Title
Characteristics of charge carriers in nanostructures

Permalink
https://escholarship.org/uc/item/4wj087pj

Author
Meyertholen, Andrew

Publication Date
2009

UNIVERSITY OF CALIFORNIA, SAN DIEGO

Characteristics of Charge Carriers in Nanostructures

A dissertation submitted in partial satisfaction of the
requirements for the degree
Doctor of Philosophy

in

Physics

by

Andrew Meyertholen

Committee in charge:

Professor Michael Fogler, Chair
Professor Daniel Arovas
Professor Leonid Butov
Professor Michael Holst
Professor Andrew Kummel

2009

The dissertation of Andrew Meyertholen is approved, and it is acceptable in quality and form for publication on microfilm and electronically:

Chair

University of California, San Diego

2009

DEDICATION

To my wife, Emily.

EPIGRAPH

Ninety percent of life is just showing up.

—Woody Allen

TABLE OF CONTENTS

LIST OF FIGURES

LIST OF TABLES

ACKNOWLEDGEMENTS

I would like to begin by thanking my advisor, Professor Michael Fogler. I truly appreciate his expert guidance and insights through every step of my research career. I will use skills I developed under his tutelage in the years to come. I would also like to thank all the current and former members of the Fogler research group for their help and camaraderie.

I am very grateful to all my collaborators for their critical contributions to my work and this dissertation. Working with them has been a great pleasure. In particular, I would like to thank Professor Leonid Butov and his research group. My research has developed, in part, thanks to many illuminating conversations I've had with Professor Butov and his team. I would also like to thank Professor Dimitri Basov and his student Zhiqiang Li for their contributions to the work in Chapter 5.

I've had the opportunity to work with many UCSD professors as a teaching assistant. These experiences were an essential component in the formation of my teaching philosophy and offered great opportunities to teach upper-level physics courses. I've picked up many tips and tricks of the trade through my relationships with these professors. I am indebted to them for their unselfish advice and contributions to my growth as both a teacher and a potential research professor. In particular, I would like to thank Professor Daniel Arovas, Professor Max DiVentra and Professor James Branson.

I consider myself lucky to have gained many friendships at UCSD, most notably with my incoming class of 2004. Thanks for being there through the good and bad times. It would not have been the same without you. I would specifically like to thank the “couples”: Evan and Hollie Bierman, Aleks Simic and Blazenka Palescak, Sean and Eva Simon, and Matthew and Elizabeth Sudano.

My family has been very supportive through this whole process. Special thanks to my parents Joe and Kathy and to my sister and brother, Amy and Dan. My in-laws could have never planned for their little girl's husband to go back to school at age 31. I'd like to thank them for their love and support - thanks Uncle Bob and Carol Bally. Also thanks to my new brothers and sister Ian, Laura, and Ben

Bally, and my soon-to-be sister Joy Peralta.

Chapter 3 contains materials from the paper: A. D. Meyertholen and M. M. Fogler, “Biexcitons in two-dimensional systems with spatially separated electrons and holes” in *Phys. Rev. B.* volume **78** page 235307 published in 2008. The dissertation author was the primary investigator and author of this paper.

I would also like to acknowledge NSF grant DMR- 0706654 for supporting this work.

Finally thanks to my wife Emily for putting up with all that the graduate student life entails. I’m so glad you are my life partner.

VITA

1997	B. S. in Physics, University of Illinois, Urbana-Champaign
1999	M. S. in Physics, University of Illinois, Urbana-Champaign
2000-2004	Physics Faculty, Bay de Noc Community College
2009	Ph.D. in Physics, University of California, San Diego
Fall 2009	Assistant Professor, University of Redlands
1997-1999	Named in "Teachers Rated as Excellent by their Students" list, University of Illinois
2004 and 2006	Two-time recipient of UC San Diego Physics Department Teaching Assistant Excellence Award
2005	Received UC San Diego Physics Departmental GAANN Fellowship
2009	Awarded UC San Diego Graduate Teaching Fellowship for summer 2009

PUBLICATIONS

A. D. Meyertholen, Z. Q. Li, D. N. Basov, M. M. Fogler, M. C. Martin, G. M. Wang, A. S. Dhoot, D. Moses, and A. J. Heeger, "Concentration-dependent mobility in organic field-effect transistors probed by infrared spectromicroscopy of the charge density profile", *Appl. Phys. Lett.*, **90**, 222108, 2007.

A. D. Meyertholen and M. M. Fogler, "Biexcitons in two-dimensional systems with spatially separated electrons and holes", *Phys. Rev. B.*, **78**, 235307, 2008

M. Remeika, J.C. Graves, A.T. Hammack, A.D. Meyertholen, M.M. Fogler, L.V. Butov, M. Hanson and A.C. Gossard, "Localization-delocalization transition of indirect excitons in lateral electrostatic", *Phys. Rev. Lett.*, **102**, 186803, 2009.

ABSTRACT OF THE DISSERTATION

Characteristics of Charge Carriers in Nanostructures

by

Andrew Meyertholen
Doctor of Philosophy in Physics

University of California San Diego, 2009

Professor Michael Fogler, Chair

This dissertation investigates charge carriers in nanoscale devices through theoretical and numerical means. First we study indirect excitons in coupled quantum wells (CQW), which exhibit evidence of a quantum mechanical state of matter. We examine whether these excitons form bound state biexcitons in CQW. It is proven that stable biexcitons exist only when the distance between electron and hole layers is smaller than a certain critical threshold. Numerical results for the biexciton binding energies are obtained using the stochastic variational method and compared with the analytical asymptotics. The threshold interlayer separation and its uncertainty are estimated. Furthermore, models are proposed to explain recent exciton experiments involving electrostatic traps. These models prove qualitatively correct and allow for estimation of the diffusion coefficient and interaction strength in CQW systems. In addition, we study organic field-effect transistors (FETs). Recent infrared imaging studies of the charge density profile in poly(3-hexylthiophene) (P3HT) FETs show evidence of a density-dependent mobility. A model is presented that concludes the mobility of P3HT has a power-law density dependence, which is consistent with the activated transport in disorder-induced tails of the density of states.

Chapter 1

Introduction

1.1 Nanoscience

Toward the end of 1959, Professor Richard Feynman presented a lecture at the American Physical Society meeting entitled “There’s plenty of room at the bottom.” He outlined what he believed to be an exciting unexplored field in science — what we now call nanoscience. Feynman envisioned one day being able to fashion materials one atom at a time, and proposed that the nanoscale world held great potential for important advances. Feynman’s belief has since been vindicated. Nanoscience has exploded into a thriving interdisciplinary pursuit.

Today nanoscience is defined as the study of materials with at least one dimension being of the atomic scale, typically 100 nm or less [1]. At this scale, quantum mechanical effects become important. These materials may be treated as quasi-lower-dimensional systems. As a sheet of paper may appear to be a two-dimensional plane in many respects, a material with one nano-sized dimension may be treated as a two-dimensional system. When studying novel lower-dimensional systems new physics often arises, as these systems behave very differently than their three-dimensional counterparts. This new physics is exciting in its own right, but it can also lead to technological innovations. The study and implementation of these new applications comprises the field of nanotechnology.

Nanoscience has proven to be a robust field and shows little signs of slowing down. For instance, advances in giant magneto-resistance have led to the development of devices such as iPods and flash drives. The coupling of nanoparticles and cancer-seeking enzymes offers the potential for a novel cancer treatment whereby nanoparticles attach to cancer cells to allow for targeted irradiation. Extensive studies of nanosized tubes called carbon nanotubes show promise for improving hydrogen storage capabilities in automobile fuel cells, and for decreasing transistor size. Recently two-dimensional sheets of carbon, called graphene, have been realized in the lab. These sheets have many exciting characteristics, including very large electron mobility that could revolutionize electronics. One thing is clear: nanoscience is one of the driving forces in the development of new technologies in fields such as biotechnology, alternative energy and electronics.

1.2 This work

This dissertation focuses on the study of charge carriers in nanosized devices, of which a better understanding is critical to further nanoscience developments. There are two main courses of study in this work; (1) the study of indirect excitons in quasi-two-dimensional coupled quantum wells, and (2) the study of electrons in quasi-two-dimensional organic field-effect transistors. Both of these systems exhibit new physics which could lead to physical and technological advances.

The exciton is a bound state of an electron and a hole, and is the primary excitation in solids. Excitons are essential to many applications, from basic electronics to solar cell technology. At low temperatures, indirect excitons in coupled quantum wells are theoretically predicted to form a number of novel states of matter ranging from Bose-Einstein condensates to superfluids and ordered crystals. These are briefly discussed in Section 2.3. The experimental search for such states has been reviewed in Reference [2].

A brief introduction to the quantum well nanostruture is in order. A quantum well is a slab of material with one of its three dimensions reduced down to a few nanometers or, more typically, a few tens of nanometers. The surrounding material makes the quantum well act as a potential well, essentially confining the charge carriers to two dimensions [3]. Coupled quantum wells will be explained in greater depth in Section 2.2.

The research addressed here on indirect excitons focuses on the formation of biexcitons, a bound state of two excitons. A state-of-the-art numerical program, the stochastic variational method, explained in depth in Section 2.4, was used to calculate the most accurate values to date of the biexciton binding energy. With these calculations, it is possible to predict under which experimental conditions these indirect biexcitons will form. This proves helpful in explaining recent experimental results theoretically. Furthermore, this is also a good first step in understanding the interaction of two indirect excitons, the comprehension of which is crucial to interpreting experimental results and finding novel uses for these systems.

Further work explores recent excitonic experiments involving electrostatic traps. These traps allow for a broader, more comprehensive study of the excitons. Photoexcited excitons fill the traps as a result of the complicated interplay of relaxation, exciton transport, and recombination. Our goal was to calculate the density distribution of excitons theoretically and use this to analyze and interpret recent experimental findings [4]. These calculations resulted in an estimate of the strength of the aforementioned indirect exciton interaction.

The problem of charge injection and dynamics is central to the conclusion of this thesis (Chapter 5), which is devoted to organic field-effect transistors. Organic electronic devices are much cheaper than their silicon counterparts, and can be made mechanically flexible. The development of effective organic electronics is an exciting prospect with diverse applications.

Organic semiconductors have complicated transport mechanisms, which must be better understood in order to develop useful organic technologies. Through the modeling of infrared spectrometry results from the Basov group at UCSD, a successful model for the density-dependent mobility in poly(3-hexylthiophene) P3HT was found. This density dependence itself has proven to be a surprise.

This thesis is organized as follows. Chapter 2 introduces excitons and biexcitons in coupled quantum wells and reviews the low-temperature physics of excitonic gases. A brief review of the experiments by Butov *et al.* will also be included. Chapter 3 presents results of numerical calculations involving indirect biexcitons and studies the experimental conditions an indirect biexciton may be expected to form in a coupled quantum well system. Chapter 4 is a theoretical exploration of the recent experiments by the Butov group at UCSD in which indirect excitons are placed in various electrostatic traps, giving the experimenter more ways in which to probe them. Finally, Chapter 5 consists of a study of the mobility in organic field-effect transistors probed by infrared spectromicroscopy of the charge density profile. This is based on experiments performed by the Basov group at UCSD.

Chapter 2

Excitons in coupled quantum wells

2.1 Excitons

Recent experiments performed by the Butov group at UCSD have produced evidence for quantum liquid behavior in an excitonic gas in Gallium Arsenide semiconducting quantum wells — a goal of experimentalists for years [2]. This chapter introduces indirect excitons and provides some background on these experiments.

The exciton is the fundamental excitation in a semiconductor solid. It is an excited state consisting of an electron and a hole bound together by the Coulomb interaction. The hole, a so-called quasi-particle, is the lack of an electron in the otherwise full electron sea or valence band. Generally, an exciton is created by the absorbtion of a photon of light exciting an electron from the electron sea into the conduction band [5]. This missing electron is called a hole. Since there is a missing negative charge in an otherwise neutral material, the hole will have a positive charge.

Excitons are generally broken down into two main types. The main distinction is the separation distance between the electron and the hole. A Frenkel exciton is generally separated by a single lattice site, and is usually associated with a certain lattice site. By contrast, a Wannier exciton has a separation of many lattice sites [6]. Our focus is on Wannier excitons.

A Wannier exciton can be thought of as a free particle under the effect of the background lattice. Interaction between the exciton and the background lattice is extremely complicated. However, a good approximation of this interaction is achieved by treating the exciton as a free bound particle propagating with a renormalized mass in a medium with a dielectric constant of the lattice material [6]. To this end, the exciton can be thought of as a hydrogen-like atom, whereby the hole is analogous to the proton. The energy of such a hydrogen-like atom is

$$E_{ex} = -\frac{e^2}{2a_{ex}\epsilon_0 d^2}\,, \tag{2.1}$$

where a_{ex} is the excitonic Bohr radius

$$a_{ex} = \frac{\hbar^2\epsilon_0}{e^2 m_r}\,, \tag{2.2}$$

and where m_r is the reduced mass

$$a_{ex} = \frac{m_h m_e}{m_h + m_e}. \tag{2.3}$$

Here m_h is the mass of the hole and m_e is the mass of the electron [6].

Since it is a particle-antiparticle pair, the exciton has a finite lifetime, typically between picoseconds and milliseconds. As we will see, this fact limits the nature and variety of experimental tests one can achieve with excitons. Much effort has gone into devising methods to extend the excitonic lifetime. One method is to excite excitons into neighboring quantum wells in a system called a coupled quantum well, which will be discussed in Section 2.2.

Excitons merit study as the primary excitation in solids, but they are interesting for many other reasons as well. Excitons can couple with photons one-to-one, essentially converting a photon into a particle with a much shorter wavelength, and having the ability to convert back at some future time. This could prove useful in applications such as excitonic optical transistors, the first step toward the development of optical computers [7]. Because it is a bound state of two fermions, the exciton is a boson and is theorized to become a Bose-Einstein condensate (BEC) in the dilute limit $na_{ex}^D << 1$, where n is the particle density, a_{ex} the excitonic Bohr radius, and D the dimensionality of the system [8]. Achieving this BEC state has been a major experimental goal. The temperature at which a BEC should occur decreases with the mass of the constituent particles, see Eq. (2.20). Since the mass of the exciton is much smaller than the electron, the temperature at which BEC should occur is relatively high, on the order of a few degrees Kelvin. Further discussion on this topic will follow in Section 2.3. Next is a discussion of quantum wells, the systems in which the indirect excitons are studied.

2.2 Coupled quantum wells

The most basic model of charge carriers in a solid is the free-electron approximation, the so-called Fermi gas model. In this model each electron in a solid is treated as free with no interaction potential, either from the lattice ions or the other electrons. This gas of non-interacting electrons is called a Fermi gas, see Appendix D, and is the condensed matter equivalent of an ideal gas. The free-electron approximation is limited, but can prove useful in explaining aspects of electron behavior in solids, especially in a qualitative sense. Furthermore, it serves as a starting-off point for more advanced theories that involve interactions including perturbation theory and the Fermi-liquid theory [9].

With no potential energy term V, the Schrodinger equation for these electrons becomes

$$\frac{-\hbar^2}{2m}\nabla^2\Psi(\mathbf{r}) = E\Psi(\mathbf{r}). \tag{2.4}$$

The boundary conditions on the electrons are periodic with the lattice. If the lattice is assumed to be isotropic, Born-von Karmon periodic boundary conditions apply where $\mathbf{L}$ is the lattice vector. The solution to Eq. (2.4) is

$$\Psi(\mathbf{r}) = \frac{1}{\sqrt{V}}\, e^{i\mathbf{k}\cdot\mathbf{r}}, \tag{2.5}$$

and the energy for one of these electronic states is

$$E = \frac{\hbar^2\mathbf{k}^2}{2m^2}. \tag{2.6}$$

Important to determining various properties of the system is how the macroscopic number of electrons fill these momentum states. Being fermions, the elec-

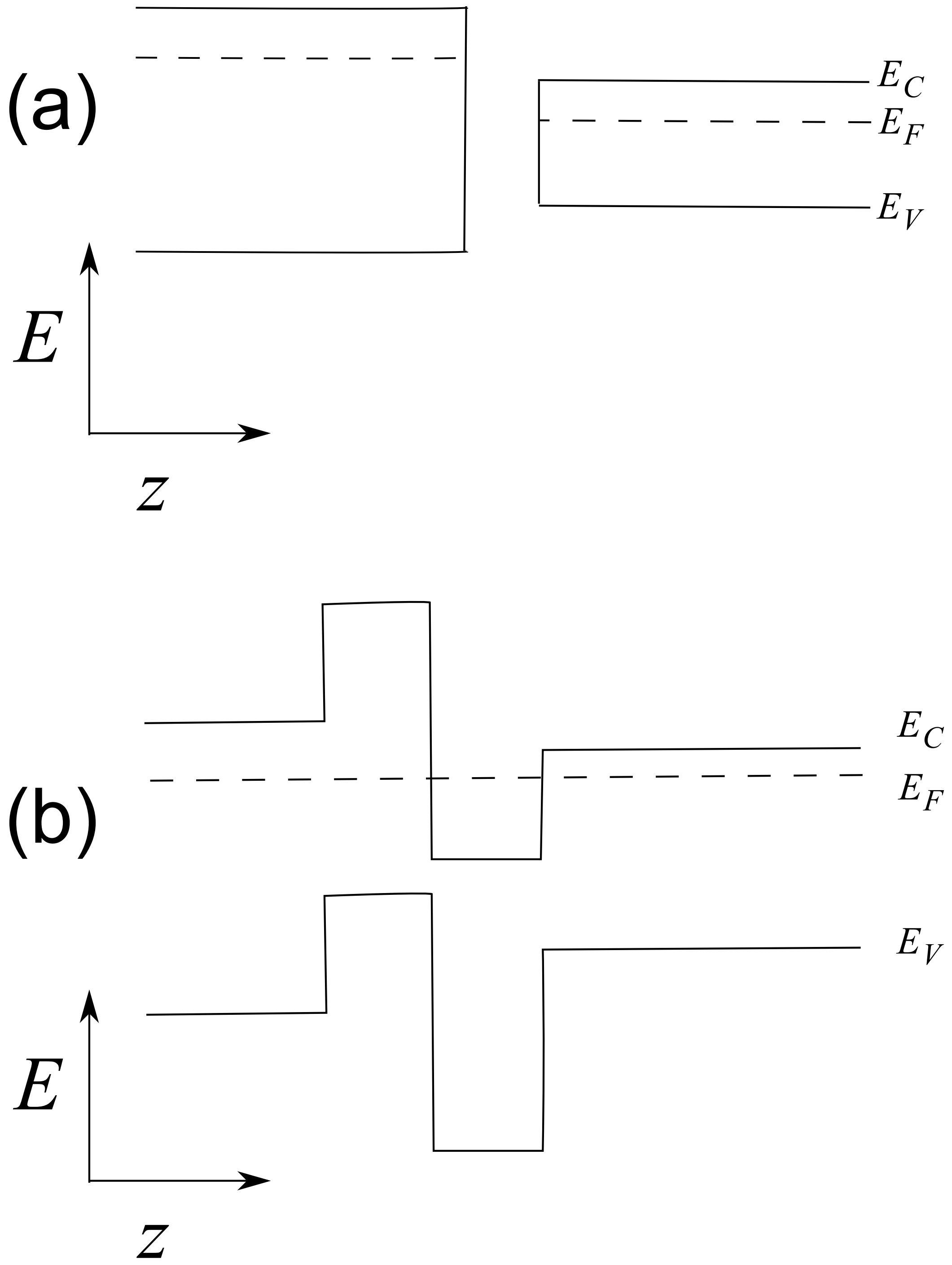

Figure 2.1: Energy band diagram for quantum well heterojunction. (a) Two semiconducting materials with different band gaps are brought together. E_C is the conduction band, E_V is the valence band, and E_F is Fermi energy. (b) When combined, an equilibrium band state is reached with a potential well in the z-direction.

trons fill these levels according to Fermi-Dirac statistics, with two spins for each state. A quantity known as the density of states can be found to better quantify this process. The density of states provides the number of momentum states that exist in a certain energy range. This quantity proves useful in calculating macroscopic characteristics for the solids in question. To do this, we work in the momentum space, or k-space: the space that spans the system's possible momentum [9]. The density of states in three dimensions is

$$\mathcal{D}(E) = \frac{V}{2\pi^2}\left(\frac{2m}{\hbar^2}\right)^{3/2} E^{1/2}. \tag{2.7}$$

The quantity k_F is defined as the Fermi momentum. It is the maximum occupied momentum state of a Fermi gas.

A quantum well structure consists of a semiconducting material, like gallium arsenide (GaAs), joined with a doped semiconducting material with a larger band gap such as aluminum gallium arsenide (AlGaAs). The interface between these two materials is known as a heterojunction [3]. As in Fig. 2.1 (a) the materials have different Fermi energies and band gaps. Electrons are attracted from the higher Fermi energy to the lower. When the two materials come together, an equilibrium is reached, as in Fig. 2.1 (b). This results in the formation of a potential well in one of the spatial directions, which we will call the z-direction. Electrons in this potential well feel a potential similar to

$$U(z) = \begin{cases} \infty & : |z| > a \\ 0 & : |z| < a. \end{cases} \tag{2.8}$$

Here, the electrons are free in two dimensions and confined in one dimension, leading to a wave function

$$\Psi(\mathbf{r}) = \frac{1}{\sqrt{V}}\,\phi(z)\exp{(ik_x)}\ \exp{(ik_y)}, \tag{2.9}$$

where $\phi(z)$ is the solution to a one-dimensional potential well. Since this is a potential well, the energy is quantized. Essentially these electrons are confined in the z-direction and are free, a Fermi gas, in the x-y plane. Altogether the energy of an individual electron is

$$E = E_S + \frac{\hbar^2}{2m}(k_x^2 + k_y^2). \tag{2.10}$$

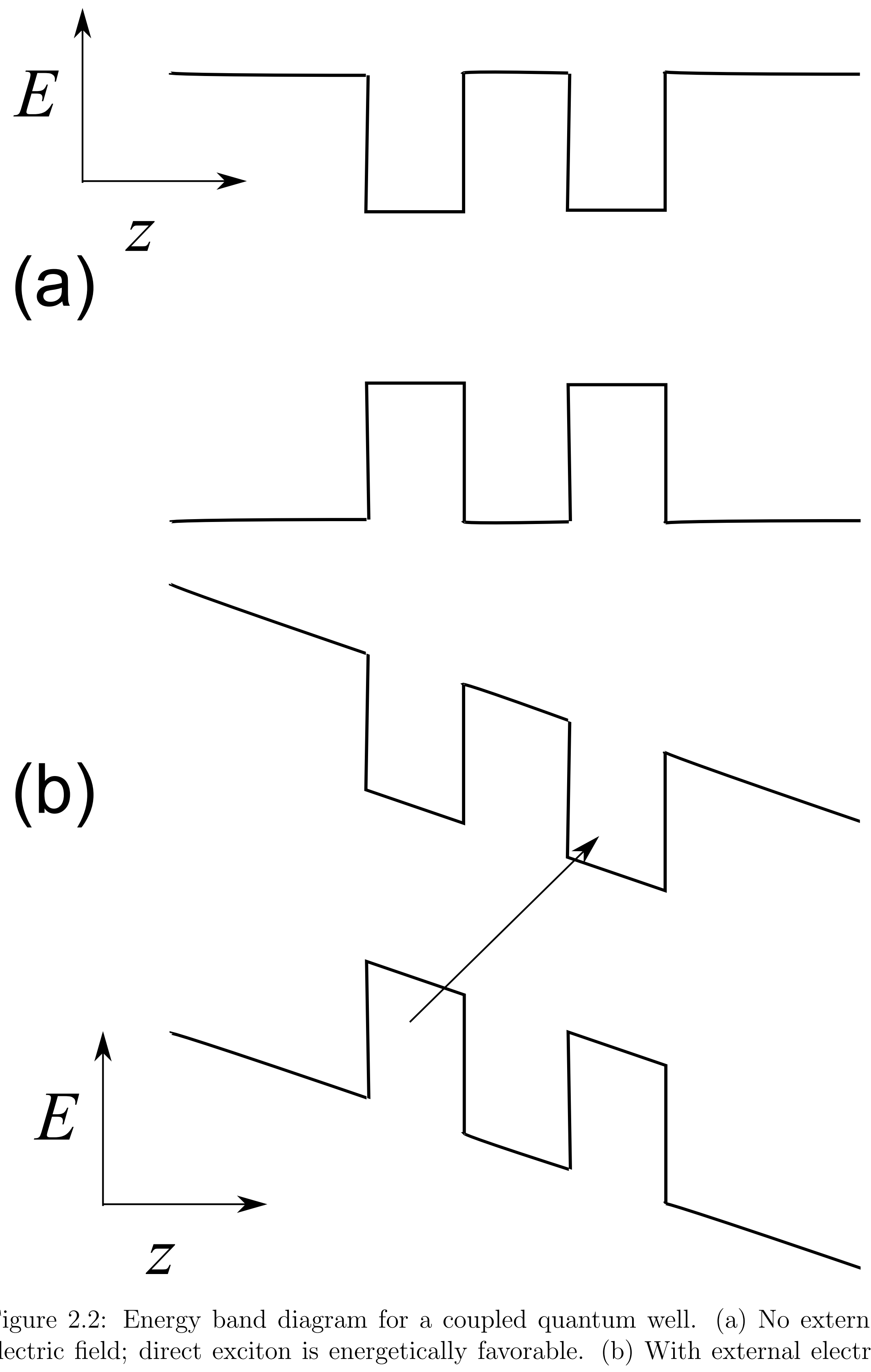

Figure 2.2: Energy band diagram for a coupled quantum well. (a) No external electric field; direct exciton is energetically favorable. (b) With external electric field, indirect exciton is favorable. Electron and hole can be in neighboring wells.

Here E_S is the energy of the electron in this potential well. The system now consists of a quasi-two-dimensional gas of electrons. We must now determine how this differs from a three-dimensional gas of electrons. We find that it is considerably different, and to investigate one must look at the density of states in two dimensions:

$$\mathcal{D}(E) = \frac{L^2 m}{\pi \hbar^2}. \tag{2.11}$$

To fully express the density of states for a quantum well, one must remember that there are different subband states for each two-dimensional Fermi gas energy spectrum. The number of occupied subbands will alter the density of states. Including the different subbands, the density of states for a quantum well is

$$\mathcal{D}(E) = \sum_{S}^{N_S} \frac{L^2 m}{\pi \hbar^2} \theta \left(E - E_S\right). \tag{2.12}$$

The density of states in two dimensions is independent of energy and hence vastly different from its three-dimensional counterpart. Many macroscopic properties of the solid depend on the density of states. Therefore this gas will have very different characteristics when compared to a three-dimensional gas.

The quantum well then acts as a one-dimensional potential well confining electrons in one dimension, resulting in a quasi-two-dimensional gas of electrons. A coupled quantum well is essentially two neighboring quantum wells separated by the doped semiconduction material [2]. This will allow for the creation of an indirect exciton, an exciton in which the hole and electron are in two neighboring wells. These indirect excitons will be discussed in the next section, as well as the experiments done by the Butov group. The work in Chapter 3 derived its motivation from these experiments.

2.3 Basic properties of cold excitonic gases in semiconductor quantum wells

As mentioned in Section 2.1, excitons at low densities are Bose particles obeying Bose-Einstein statistics. At low temperatures they are theorized to become a quantum liquid, a statistically degenerate Bose gas or Bose-Einstein condensate. Producing a quantum state of excitons in the lab has proven difficult. A discussion will follow with a summarization of this theory and a description of recent experiments by the Butov group at UCSD by which the results in Chapter 3 were prompted.

A gas of Bosons will, in general, obey the Bose-Einstein distribution function

$$N = \frac{1}{e^{\beta(k^2/2m-\mu)} - 1}, \tag{2.13}$$

where k is the momentum vector, μ is the chemical potential, and

$$\beta = \frac{1}{k_B T}. \tag{2.14}$$

Here, k_B is the Boltzmann constant, and T is the temperature. In turn, the density of this gas is found via

$$n = \frac{\mathcal{G}}{(2\pi)^D} \int_{-\infty}^{\infty} N(k) d^D k = \frac{\mathcal{G}}{(2\pi)^D} \int_{-\infty}^{\infty} \frac{d^D k}{e^{\beta(k^2/2m-\mu)} - 1}, \tag{2.15}$$

where $\mathcal{G}$ is the spin degeneracy of excitons, and D is the dimensionality of the system.

In the low density limit $na_{ex}^D << 1$, the chemical potential μ must have an upper bound of zero. Therefore for a three-dimensional gas, Eq. (2.15) becomes

$$n = 2.612\mathcal{G} \left(\frac{m_{ex} k_B T}{2\pi} \right)^{(3/2)}. \tag{2.16}$$

Since this is constant, a problem arises. How does the system accommodate the addition of more particles? In other words, how can this density be constant for any system with any number of particles? The answer Einstein gave is that the density in Eq. (2.16) does not account for the ground state, so any particle in addition to this must "condense" into the ground state, leading to a deviation from the Bose-Einstein distribution function. This will occur around temperatures approaching

$$T_C = \left(\frac{n}{2.612\mathcal{G}} \right)^{(2/3)} \frac{2\pi}{m_{ex} k_B}. \tag{2.17}$$

This condensate is known as a Bose-Einstein condensate and is an inherently quantum mechanical manifestation.

Bose-Einstein condensation in various systems may lead to a state called the superfluid. A superfluid is a quantum mechanical state of matter with very peculiar macroscopic properties, including zero viscosity and persistent current states or quantized vortices. The microscopic mechanism behind the superfluid phase can be varied. He_4, a bosonic atom, becomes a superfluid associated with the onset of Bose-Einstein condensation; while He_3, a fermionic atom, will become a superfluid as a consequence of the BCS theory of superconductivity.

For infinite two-dimensional systems, a Bose-Einstein condensate does not occur. This is a consequence of the constant density of states for the two-dimensional system (see Section 2.2). Since the density of states is constant, the lower energy states of the system can accommodate any number of particles. There is no need for a condensate in this case.

However, the statistics of a quasi two-dimensional boson gas strongly depart from classical when the de Broglie wavelength

$$\lambda_{dB} = \sqrt{\frac{2\pi\hbar^2}{mk_BT}} \tag{2.18}$$

approaches the interparticle separation distance for the gas, or

$$n\lambda_{dB}^2 \approx 1. \tag{2.19}$$

For three dimensions, this is a similar requirement as in Eq. (2.17):

$$n\lambda_{dB}^3 = 2.612\,.$$

A two-dimensional gas of weakly interacting particles develops a local coherence (quasi-condensate) at a temperature

$$T_{dB} = \frac{2\pi\hbar^2 n}{m\mathcal{G}}. \tag{2.20}$$

This quasi-condensate has a large coherence length — much larger than the distance between the particles. If excitons are confined to a region smaller than this coherence length (e.g., by means of an artificial trap), the system will resemble a Bose-Einstein condensate. However, in the thermodynamic limit it will not be a true condensate and will not exhibit superfluidity.

As temperature is reduced further, the a two-dimensional system will undergo a superfluid transition. This transition is of the Kosterlitz-Thouless type [11]. It is theorized to happen at a temperature of [12]

$$T_{KT} = \frac{4\pi\hbar^2 n}{2m \ln\ln(1/na^2)}. \tag{2.21}$$

Below T_{dB} and above T_{KT} the quantum liquid will be a microscopic superfluid with free (unpaired) vortices. Below T_{KT} the liquid will be a macroscopic superfluid with vortices bound in vortex-antivortex pairs.

Recent estimates of the T_{KT} from Monte-Carlo calculations [13] agree with Eq. (2.21); however, they suggest that the argument of the inner logarithm contains an additional numerical factor of approximately 380.

The creation of an excitonic quantum liquid is difficult for many reasons. The finite lifetime of excitons makes it difficult to cool them to a temperature at which quantum effects become important. This lifetime has been extended through the creation of so-called indirect excitons created in a coupled quantum well structure [2]. As previously discussed, a quantum well is a quasi-two-dimensional structure with one dimension on the order of 100 nm. A coupled quantum well is a structure with two parallel quantum wells separated by a small potential barrier. This allows for the creation of an indirect exciton, an exciton whose hole and electron are in separate quantum well planes separated by a distance d, as in Fig. 2.3. Because of the small wave function overlap from neighboring quantum wells, the recombination of the exciton is suppressed and the lifetime is extended by three orders of magnitude or more [2]. In a symmetric coupled well (no electric field applied) the lowest energy exciton is the direct exciton: both e and h reside in the same well. This changes in the presence of a field. The electron moves because it becomes energetically favorable, see Fig. 2.2.

Due to the spatial separation between e and h, an indirect exciton possesses an electric dipole. This results in a dipolar repulsion between indirect excitons. This works to minimize the creation of electron-hole droplets [14, 15] and speed the drift of excitons away from the excitation zone, allowing them to cool to the lattice temperature and approach the range of temperatures required for forming an excitonic quantum liquid.

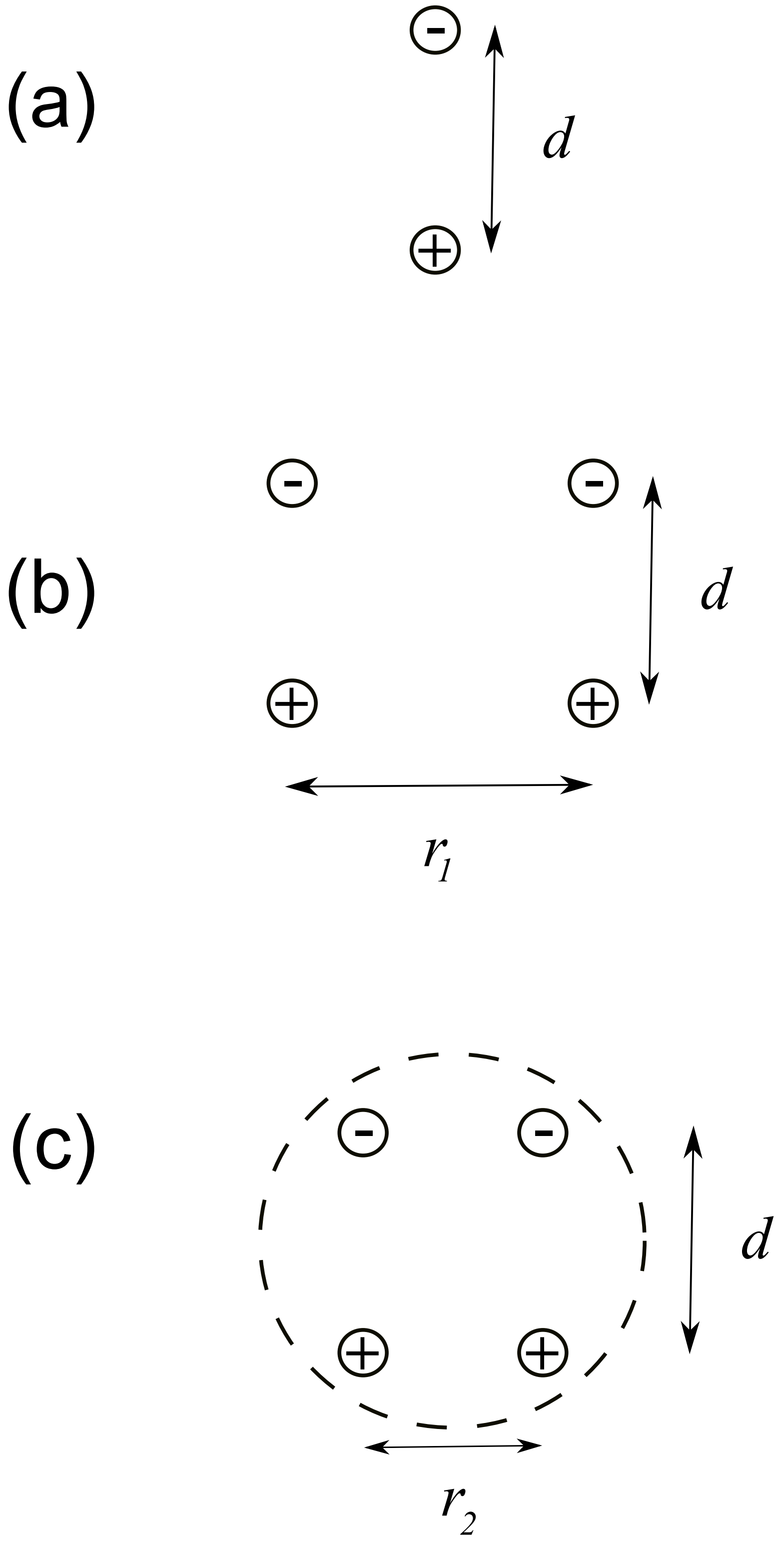

Figure 2.3: Indirect excitons and biexcitons. (a) Indirect exciton. (b) At large separation distances, indirect excitons are dipoles and thus repel each other. (c) At some distance r_2, indirect excitons bind together forming a biexciton. This is studied in Chapter 3.

This repulsion also allows for estimation of the excitonic density. Due to this dipolar repulsion, the energy of each exciton is density-dependent. One may calculate an energy shift of

$$\delta\omega(n) = \frac{4\pi n e^2 d}{\epsilon}. \tag{2.22}$$

Eq. (2.22) is a crude approximation (this "capacitor" formula is derived in Section 4.3.2). This energy shift does not take exchange or correlation effects into account. In fact, it's possible the excitons can feel attraction as opposed to repulsion, similar to a bound H_2 molecule. This scenario is investigated in Chapter 3. In Chapter 4 estimates of this interaction show that for UCSD experiments [4] there is indeed repulsion, however at a value 2-3 times less than Eq. (2.22) would indicate.

The experiments that motivated this work were performed by the Butov group at UCSD. The group carried out photoluminescence studies of exciton gases in coupled quantum wells. These structures are made from GaAs and have an 8 nm well and a 4 nm barrier of $\mathrm{Al}_{0.33}\mathrm{Ga}_{0.67}\mathrm{As}$ [2]. The excitons are excited by a HeNe laser (λ= 632.8 nm) or a Ti:Sapphire laser (λ = 786 nm). The excitation region has a 10 μm diameter region in a square lattice of size 150 μm by 150 μm [2]. The lattice in turn may be cooled to a fraction of one degree Kelvin. The excitons are photoexcited into existence, and when they eventually recombine a photon is released. These photons are captured with a CCD camera. The de Broglie temperature, Eq. (2.20), is approximately $T_{dB} \approx 3$ K for this experiment [2].

The experimental results are highly dependent on the excitation power of the laser. At low excitation power, the excitonic gas essentially takes on the shape of the excitation region. It is believed the excitons are localized by in-plane disorder. However at larger excitation power, as the density of excitons is increased, the dipolar repulsion washes out the disorder and the excitons become delocalized. When this occurs, interesting patterns emerge. An example of these patterns can be seen in a photoluminescence intensity image in Fig. 2.4. The main features include the internal and external ring, localized bright spots, and a macroscopically ordered exciton state [2]. The internal ring and localized bright spots have been explained through classical mechanisms. Since the excitons have a drift velocity

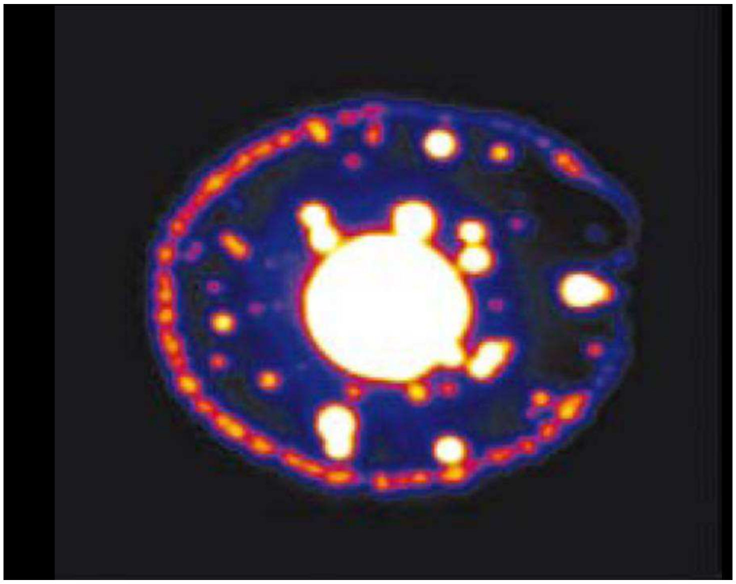

Figure 2.4: Example of two-dimensional photoluminescence pattern for experiment by Butov group. Temperature is 1.7 K, gate voltage is $V_g = 12\ V$, and excitation power is $P_{ex} = 690\ \mu$W [16].

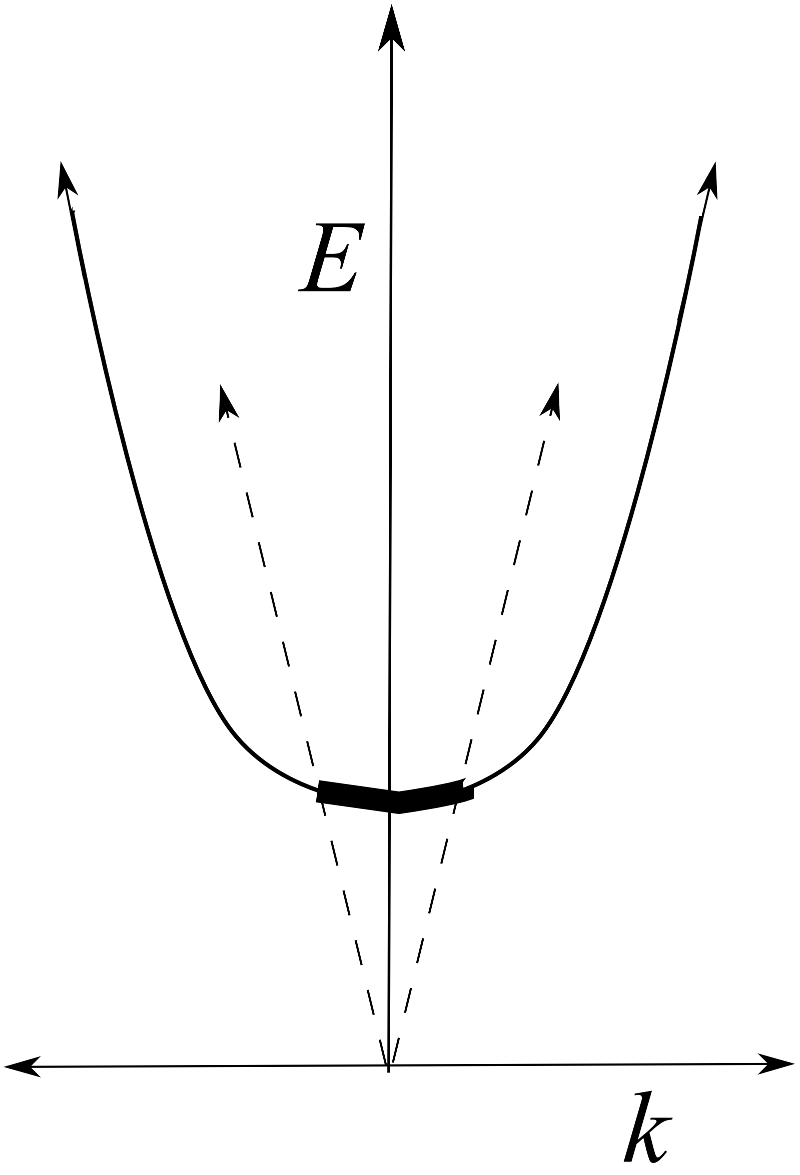

Figure 2.5: Dispersion relationship for photons (linear dashed curve) and excitons (quadratic solid curve). Due to conservation of energy and momentum, only excitons in the dark highlighted region are optically active.

due to diffusion and the dipolar repulsion, they are not typically optically active until they have traveled from the excitation spot. As seen in Fig. 2.5, only excitons in the radiative zone will be optically active. Thus, the delocalization of the excitons works to extend their lifetime even further. As the excitons transport over distances of as much as 100 μm, they lose energy and eventually come to an energy in the radiative zone. If excitons at the internal ring are still not optically active, they will pick up a larger kinetic energy as they traverse out of the potential hill caused by the excitation zone. This accounts for the inactive region before the start of the external ring. The localized bright spots are in this inactive region, and are believed to be associated with the local disorder of the system [2].

The radius of the external ring increases with excitation power. At extremely low temperatures the ring creates a beaded pattern, an example of macroscopic spatial ordering. This can again be seen in Fig. 2.4. These beads can appear in circular lengths up to 1 mm. The temperature at which this pattern emerges is close to the critical temperature at which quantum liquid effects should set in, $T_{dB} <$ 3K. It is believed this pattern is a quantum mechanical effect, and is a sign the excitons have become a quantum liquid or are in a quasi-Bose-Einstein condensate state [17]. This is further borne out by data that shows that the coherence length of the excitons exceeds the classical limit at this transition [18]. Further progress in this field requires a better understanding of exciton-exciton interaction. This motivated us to study the simplest interacting system — a pair of indirect excitons, see Fig. 2.3. The results of this investigation will be discussed in detail in Chapter 3. However, by way of extended introduction, the computational method used in Chapter 3 is reviewed.

2.4 Stochastic variational method

In Chapter 3, the stochastic variational method (SVM) is employed. This computational technique solves the few-body Schrodinger equation

$$H = -\sum_{i=1}^{N} \frac{\hbar^2 \nabla_i^2}{2m_i} + \sum_{i \neq j} \frac{e_i e_j}{r_{ij}} \tag{2.23}$$

using the variational principle [19]. The basis states used for the trial wave function are correlated Gaussians

$$\psi(\mathbf{x}, \mathbf{B}_n) = \mathcal{A}\left[G_n(\{\mathbf{r}_\nu\})\right] \, , \tag{2.24}$$

with the form

$$G_n = \exp\left(-\frac{1}{2}\mathbf{x}^\dagger \mathbf{B}_n \mathbf{x}\right) \, , \tag{2.25}$$

where $\mathbf{x}$ are the Jacobi coordinates, a generalized center of mass coordinate system, given by

$$\mathbf{x}_i = \sum_{j=1}^{N} \mathbf{U}_{ij}\mathbf{r}_j, \tag{2.26}$$

where $\mathbf{r}$ are the spatial coordinates and

$$U = \begin{pmatrix} -1 & 1 & 0 & 0 \\ -\frac{m_1}{m_{12}} & -\frac{m_2}{m_{12}} & 1 & 0 \\ -\frac{m_1}{m_{13}} & -\frac{m_2}{m_{13}} & -\frac{m_3}{m_{13}} & 1 \\ \frac{m_1}{m_{14}} & \frac{m_2}{m_{14}} & \frac{m_3}{m_{14}} & \frac{m_4}{m_{14}} \end{pmatrix} \tag{2.27}$$

is the transformation matrix for a four-particle system. Here $m_{1i} = m_1 + m_2 ... + m_i$. The Gaussian basis functions are advantageous due to their ease of integration.

The program uses a random process to determine the exact values of $\mathbf{B}_n$, which determine the form of the Gaussian function itself. The algorithm for the program is as such: (1) an initial randomly generated guess is made for the coefficients $\mathbf{B}_1$, (2) the ground state energy of the system is found by diagonalizing the Hamiltonian, (3) each $\mathbf{B}_1$ is varied and a new energy found, (4) if this new coefficient lowers the energy it is kept, then the program goes back to step three and repeats a specified number of times. Next, (5) after varying each $\mathbf{B}_1$ a set number of times, these coefficients are the best $\mathbf{B}_1$ coefficients. Now a new basis state represented by the $\mathbf{B}_2$ coefficients is created and steps two through four are repeated a specified number of times. The result is a numerically exact value for the ground state energy. If needed, the program may be easily modified to find density functions etc., see Fig. 3.6.

This state-of-the-art program works much faster than alternatives such as diffusion Monte Carlo. Typically for four-body problems done in Chapter 3, the basis size was on the order of 400 - 700, with a run time of approximately ten minutes to a couple of hours on a laptop computer. The program was designed by Varga and Suzuki and has been used with much success [19]. The limiting feature here is diagonalization of the Hamiltonian. To speed things up, a Gram-Schmidt process is employed so a full diagonalization for each step is not necessary. Still, a basis size of over 700 for a system of four or more particles becomes time-intensive.

In its present form, the code works only for states with zero orbital angular momentum. Furthermore, the program has difficulty finding the ground state for loosely bound states and excited continuum states. Special techniques can be employed to handle these cases [20]. For the work in Chapter 3 the program has been altered to work for two dimensions and for the various potentials used.

In Chapter 3 we solved the four-body biexciton equation

$$H = -\frac{\hbar^2}{2m_e}\left[\nabla^2_{e_1} + \nabla^2_{e_2}\right] - \frac{\hbar^2}{2m_h}\left[\nabla^2_{h_1} + \nabla^2_{h_2}\right] + \sum_{i \neq j} \frac{e_i e_j}{r_{ij}}. \tag{2.28}$$

The basis states make up the trial wave function

$$\Psi = \sum_{i=1}^{K} c_i \psi(\mathbf{x}, \mathbf{B}_n)\,, \tag{2.29}$$

where K is the basis size. Then, an upper bound for the ground state energy is found by solving the generalized eigenvalue problem

$$HC = E_k OC. \tag{2.30}$$

Here H and O are the Hamiltonian and overlap matrix elements.

What follows is a summarization of the matrix element calculations in two dimensions. For a more detailed discussion please see Appendix C.

The overlap matrix element is

$$\langle G_1 | G_2 \rangle = \left[\frac{(2\pi)^{N-1}}{\det(\mathbf{B}_1 + \mathbf{B}_2)}\right]\,, \tag{2.31}$$

where N is the number of particles. The Hamiltonian matrix element is broken into two parts, the kinetic and the potential term. The kinetic matrix element works out to be

$$\left\langle G_1 | \Lambda \nabla^2 | G_2 \right\rangle = \langle G_1 | G_2 \rangle \left[2Tr\left(\Lambda \mathbf{B}_1\right) - 2\mathrm{Tr}(\mathbf{B}_2 + \mathbf{B}_1)^{-1}(\mathbf{B}_2 \Lambda \mathbf{B}_2)\right]. \tag{2.32}$$

Calculation of the potential term is the most difficult. To ease in this the potential is set in the form

$$V\left(\mathbf{r}_i - \mathbf{r}_j\right) = \int d\mathbf{r} V(\mathbf{r})\, \delta(\mathbf{r}_i - \mathbf{r}_j - \mathbf{r}). \tag{2.33}$$

Therefore, the potential matrix element will be

$$\langle G_1 | V_{ij} | G_2 \rangle = \int d\mathbf{r} V(\mathbf{r}) \left\langle G_1 | \delta(\mathbf{r}_i - \mathbf{r}_j - \mathbf{r}) | G_2 \right\rangle \,, \tag{2.34}$$

leading to the expression

$$\langle G_1 | V_{ij} | G_2 \rangle = \frac{\langle G_1 | G_2 \rangle}{2\pi p_{ij}} \int d\mathbf{r} V(\mathbf{r}) e^{-r^2/2p_{ij}}, \tag{2.35}$$

where

$$p_{ij} = \sum_{k=1}^{N-1} \sum_{k=1}^{N-1} C_{ijk} (\mathbf{B}_1 + \mathbf{B}_2)^{-1}_{kl} C_{ijl} \,, \tag{2.36}$$

and

$$\mathbf{C}_{ijk} = \mathbf{U}^{-1}_{ik} - \mathbf{U}^{-1}_{jk}. \tag{2.37}$$

Eq. (2.35) may be solved for two potentials, a potential between like charges in the same quantum well plane:

$$V(\mathbf{r})_{like} = \frac{1}{r}, \tag{2.38}$$

and a potential for unlike charges in neighboring quantum wells separated by a distance d:

$$V(\mathbf{r})_{unlike} = \frac{1}{\sqrt{r^2 + d^2}} \,, \tag{2.39}$$

leading to solutions

$$\langle G_1 | V_{ij} | G_2 \rangle_{like} = \langle G_1 | G_2 \rangle \sqrt{\frac{\pi}{2p_{ij}}} \,, \tag{2.40}$$

and

$$\langle G_1 | V_{ij} | G_2 \rangle_{unlike} = \langle G_1 | G_2 \rangle \sqrt{\frac{\pi}{2p_{ij}}}\, \mathrm{erfc}(d/\sqrt{2p_{ij}})\, e^{-d^2/2p_{ij}}. \tag{2.41}$$

A key element of the computation is the symmetrization process. The system employed in Chapter 3 solved a four-body fermionic problem where there are two sets of indistinguishable particles. The basis function is a function of the spatial coordinates $\mathbf{r}$ or $\psi(\mathbf{r}_1, \mathbf{r}_2, \mathbf{r}_3, \mathbf{r}_4)$. Therefore, the symmetrized basis function will have a form similar to

$$\begin{aligned}\psi(\mathbf{r}_1, \mathbf{r}_2, \mathbf{r}_3, \mathbf{r}_4) = \psi(\mathbf{r}_1, \mathbf{r}_2, \mathbf{r}_3, \mathbf{r}_4) - \psi(\mathbf{r}_3, \mathbf{r}_2, \mathbf{r}_1, \mathbf{r}_4) \\ - \psi(\mathbf{r}_1, \mathbf{r}_4, \mathbf{r}_3, \mathbf{r}_2) + \psi(\mathbf{r}_3, \mathbf{r}_4, \mathbf{r}_1, \mathbf{r}_2). \quad (2.42)\end{aligned}$$

An example of the input parameters for the SVM is given in Table 2.4. The first rows establish the particular system to be solved supplying the number of particles, charges and masses of the particles, and the spin and isospin states. Next come the variational parameters. $iran$ is an input parameter used in the initial random generator. ica is a parameter that selects the method of basis generation, which can be altered to fit the individual system. The next variable determines the type of particle. Here $ibf = 1$ for fermions and $ibf = 1$ for bosons. Next M_0 and K_0 are to specify the number of times a random number is to be generated for a particular basis element and the basis as a whole, respectively; and K is the number of basis sets to be used. Finally b_{min} and b_{max} are the upper and lower bounds for the basis elements, where the basis takes the form

$$\exp\left[-\sum_{i<j} \frac{(\mathbf{r}_i - \mathbf{r}_j)^2}{2b_{ij}}\right]. \quad (2.43)$$

For further explanation see the reference by Varga and Suzuki [20].

Table 2.1: An example input file for the SVM program.

input	variable name
4	number of particles
1, 1, 1, 1	masses of particles
-1, 1, -1, 1	charges of particles
1	number of isospins
1, 1, 2 , 1, 2	projections of the isospins
4	number of spins states
1, 1, 1, 2, 2	projections of the spins
-1, 1, 2, 2, 1	projections of the spins
-1, 2, 1, 1, 2	projections of the spins
1, 2, 2, 1, 1	projections of the spins
1, -11046, 2, 1	$\hbar^2/2m$, iran, ica, ibf
5, 25, 500	M_0, K_0, K
0.1, 100, 0.5	b_{min}, b_{max}, d

Chapter 3

Biexcitons in two-dimensional systems with spatially separated electrons and holes

3.1 The problem and main results

As reviewed in Chapter 3 the physics of cold excitons — bound states of electrons and holes in semiconductors — has attracted much attention recently. Several intriguing phenomena have been demonstrated for such "indirect" excitons, including long-range transport, [21, 22, 23, 16, 24, 7] macroscopic spatial ordering, [16] and spontaneous coherence [18]. Further progress in this field requires an improved understanding of exciton interactions.

Despite being charge neutral, indirect excitons possess a dipole moment ed, where d is the separation of the electron and hole quantum wells. As a result, interaction of two excitons at large distances r is dominated by their dipolar repulsion,

$$V(r) = \frac{e^2}{\kappa}\frac{d^2}{r^3}\,, \tag{3.1}$$

where κ is the dielectric constant of the semiconductor. At short distances exchange and correlation effects are also important. The interaction may even become attractive over a range of r. In this case two excitons can form a bound state

— a biexciton. The corresponding binding energy is defined by

$$E_B = 2E_{\mathrm{X}} - E_{\mathrm{XX}}\,, \tag{3.2}$$

where E_{X} and E_{XX} are the ground-state energies of the exciton and biexciton, respectively.

While observations of biexcitons in single quantum well structures ($d = 0$) have been described multiple times, [25, 26, 27, 28, 29, 30, 31, 32] no such reports exist for the $d > 0$ case. A recent theoretical work [33] has attributed the lack of experimental signatures of indirect biexcitons to extreme smallness of their binding energies. In this chapter we verify and improve all previously known estimates of E_B. In particular, we show that $E_B(d)$ is positive, i.e., the biexciton is stable, only for d smaller than some critical value d_c, see Fig. 3.1. Typical experimental parameters [2, 34] fall on the $d > d_c$ part of the diagram.

In our calculations we adopt the simplifying assumption that the effective masses m_e and $m_h \geq m_e$ of electrons and holes are constant and isotropic. We also treat the quantum wells as two-dimensional layers of zero thickness. We find it convenient to measure distances in units of the effective electron Bohr radius and energies in units of the effective Rydberg,

$$a_e = \frac{\hbar^2\kappa}{m_e e^2}\,, \quad \mathrm{Ry}_e = \frac{1}{2}\frac{e^2}{\kappa a_e}\,, \tag{3.3}$$

respectively. With these conventions, the four-particle system of two electrons and two holes is described by the Hamiltonian $H_{\mathrm{XX}} = T + U$, where

$$T = T_1 + T_2\,, \quad T_j = -\nabla_j^2 - \sigma\left(\frac{d}{d\mathbf{R}_j}\right)^2\,, \tag{3.4}$$

$$U = \frac{2}{|\mathbf{r}_1 - \mathbf{r}_2|} + \frac{2}{|\mathbf{R}_1 - \mathbf{R}_2|} - \sum_{ij} v(\mathbf{r}_i - \mathbf{R}_j, d)\,, \tag{3.5}$$

$$v(\mathbf{r}, d) = \frac{2}{\sqrt{|\mathbf{r}|^2 + d^2}}\,. \tag{3.6}$$

Here $\mathbf{r}_i$ and $\mathbf{R}_i$ are two-dimensional coordinates of the electrons and the holes, respectively, $\nabla_j = d/d\mathbf{r}_j$, and

$$\sigma = m_e/m_h \tag{3.7}$$

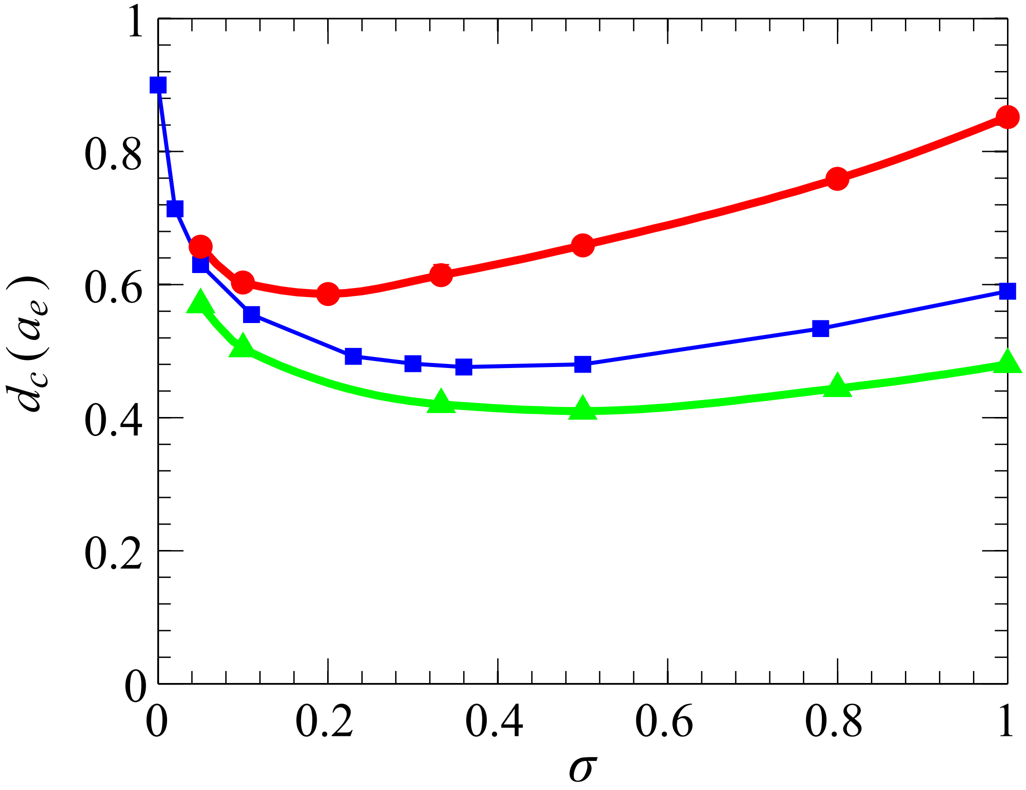

Figure 3.1: Critical interlayer separation *vs*. the electron-hole mass ratio. Above the curves no biexciton formation is possible. The circles are our results. The squares are from Ref. [40]. The triangles correspond to d above which $E_B(d)$ drops below $10^{-3}\,\mathrm{Ry}_e$, making biexcitons irrelevant in experimental practice.

is the mass ratio. Similarly, the single-exciton Hamiltonian is

$$H_X = T_1 + v(\mathbf{r}_1 - \mathbf{R}_1, d)\,. \tag{3.8}$$

The problem is characterized by two dimensionless parameters: d and σ. The case of $d = 0$ (direct excitons) has been studied extensively. [35, 36, 37] In contrast, high accuracy calculations of E_B for $d > 0$ have been carried out only in the aforementioned Ref. [33]. The authors of that work have employed the diffusion quantum Monte-Carlo method (DMC). Away from $d = 0$, they were able to fit their results for $\sigma = 1$ and $\sigma = 1/2$ to the exponential:

$$E_B(d) \approx \alpha e^{-\beta d}. \tag{3.9}$$

This result is surprising. Equation (3.9) seems to imply that the biexcitons are stable at any d, i.e., $d_c = \infty$. On the other hand, physical intuition and previous approximate calculations [38, 39] suggest that d_c should be finite. A more recent work [40] has reached the same conclusion. We present rigorous analytical arguments and essentially exact numerical results proving that $d_c \leq 1$ at all σ, see Fig. 3.1. (Due to electron-hole symmetry, it is sufficient to consider $0 \leq \sigma \leq 1$.)

Since d_c is finite, the interpolation formula (3.9) must overestimate the binding energy at large d. We show that near the biexciton dissociation threshold,

$$d_c - d \ll D\,, \tag{3.10}$$

where $D \sim 1$ for $\sigma \sim 1$ and $D \sim \exp(-\sigma^{-1/2})$ for $\sigma \ll 1$, function $E_B(d)$ behaves as

$$E_B \simeq E_0 e^{-D/(d_c - d)}. \tag{3.11}$$

This equation resembles the well-known expression for the energy ε of a bound state in a weak two-dimensional potential $V(r)$. Such a state exists if

$$W \equiv \frac{M}{2\pi\hbar^2} \int d^2 r V(r) < 0\,, \tag{3.12}$$

where M is the mass of the particle. Near the threshold $W \to 0$ one finds [41]

$$|\varepsilon| \propto e^{-1/|W|}, \quad |W| \ll 1\,. \tag{3.13}$$

The exciton-exciton interaction potential $V(r)$ in general does not satisfy the condition of the perturbation theory $V(r)r^2 \ll \hbar^2/M$, with $M = m_e + m_h$. Therefore, Eq. (3.13) does not literally apply here. Nevertheless, the physical origins of the exponential dependence in Eqs. (3.11) and (3.13) are the same, see Sec. 3.2B.

We verify and complement the above analytical results numerically using the stochastic variational method (SVM). [19] The SVM has proven to be a powerful technique for computing the energies of few-particle systems. [42] For example, it has given the best estimates of E_B for direct biexcitons, [35, 36] $d = 0$. Our calculations are largely in excellent agreement with those of Ref. [33], see Fig. 3.2 and Table 3.1. Thus, Eq. (3.9) is certainly useful as an interpolation formula for not too large d. However, near the estimated d_c, our results favor Eq. (3.11) over Eq. (3.9). Since the SVM is variational, we can be sure that it is more reliable when it gives a larger E_B than other methods.

The remainder of this chapter is organized as follows. In Sec. 3.2 we derive a few analytical bounds on E_B and the asymptotic formula (3.11). Numerical calculations are presented in Sec. 3.3. Section 3.4 is devoted to discussion and comparison with results in previous literature. Some details of the derivation are given in Appendices A and B.

3.2 Analytical results

In this section we approach the biexciton problem by analytical methods. Since the exact solution seems out of reach, the best one can do is to consider certain limits where suitable control parameters exist. Below we examine three of them. First, we study large-d excitons. We prove that they cannot bind into a stable biexciton. Second, we consider the immediate vicinity $d_c - d \ll 1$ of the dissociation threshold d_c. We derive the asymptotical formula for the binding energy, Eq. (3.11), which is valid for arbitrary σ. Finally, we analyze the case $\sigma \ll 1$.

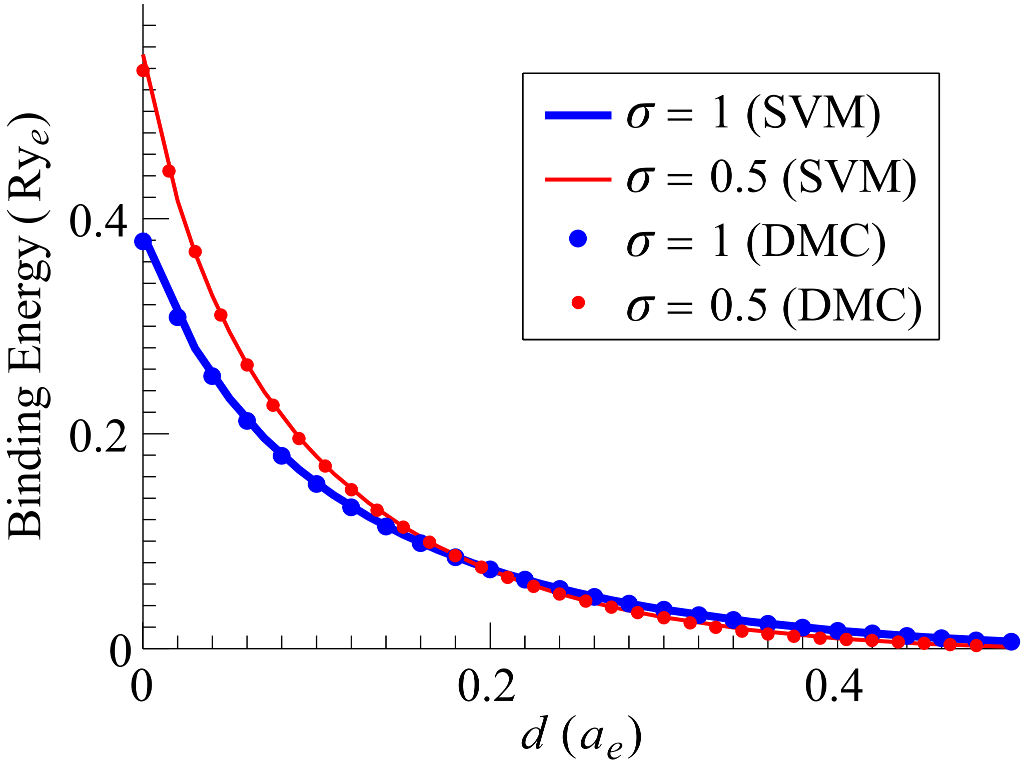

Figure 3.2: Binding energy of biexciton vs. the distance between the quantum wells for the mass ratios $\sigma = 1$ and 0.5. Our results using the stochastic variational method (SVM) are shown by the solid lines. The dots using diffusion Monte-Carlo (DMC) are from the Ref. [33].

Table 3.1: Biexciton binding energies in units of Ry_e from the previous ("DMC", Ref. [33]) and present ("SVM") work.

	$\sigma = 1$			$\sigma = 0.5$	
$d(a_e)$	DMC	SVM	$d(a_e)$	DMC	SVM
0.000	0.3789	0.3858	0.000	0.5381	0.5526
0.020	0.3084	0.3089	0.015	0.4443	0.4450
0.040	0.2538	0.2546	0.030	0.3695	0.3689
0.060	0.2118	0.2133	0.045	0.3104	0.3109
0.080	0.1794	0.1807	0.060	0.2639	0.2649
0.100	0.1532	0.1542	0.075	0.2265	0.2275
0.120	0.1315	0.1324	0.090	0.1956	0.1966
0.140	0.1135	0.1141	0.105	0.1696	0.1707
0.160	0.0982	0.0986	0.120	0.1477	0.1487
0.180	0.0851	0.0855	0.135	0.1291	0.1299
0.200	0.0738	0.0742	0.150	0.1130	0.1136
0.220	0.0640	0.0644	0.165	0.0989	0.0995
0.240	0.0556	0.0559	0.180	0.0865	0.0872
0.260	0.0483	0.0485	0.195	0.0757	0.0764
0.280	0.0418	0.0420	0.210	0.0663	0.0670
0.300	0.0361	0.0363	0.225	0.0580	0.0586
0.320	0.0311	0.0313	0.240	0.0507	0.0512
0.340	0.0267	0.0270	0.255	0.0443	0.0447
0.360	0.0229	0.0231	0.270	0.0385	0.0389
0.380	0.0195	0.0197	0.285	0.0333	0.0337
0.400	0.0165	0.0167	0.300	0.0286	0.0291
0.420	0.0140	0.0141	0.315	0.0241	0.0250
0.440	0.0117	0.0118	0.330	0.0200	0.0214
0.460	0.0096	0.0097	0.345	0.0165	0.0182
0.480	0.0078	0.0079	0.360	0.0135	0.0154
0.500	0.0063	0.0065	0.375	0.0112	0.0129
0.520	0.0051	0.0052	0.390	0.0096	0.0107
0.540	0.0040	0.0040	0.405	0.0087	0.0087
0.560	0.0030	0.0031	0.420	0.0076	0.0071
0.580	0.0021	0.0023	0.435	0.0064	0.0056
0.600	0.0013	0.0017	0.450	0.0051	0.0044
0.620	0.0007	0.0012	0.465	0.0039	0.0033
0.640	0.0002	0.0007	0.480	0.0027	0.0024

3.2.1 Exciton interaction at large d

The absence of stable biexcitons at large d is due to the lack of binding in the classical limit, which is realized at such d. Indeed, if we temporarily change the length units to d and energy units to $e^2/\kappa d$, then the potential energy U in Eq. (3.5) becomes d-independent while the kinetic energy T acquires the extra factor $a_e/d \ll 1$ compared to Eq. (3.4). Hence, the potential energy dominates. A rigorous proof that $d_c < \infty$ can be constructed by dealing with the quantum and many-body aspects of the problem separately. The many-body part is handled at the classical level. Thereafter the quantum corrections are included. With further analysis, both parts of the argument can be reduced to simpler problems for which controlled approximations exist.

Since the Earnshaw theorem does not apply in two dimensions, the absence of a stable classical biexciton is not immediately obvious. However, we verified it following these steps. The classical ground-state is the global minimum of the potential energy. We can perform the minimization over the electron positions $\mathbf{r}_1$ and $\mathbf{r}_2$ first. Let $\mathbf{R}$ be the distance between the holes,

$$\mathbf{R} = \mathbf{R}_1 - \mathbf{R}_2\,, \tag{3.14}$$

then the energy function to minimize is (in the original units convention)

$$U_R = \frac{2}{|\mathbf{r}_1 - \mathbf{r}_2|} + \frac{2}{R} - \sum_{\substack{j=1,2\\ \mathbf{t}=\pm\mathbf{R}/2}} v(\mathbf{r}_j - \mathbf{t}, d)\,. \tag{3.15}$$

It can be shown that for all R the lowest energy is achieved when the in-plane coordinates of the four charges fall on a straight line, see Fig. 3.3. Forming a cross is the only other viable alternative, but it always has a higher energy. For the linear geometry of the system, numerically exact results for $U_{\min}(R, d) \equiv \min_{\mathbf{r}_1,\mathbf{r}_2} U_R$ are obtained trivially. The plot of $V_{\text{cl}}(R) \equiv U_{\min}(R, d) + (4/d)$ is shown in Fig. 3.3. This combination can be thought of as the classical limit of the exciton interaction potential $V(R)$. Function V_{cl} monotonously decreases with R and achieves its global minimum at $R = \infty$. This means that classical excitons do not form a bound state.

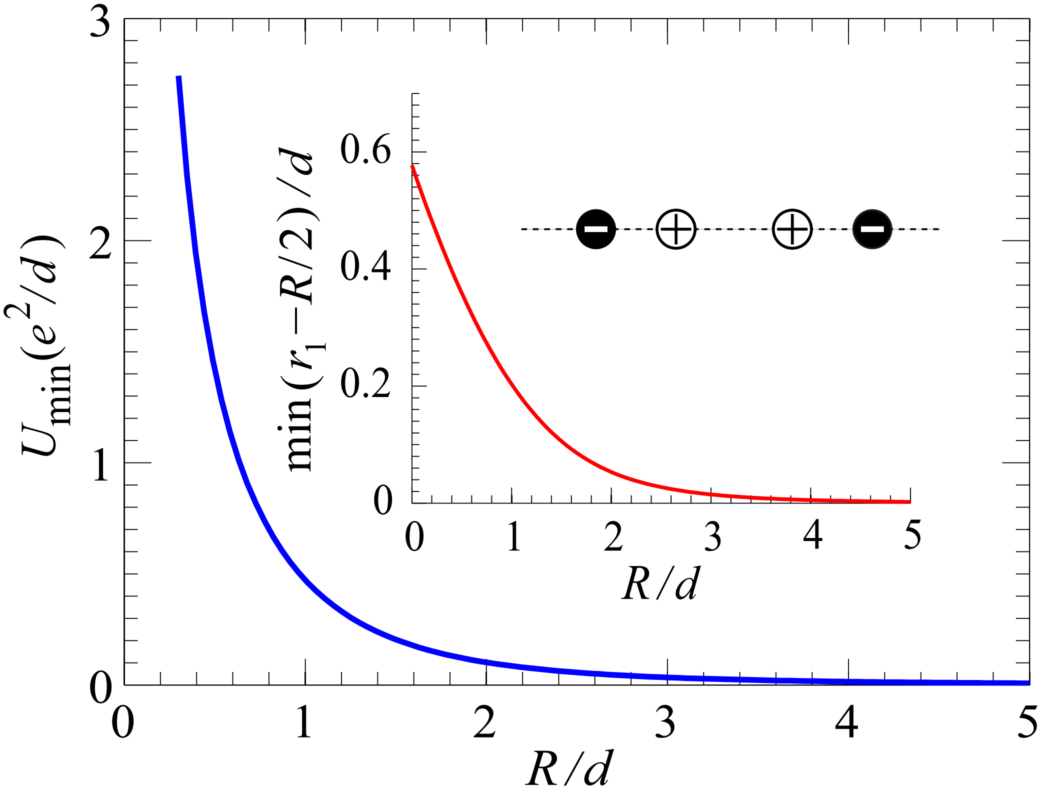

Figure 3.3: Main panel: ground-state energy $U_{\rm min}$ *vs*. the separation R of holes for a pair of classical excitons. In this state all four charges are on the same straight line. Inset: in-plane distance between nearest electrons and holes *vs*. R.

At large R, function $V_{\text{cl}}(R)$ follows the dipolar interaction law (3.1) with the quadrupolar, *etc.*, corrections:

$$V_{\text{cl}}(R, d) = \frac{2d^2}{R^3} - \frac{3}{2}\frac{d^4}{R^5} + \mathcal{O}\left(\frac{d^6}{R^7}\right), \quad R \gg d\,. \tag{3.16}$$

Quantum corrections due to the zero-point motion about the classical ground state are not able to compete with the dipolar repulsion when d is large, see Appendix A. Therefore, there is a critical $d_c = d_c(\sigma)$ above which a stable biexciton does not exist.

3.2.2 Binding energy near d_c

In this subsection we examine the biexciton state near the dissociation threshold d_c for arbitrary σ. It is easy to understand that in this regime the biexciton orbital wavefunction Ψ should have a long tail extending to large distances away from the center of mass of the the system. Inside of this tail the configurations of electrons and holes resemble a pair of well-separated individual excitons. Therefore, at $r \gg 1$, where r is the distance between the centers of mass of two such excitons, Ψ takes the asymptotic form

$$\Psi = [1 + (-1)^s P_{12}]\, \Phi(\mathbf{r}) \prod_{j=1,2} \phi_\sigma(\mathbf{r}_j - \mathbf{R}_j)\,, \tag{3.17}$$

$$\mathbf{r} = \frac{1}{1+\sigma}\mathbf{R} + \frac{\sigma}{1+\sigma}(\mathbf{r}_1 - \mathbf{r}_2)\,. \tag{3.18}$$

Here s is the total electron spin, ϕ_σ is the ground-state wavefunction of a single exciton with mass ratio σ, and operator P_{12} exchanges $\mathbf{r}_1$ and $\mathbf{r}_2$. Let us assume, for simplicity, that holes are spin-1/2 particles. Then the wavefunction Φ of the relative motion must have the parity $\Phi(-\mathbf{r}) = (-1)^{s+S}\Phi(\mathbf{r})$, where S is the total spin of the holes. Our goal in this subsection is to determine the behavior of Φ at large r and use it to derive Eq. (3.11).

We proceed, as usual, by expanding Φ into partial waves of angular momenta m (m and $s + S$ must be simultaneously odd or even). The equation for the radial wavefunction $\chi_m(r)$ reads

$$-\frac{1}{r}\frac{d}{dr}r\frac{d\chi_m}{dr} + \left[\varkappa^2 + \mu V(r) + \frac{m^2}{r^2}\right]\chi_m = 0\,, \tag{3.19}$$

where $\varkappa$ and μ are defined by

$$\varkappa = \sqrt{\mu E_B}\,, \quad \mu = \frac{1+\sigma}{2\sigma}\,. \tag{3.20}$$

At small distances, potential $V(r)$ is either ill-defined or complicated, but for $r \gg d$ it obeys the dipolar law $V(r) = 2d^2/r^3$ [Eq. (3.1)]. From this, it is easy to see that $\mu V(r) r^2 \ll 1$ at $r \gg b$ with b given by

$$b = 8\mu d^2\,. \tag{3.21}$$

At such r the potential energy V acts as a small perturbation. [41] Therefore, $\chi_m(r)$ coincides with the wavefunction of a free particle,

$$\chi_m(r) = c_1 K_m(\varkappa r)\,, \quad r \gg b\,. \tag{3.22}$$

Note that b is either of the order or much larger than d because $\mu \geq 2$ and $d \simeq d_c \sim 1$.

Sufficiently close to the critical d, we have $\varkappa \ll 1/b$. In this case there exists an interval of distances $b \ll r \ll b^{1/3}\varkappa^{-2/3}$ where we can drop the term $\varkappa^2$ in Eq. (3.19) compared to $\mu V(r)$. After this, Eq. (3.19) admits the solution

$$\chi_m(r) = I_{2m}\left(\sqrt{\frac{b}{r}}\right) - 4c_2 K_{2m}\left(\sqrt{\frac{b}{r}}\right)\,, \tag{3.23}$$

where $I_{2m}(z)$ and $K_{2m}(z)$ are the modified Bessel function of the first and the second kind, respectively. [43] The unit coefficient for $I_{2m}(z)$ and the factor of (-4) in front of c_2 are chosen for the sake of convenience. The ground-state solution is obtained for $m = 0$. Using the asymptotic expansion [43] of I_0 and K_0 in Eqs. (3.22) and (3.23), and demanding them to be consistent with one another, we find for $m = 0$ and $b \ll r \ll \varkappa^{-1}$:

$$\chi_0 = 1 - 2c_2\left[\ln\left(\frac{4r}{b}\right) - 2\gamma\right] + \mathcal{O}\left(\frac{b}{r}\right)\,, \tag{3.24}$$

$$c_2 = -\frac{1}{6\gamma + 2\ln(b\varkappa/8)} = \frac{1}{\ln(E_0/E_B)}\,, \tag{3.25}$$

where

$$E_0 = \frac{8}{e^{6\gamma}}\left(\frac{\sigma}{1+\sigma}\right)^3 \frac{1}{d^4}\,. \tag{3.26}$$

Here $\gamma = 0.577\ldots$ is the Euler-Mascheroni constant. [43] Equation (3.24) specifies the boundary condition to which the solution for χ_0 in the near field, $r \lesssim b$, must be matched.

At $d = d_c$, both $\varkappa$ and c_2 vanish. Wavefunction $\chi_0(r)$ at small $\varkappa$ can be viewed as the wavefunction for $d = d_c$ perturbed by the small change in the boundary condition in the far field, $r \gtrsim b$, and by another perturbation,

$$\varkappa^2 + \mu V(r)|_{d_c}^{d}\,,$$

in the near field, $r \lesssim b$. To the first order in these perturbations we have

$$E_B = -Ac_2 + B(d, \varkappa^2)\,, \tag{3.27}$$

where A is a constant and B is a smooth function subject to the condition $B(d_c, 0) = 0$. Expanding B to the first order in $d_c - d$ and $\varkappa^2$, we arrive at the transcendental equation for E_B:

$$\left(1 - \mu\frac{\partial B}{\partial \varkappa^2}\right) E_B + \frac{A}{\ln(E_0/E_B)} = -\frac{\partial B}{\partial d}\,(d_c - d)\,. \tag{3.28}$$

The solution cannot be written in terms of elementary functions. However, the logarithmic term gives the sharpest dependence on E_B. Hence, at small E_B the first term on the left-hand side of Eq. (3.28) can be dropped. Now this equation can be easily solved to recover Eq. (3.11) with

$$D = \frac{A}{C}\,, \quad C = -\frac{\partial B}{\partial d}\,. \tag{3.29}$$

The coefficients A and C must be determined from the solution of the inner problem. For $\sigma \ll 1$ part of this task can be accomplished analytically, as explained later in this section. For $\sigma \sim 1$ a numerical solution, such as the one discussed in Sec. 3.3, seems to be the only alternative.

Our results comply with a general theorem, [44] which states that in the asymptotic limit $k = i\varkappa \to 0$ the scattering phase shift $\delta(k)$ satisfies the equation

$$(\pi/2)\cot\delta(k) = \ln(k/2) + f(k^2)\,, \tag{3.30}$$

where $f(z)$ is some analytic function. This theorem is valid for a general short-range potential in two dimensions. For a bound state $\cot\delta(k)$ should be replaced by i, leading to

$$\ln\left(\sqrt{\mu E_B}/2\right) + f(-\mu E_B) = 0\,, \tag{3.31}$$

which is in agreement with our Eq. (3.28). Our derivation has the advantage of showing that the proper dimensionless combination in the argument of the logarithm is $\sqrt{E_B/E_0}$ and that the asymptotic behavior (3.11) is realized at $E_B \ll E_0$.

3.2.3 Binding energy for small mass ratios

Although the electron-hole mass ratio is not truly small in typical semiconductors, it is interesting to examine the case $\sigma \ll 1$ from the theoretical point of view. At such σ the exciton interaction potential V can be meaningfully defined at all distances using the Born-Oppenheimer approximation (BOA). [45, 46] In addition, the radial wavefunction can be computed everywhere with accuracy $\mathcal{O}(\sigma)$.

The distance r between excitons is no longer a physically reasonable variable when the four particles approach each other closely and their partitioning into excitons becomes ambiguous. In the BOA this problem is mitigated by selecting R — the distance between the heavy charges — to be the radial coordinate of choice. The ground-state biexciton wavefunction is taken to be

$$\Psi = \chi(R)\varphi(\mathbf{R}, \mathbf{r}_1, \mathbf{r}_2)\,, \tag{3.32}$$

where φ is the ground-state of two interacting electrons subject to the potential of two holes fixed at positions $\mathbf{R}_{1,2} = \pm\mathbf{R}/2$:

$$H_{\mathrm{BOA}}\varphi = \left[-\nabla_1^2 - \nabla_2^2 + U_R(\mathbf{r}_1, \mathbf{r}_2)\right]\varphi = U_{\mathrm{BOA}}\varphi\,. \tag{3.33}$$

Here $U_{\mathrm{BOA}}(R)$ is the corresponding energy. In turn, $\chi(R)$ is found from

$$-\frac{1+\sigma}{R}\frac{d}{dR}R\frac{d\chi}{dR} + \mu\left[U_{\mathrm{BOA}}(R) - E_{\mathrm{BOA}}\right]\chi = 0\,. \tag{3.34}$$

The BOA is known to have $\mathcal{O}(\sigma)$ accuracy. In principle, it can be systematically improved. [47] However, since below we will be solving Eq. (3.34) by means of the quasiclassical approximation, which itself is known to be accurate only up to $\mathcal{O}(\sigma)$, this is unwarranted.

Dropping all inessential $\mathcal{O}(\sigma)$ terms, we can simplify Eq. (3.34) as follows:

$$-\frac{1}{R}\frac{d}{dR}R\frac{d\chi}{dR}+\left[\varkappa^2+\mu V(R)\right]\chi=0\,, \tag{3.35}$$

$$V(R)\equiv U_{\mathrm{BOA}}(R)-U_{\mathrm{BOA}}(\infty)\,. \tag{3.36}$$

Our task is to solve this equation with boundary conditions $|\chi(0)|<\infty$ at the origin and

$$\chi(R)\simeq I_0\left(\sqrt{\frac{b}{R}}\right)-4c_2K_0\left(\sqrt{\frac{b}{R}}\right) \tag{3.37}$$

at $b\ll R\ll b^{1/3}\varkappa^{-2/3}$, with c_2 given by Eq. (3.25).

We reason as follows: in order to have a bound state, potential $V(R)$ must be negative over some range of R. It can be shown that this occurs in a single contiguous interval, see Fig. 3.4 and Sec. 3.3. Inside of this interval there is a classically allowed region, $\mu V(R)<-\varkappa^2$, where function $\chi(R)$ reaches a maximum. As we approach the dissociation threshold, this region shrinks. Near the threshold it becomes very narrow, so that the quadratic approximation

$$\mu V(R)\simeq-\varkappa^2+\frac{1}{2}\mu V''\,(R-R_-)(R-R_+) \tag{3.38}$$

becomes legitimate. Here R_- and R_+ are the turning points. To construct the desired solution we simply need to match $\chi(R)$ in the classical region, $R_-<R<R_+$, inside the tunneling region, $R_+\ll R\ll b$, and in the far field, $R\gg b$. Details of this calculation are outlined in Appendix B. The result is

$$A=4\left(\frac{\pi}{e}\sigma V''\right)^{1/2}\exp(-2S_0)\,, \tag{3.39}$$

$$S_0=\frac{1}{\sqrt{2\sigma}}\int\limits_{R_+}^{\infty}dR\sqrt{V(R)}\,, \tag{3.40}$$

$$B=|V(R_0)|-\sqrt{\sigma V''}\,, \tag{3.41}$$

where $R_0=(R_++R_-)/2$ is the point where $V(R)$ has the minimum.

Equations (3.29) and (3.39) imply that the coefficient D in Eq. (3.11) and the range of d [Eq. (3.10)], where Eq. (3.11) applies, is proportional to the exponentially small factor e^{-2S_0} at $\sigma\ll1$. We expect that D grows with σ and by extrapolation, reaches a number of the order of unity at $\sigma\sim1$.

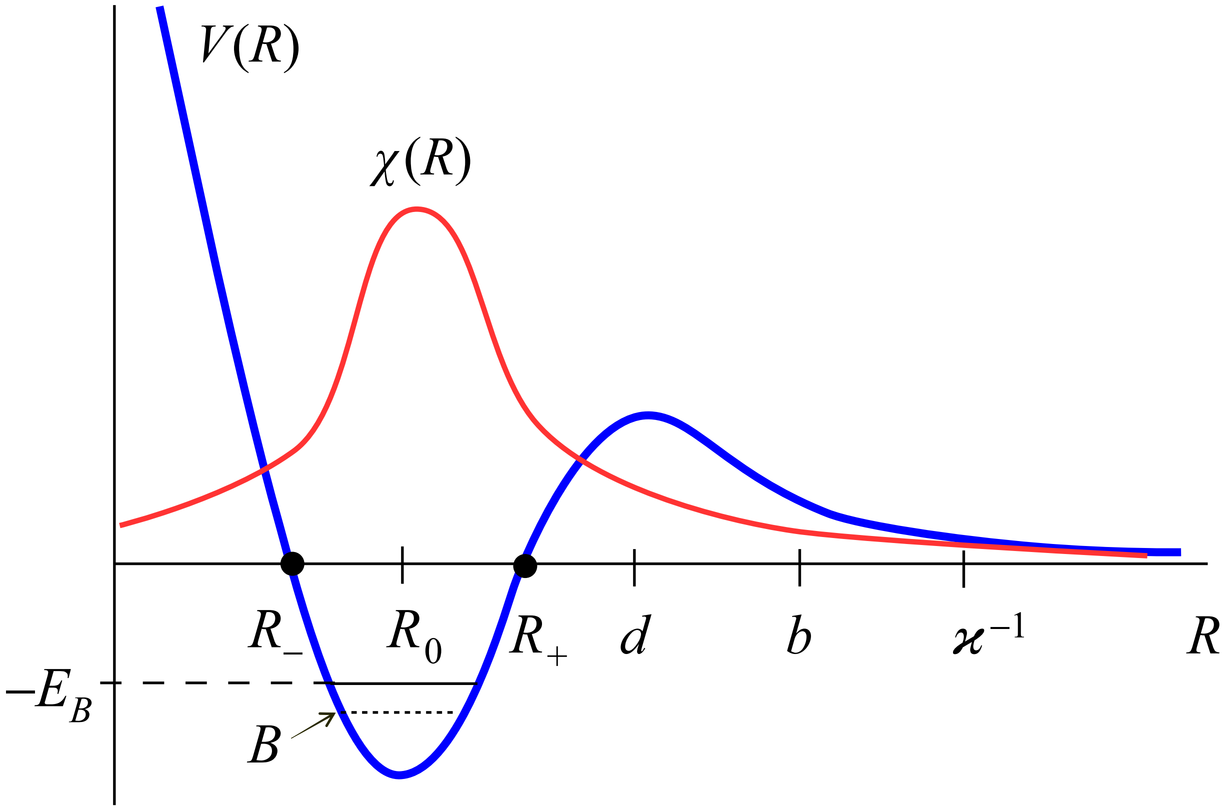

Figure 3.4: Sketch of the interaction potential $V(R)$ and the exciton wavefunction $\chi(R)$ for the Born-Oppenheimer limit $\sigma \ll 1$.

A few other properties of function $d_c(\sigma)$ can also be deduced analytically. For example, Eq. (3.41) implies that

$$d_c(0) - d_c(\sigma) \propto \sqrt{\sigma}\,, \quad \sigma \ll 1\,. \tag{3.42}$$

Hence, $d_c(\sigma)$ has an infinite derivative at $\sigma = 0$ and so initially decreases with σ. At some σ, however, $d_c(\sigma)$ must start to increase. Indeed, due to the electron-hole symmetry, the combination $d_c(\sigma)/(1+\sigma)$ must have a vanishing derivative [48] at $\sigma = 1$. Therefore,

$$d_c'(1) = d_c(1)/2 > 0\,. \tag{3.43}$$

Finally, we have a strict upper bound [48]

$$d_c(\sigma) \leq (1+\sigma) d_c(0)\,. \tag{3.44}$$

All of these properties are borne out by our Fig. 3.1. Still, a purely analytical solution of the biexciton problem does not appear to be possible at any σ. In the next section, we approach it by numerical calculations.

3.3 Numerical simulations

In order to verify our analytical predictions and other results in the literature [33, 40], we have carried out a series of numerical calculations using the SVM. To implement this method we customized the published SVM computer code [20] for the problem at hand. In the SVM one adopts a nonorthogonal basis of correlated Gaussians in the form [42]

$$G_n = \exp\left(-\frac{1}{2}\mathbf{x}^\dagger \mathbf{B}_n \mathbf{x}\right)\,, \tag{3.45}$$

from which a variational wavefunction of given electron and hole spins (S and s, respectively) is constructed:

$$\psi = \mathcal{A}\left[G_n(\{\mathbf{r}_\nu\})\Upsilon_{S,s}\right]\,. \tag{3.46}$$

Here $\mathbf{x}$ is a 3×1 vector of Jacobi coordinates (linear combinations of differences in particle coordinates in which the kinetic energy separates), $\mathbf{B}_n$ is a positive-definite

3×3 matrix, $\mathcal{A}$ is the antisymmetrizer, and $\Upsilon_{S,s}$ is the spin wavefunction. All our SVM calculations are done for the spin-singlet state $S = s = 0$. Note that G_n corresponds to the zero total momentum of the system.

The number of basis states is grown incrementally until the energy is converged or the prescribed basis dimension (typically 700) is reached. At each step a new quadratic form $\mathbf{B}_n$ is generated randomly. If adding the corresponding function G_n to the basis improves the variational energy significantly, this G_n is kept; otherwise, a new $\mathbf{B}_n$ is generated by varying some of its matrix elements. Details can be found in Refs. [42] and [20].

Our numerical results for $\sigma = 0.5$ and $\sigma = 1$ are given in Table 3.1 and plotted in Fig. 3.2. In Fig. 3.5 we replot the binding energy E_B for $\sigma = 1$ in a form suitable for testing Eq. (3.11):

$$\frac{1}{\ln(E_0/E_B)} = \frac{d_c - d}{D} + \frac{(d_c - d)^2}{D_1}\,. \tag{3.47}$$

Here we take into account one more term in the Taylor expansion of the right-hand side of Eq. (3.27) compared to Eq. (3.28). Extrapolation of the data to $E_B = 0$ gives us d_c. The uncertainties in this parameter are estimated by imposing a 95% confidence level on the fit coefficients d_c, D, and D_1. The same procedure has been applied to several other mass ratios in the interval $0.1 < \sigma \leq 1$. The results for d_c are shown in Fig. 3.1. Their comparison with other results in the literature will be addressed in Sec. 3.4.

At $\sigma \leq 0.1$ the range (3.10) of d where Eq. (3.11) applies is exponentially small. Even with our highly accurate numerical method we were not able to probe this range. Thus, we assumed that the nonanalytical correction $Ac_2(E_B)$ is undetectable on the background of E_B in Eq. (3.27), so that our numerical results for $E_B(d)$ at such σ are dominated by the regular contribution

$$E_B = C(d_c - d) + C_1(d_c - d)^2 + \ldots \tag{3.48}$$

Accordingly, at $\sigma \leq 0.1$ we deduced d_c from the fit of $E_B(d)$ to a quadratic polynomial. Additionally, we confirmed that at $\sigma = 0.2$ the two fitting procedures give similar results: $d_c = 0.59 \pm 0.01$ per Eq. (3.47) *vs.* $d_c = 0.58 \pm 0.01$ per Eq. (3.48).

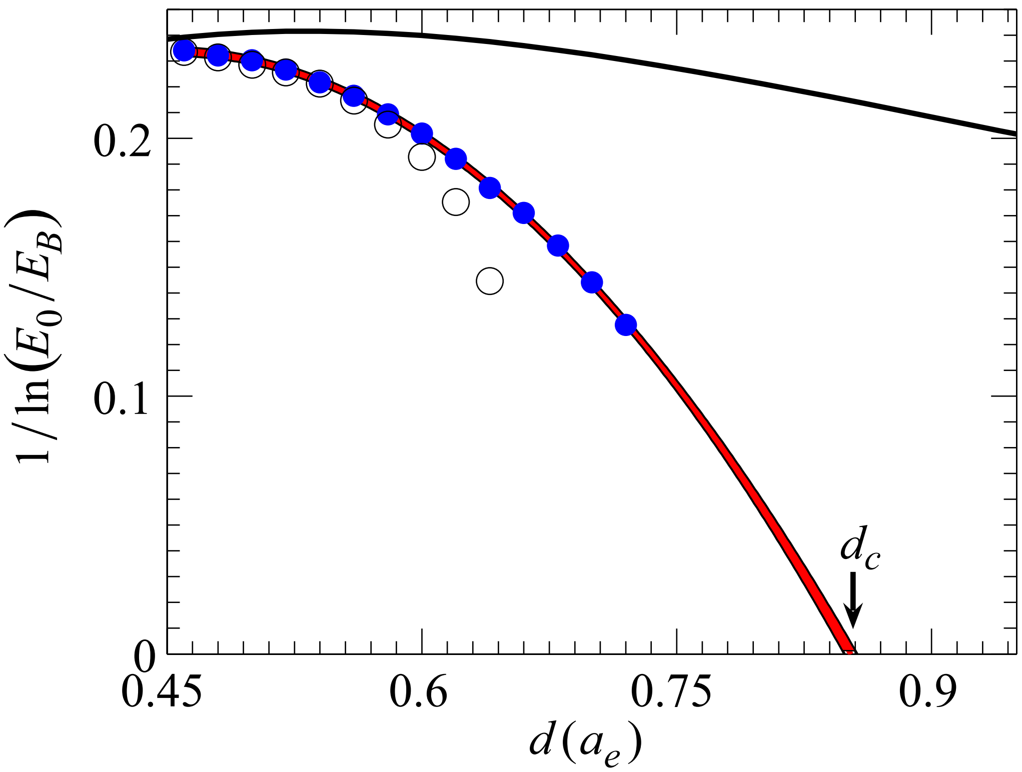

Figure 3.5: Logarithmic plot of the biexciton binding energy as a function of d for $\sigma = 1$. Our results are shown by the filled symbols; the open circles are from Ref. [33]. The thicker line is the fit to Eq. (3.47), which yields $d_c = 0.87 \pm 0.01$ with a 95% confidence level. The other line is Eq. (3.9) with α and β from Ref. [33].

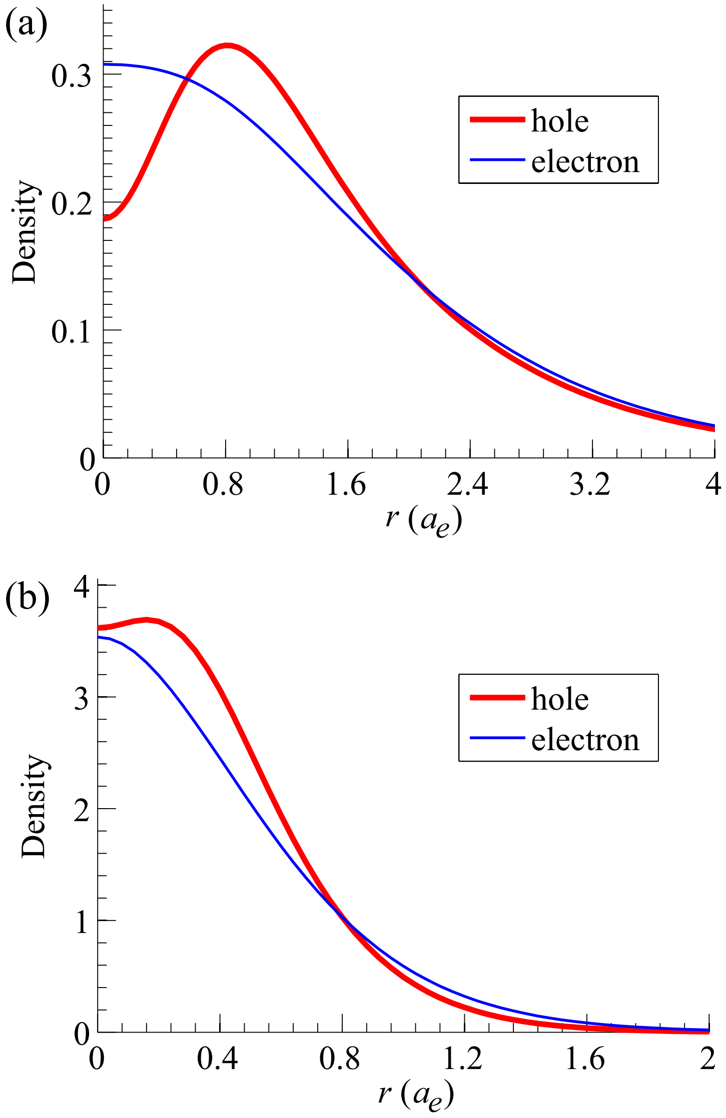

Figure 3.6: (a) Electron and hole density *vs*. the distance to the center of mass in a biexciton with $\sigma = 0.5$ and $d = 0.3$. (b) Same for $\sigma = 0.5$ and $d = 0.0$.

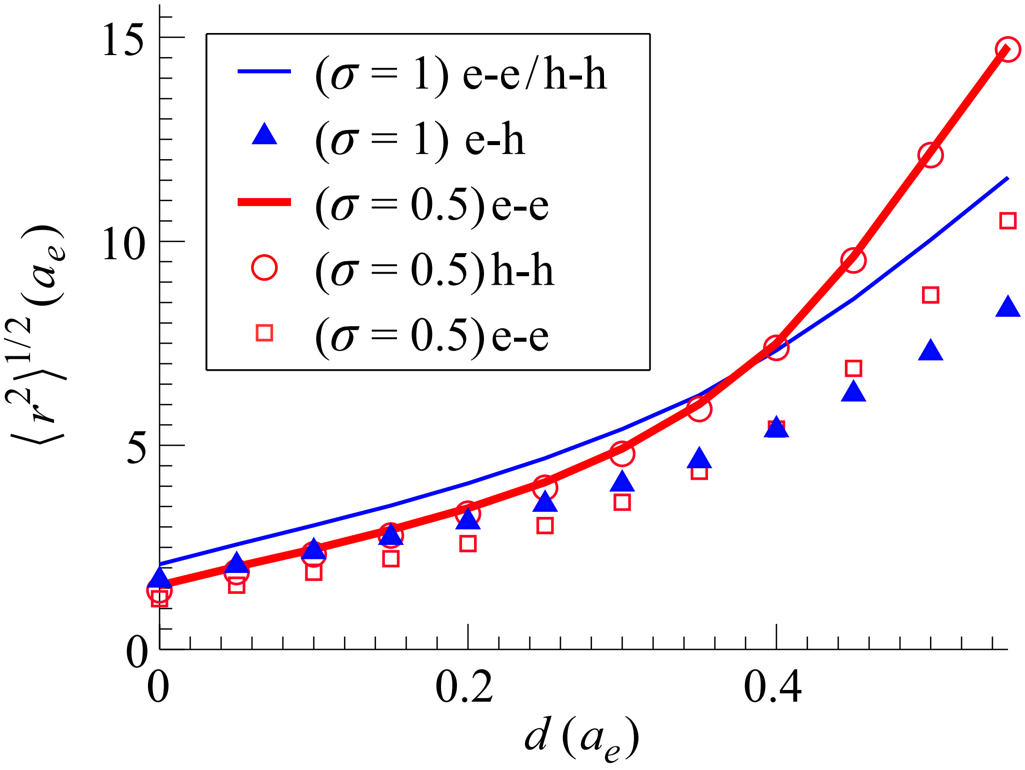

Figure 3.7: Root mean square of the pairwise distances between the biexciton constituents *vs.* d for $\sigma = 0.5$ and $\sigma = 1$. Here $e - e$ is the electron to electron distance, $h-h$ is the hole to hole distance, and $e-h$ is the electron to hole distance.

Finally, we have computed the electron and hole densities in the biexciton as a function of their distance from the center of mass. Examples are presented in Fig. 3.6 for $d = 0.0$ and $d = 0.3$. In the latter case the particles are on average further away from the center of mass. The same trend is also seen in the average root-mean square separations between various particles, which are plotted in Fig. 3.7. Their accelerated growth with d occurs because the biexciton becomes less bound and eventually dissociates.

3.4 Discussion

Let us compare our results with previous theoretical work. Early studies of the biexcitons based on Hartree-Fock [39] or Heitler-London [49] approximations provided initial evidence for the existence of a finite threshold d_c for the biexciton dissociation. However, they gave a considerably lower d_c that we find here because these approximations did not account for all correlation effects essential to the biexciton stability.

Comparing with more recent calculations [33] of the biexciton binding energies by the DMC technique, we find an overall excellent agreement. Still, our SVM occasionally slightly outperforms the DMC, see Table 3.1. Furthermore, in the SVM the estimate of the ground-state energy decreases at each step, so that the statistical noise is never an issue, unlike in the Monte-Carlo methods. Neither the SVM nor the DMC is able to compute arbitrarily small binding energies; therefore, in order to determine d_c, an extrapolation to $E_B = 0$ is necessary. The clarification of what extrapolation formula should be used for this purpose is an important finding of this work. Equation (3.47) represents the true asymptotic behavior in the limit of small E_B and indeed describes our numerical results at such E_B better than the interpolation formula (3.9) plotted alongside for reference.

Another recent theoretical work on biexcitons used a Born-Oppenheimer-like approximation. It differs from the usual adiabatic BOA described in Sec. 3.2 by using the exciton mass $M = m_e + m_h$ instead of the heavy particle mass m_e, i.e., by replacing $1 + \sigma$ by unity in Eq. (3.34). The adiabatic BOA is known to give a strict lower bound on the ground state energy. [50] The approximation of Ref. [40] decreases the kinetic energy and thus lowers the ground state energy E_{XX} even further. On the other hand, our SVM, being a variational method, gives a strict upper bound for E_{XX}. Since the energy of a single exciton E_X is usually computed extremely accurately, our binding energies $E_B = 2E_X - E_{XX}$ should be smaller than those of Ref. [40]. By digitizing Fig. 5 of Ref. [40] we found that this is indeed true for $d > 0.015a_e$ and $\sigma = 0.5$. Accordingly, their estimates of the threshold interlayer separation d_c should exceed ours. Surprisingly, for all σ shown in Fig. 3.1, our d_c are *higher* than those reported in Ref. [40]. The discrepancy is much larger than the uncertainty of d_c from our extrapolation procedure. We suspect that the problem is again related to the manner in which the $E_B \to 0$ extrapolation was performed in Ref. [40]. In any case, a significant discrepancy in d_c is seen only at $\sigma \sim 1$. At small mass ratios, where the approximation of Ref. [40] becomes accurate to the order $\mathcal{O}(\sigma)$, our results are in better agreement.

Turning to the experimental implications of our theory, observations of biexcitons in single quantum well systems have been reported by many experimental groups. [25, 26, 27, 28, 29, 30, 31, 32] In contrast, no biexciton signatures have ever been detected in electron-hole bilayers. Let us discuss how this can be understood based on our results.

The first point to keep in mind is that the biexciton dissociation threshold d_c plotted in Fig. 3.1 is a zero-temperature quantity. For the biexcitons to be observable at finite temperatures, E_B must exceed kT by some numerical factor. (As usual in dissociation reactions, [51] this factor is larger the smaller the exciton density is.) The coldest temperature demonstrated for the excitons in quantum wells is $T \sim 0.1\,\mathrm{K}$ [Ref. [52]]. The maximum separation d_* between the two-dimensional electron and hole layers at which biexcitons are still physically relevant in such structures can be roughly estimated from

$$E_B(d_*) = 10^{-3}\,\mathrm{Ry}_e\,. \tag{3.49}$$

Function $d_*(\sigma)$ is plotted by triangles in Fig. 3.1. In GaAs quantum wells we have [53] $\sigma \approx 0.5$, $a_e = 10\,\mathrm{nm}$, and so $d_* \approx 4.5\,\mathrm{nm}$. In comparison, the smallest center-to-center separation that has been achieved in GaAs/AlGaAs and In-

GaAs/GaAs quantum wells without compromising the sample quality is at least twice as large. [2] Cold gases of indirect excitons have also been demonstrated in AlAs/GaAs structures, [34] in which d is smaller, $d = 3.5\,\text{nm}$. But the electron Bohr radius is also smaller, $a_e \approx 3\,\text{nm}$, so, unfortunately, the dimensionless d is about the same.

A more serious obstacle to the creation and observation of biexcitons is disorder. A rough measure of disorder strength is given by the linewidth of the exciton optical emissions, which is currently $\sim 1\,\text{meV}$, i.e., of the order of $0.1\,\text{Ry}_e$ in GaAs. E_B becomes smaller than this energy scale as soon as d exceeds the thickness of a few atomic monolayers, see Fig. 3.2. Actually, if the disorder were due to a long-range random potential, it might still be possible to circumvent its influence on the measured optical linewidth by interferometric methods such as quantum beats. [27, 29] In reality, a short-range random potential is probably quite significant.

One potentially promising system for the study of the biexciton stability diagram is a single wide quantum well subject to an external transverse electric field. [54] If the well is symmetric and the applied field is zero, we have $d = 0$. A finite field can pull electrons and holes apart, leading to $d > 0$. Of course, for such a structure one should recalculate the stability diagram of Fig. 3.1 by taking into account the motion of particles in all three dimensions.

Although it is challenging to observe the binding of free indirect excitons, in experiments they can be loaded and held together in artificial traps. [55] We anticipate that the SVM can be a powerful tool to study systems of a few trapped excitons theoretically, complementing recent Monte-Carlo work. [56]

To summarize, we have obtained the most accurate estimates to date of the binding energies of two-dimensional biexcitons. Future work may include a refined study of exciton-exciton scattering [40] and interacting excitons in traps.

Recently Lee *et al.* [63] reported a new calculation of the biexciton binding energy E_B as a function of σ by the DMC. This time in order to determine d_c they adopted our interpolation procedure, i.e.,

$$[\ln(E_0/E_B)]^{-1} = -\frac{d_c - d}{D} + \dots$$

These calculations are in excellent agreement with the results of our work at $\sigma >$

0.2. At lower σ, where our method is less accurate, Lee *et al.* were able to find biexciton trial states of slightly higher values of E_B (and therefore slightly higher d_c). According to the variational principle, these values should be considered more accurate than ours.

Chapter 4

Excitons in artificial traps

4.1 Introduction

In order to obtain a more thorough understanding of a physical system, it is advantageous to have as many tunable experimental parameters as possible. These experimental parameters permit a more comprehensive probing of the system in question. In the study of indirect excitons, this may be accomplished by the use of electrostatic traps. These electrostatic traps allow for the creation of variable one-dimensional and two-dimensional potential wells in which the excitons can be trapped and their density controlled. In this chapter, recent experiments using these traps are investigated. These experiments allow for the study of various aspects of the indirect exciton, namely the interexcitonic interaction and the diffusive characteristics of the excitonic gas.

The first set of experiments to be considered investigates indirect excitons in electrostatic lattices, see Figure 4.1. These lattices create a series of one-dimensional potential traps, see Fig. 4.2. As explained in Section 2.3, in experiments without these electrostatic traps, the excitonic gas is localized in the excitation region until a certain density of excitons is reached. It is observed that the electrostatic traps prolong this localization in the spatial direction perpendicular to the traps, since a “potential hill” must be overcome in order to move in the perpendicular direction. Each time a potential hill is traversed, the gas is trapped until the energy reaches the percolation point and “climbs” over the neighboring

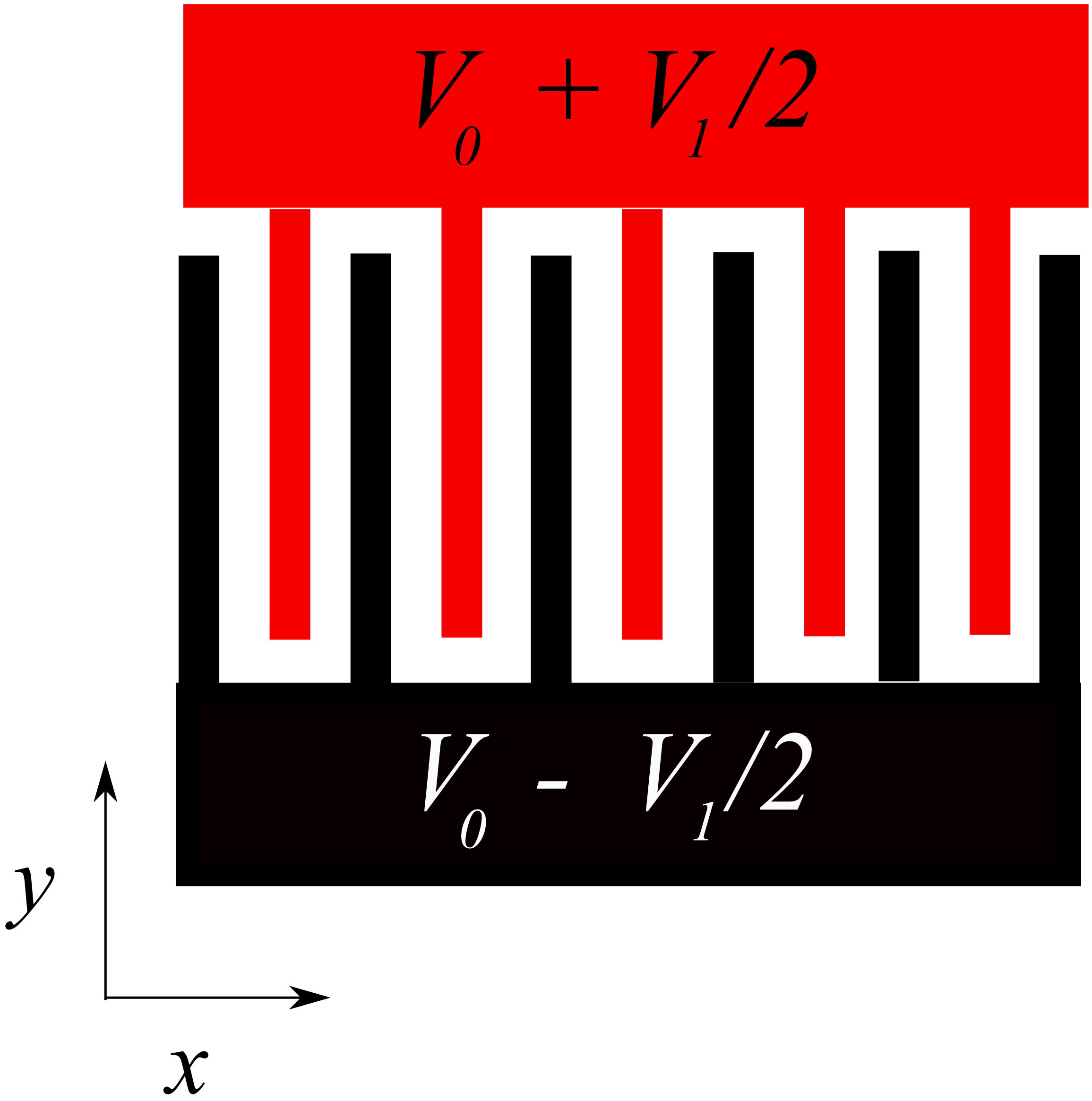

Figure 4.1: Diagram of the electrostatic gates used in the one-dimensional lattice experiments.

"potential hill," see the cartoon in Fig. 4.3. This model is verified in experimental results. In Fig. 4.4 (a) the progress of the gas in the y-direction is greater than in the x-direction where the traps impede the movement, causing the shape of the gas to be oval as opposed to a more circular shape when no traps are present, as seen in Fig. 4.4 (b).

In this chapter, a theoretical model is proposed in which the electrochemical potential

$$\zeta = \mu(x) + U(x) = \text{const}\,, \tag{4.1}$$

is expected to be constant. This is because the diffusion length $L_D = \sqrt{D/R}$ is typically longer than the period of the potential $U(x)$. Hence, the excitons should be able to adjust to the external potential in a quasi-equilibrium fashion, despite their lifetime $1/R$ being finite. With this approximation, one can compute the density as a function of the chemical potential μ. This can in turn be compared with experimental results and an estimate of the excitonic interaction strength, g, is obtained. This estimate is important since the value of the interaction strength remains an open question (see Section 2.3). The exciton-exciton interaction is discussed further in Section 4.3.2.

The experimental setup is similar to that in Section 2.3, with electrostatic gates added as in Fig. 4.1. These gates lead to an electrostatic lattice with an additional electric potential in the x-direction of

$$U(x) = U_0 \cos^2(qx/2)\,, \tag{4.2}$$

as in Fig. 4.2. For this specific experiment, U_0 is set at 1.85 meV and the lattice period is $2\pi/q = 2$ μm.

In the second experiment, a diamond-shaped trap is employed. This leads to a two-dimensional flat-bottomed potential of the form similar to that in Fig. 4.8. The sharpness and depth of this potential well can be closely controlled. In addition, the excitons can be confined in both the x and y directions. This permits a fine-tuning of the density of excitons. As with lattices, this diamond-shaped trap confines the excitons and prolongs their localization.

In this case, the traps are much larger and a static case is no longer valid (the length of the trap exceeds the diffusion length L_D). Therefore, a semi-classical

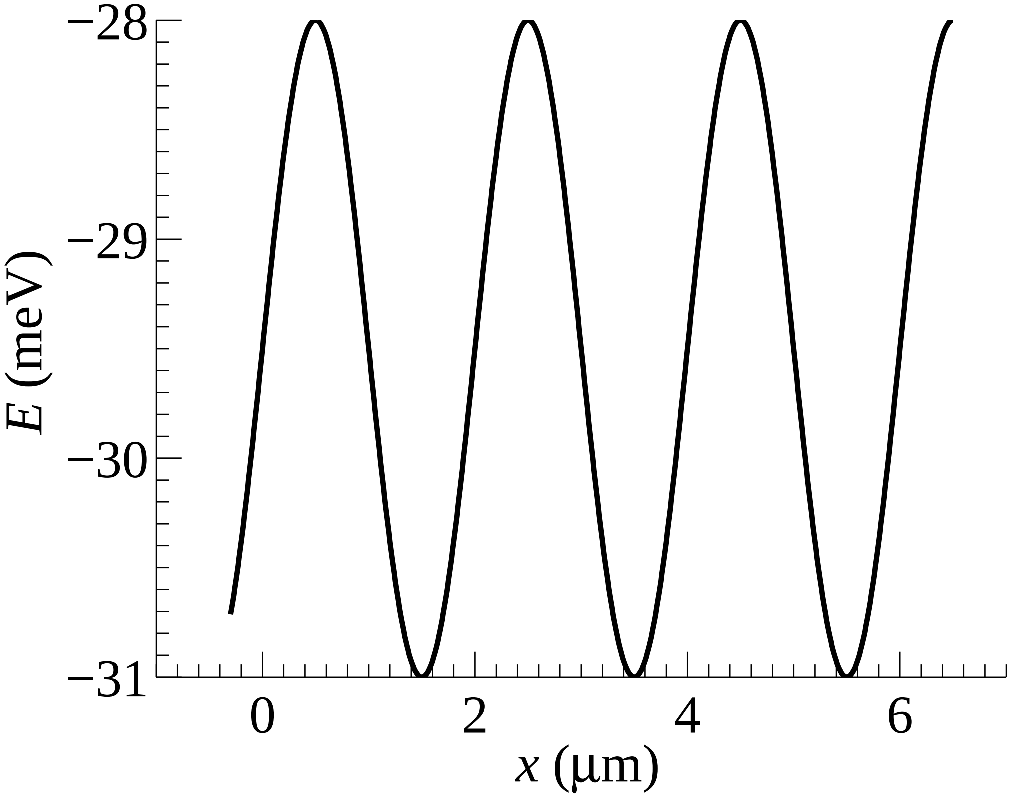

Figure 4.2: One-dimensional lattice with shape as in Eq. (4.2).

drift-diffusion model is employed with equation (similar to Ivanov [24])

$$\frac{\partial n}{\partial t} + \nabla \cdot \mathbf{J_n} + Rn = G, \tag{4.3}$$

where n is the indirect exciton density, R is the recombination rate of indirect excitons, G is the generation rate of indirect excitons, and $\mathbf{J_n}$ is the indirect exciton particle current, given in Eq. (4.16).

Comparing this model with experimental results, one can obtain estimates of the diffusion coefficient D and the interaction strength g. A fundamental theoretical understanding of these excitons is important to the planning and implementation of future experiments with electrostatic traps. What follows is a description of the two theoretical models employed in these experiments and a discussion of theoretical results.

4.2 Discussion

4.2.1 Lattices

Let us make three simplifying assumptions: 1) the lattice potential $U(x) = (U_{\text{lat}}/2)\cos qx$ acting on the excitons can be considered smooth, 2) the excitons are in a state of thermodynamic equilibrium at temperature T, and 3) the photoluminescence signal is collected over a restricted range of transverse momenta $|\mathbf{k}| < Q$, where Q is small enough that it can be treated as zero for calculating exciton energies yet is large enough that the spatial resolution is smaller than the lattice period $2\pi/q$. Under these assumptions, the condition for the equilibrium is that the electrochemical potential is constant:

$$\zeta = \mu(x) + U(x) = \text{const}\,, \tag{4.4}$$

where $\mu(x)$ is the local chemical potential. In turn, the local photoluminescence frequency is determined by

$$\omega(x) = \zeta + E_{\mathbf{k}=0} - \mu(x)\,, \tag{4.5}$$

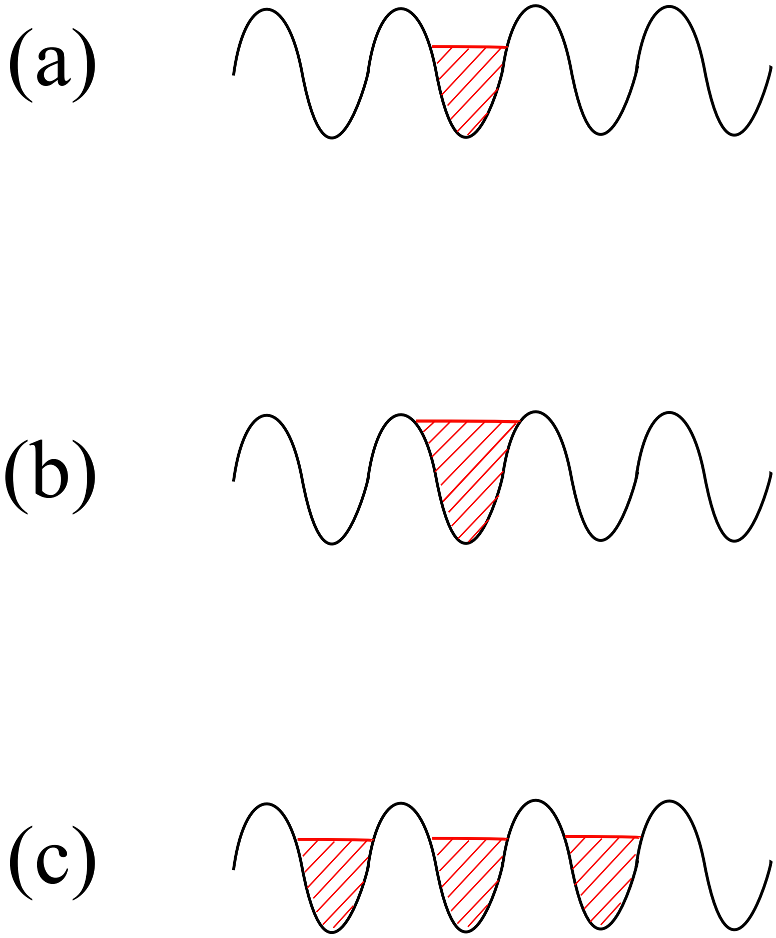

Figure 4.3: Cartoon demonstration of trap dynamics. (a) Excitons are trapped in lattice. As density increases due to laser power increase (b) eventually the excitons reach the percolation point. Finally as the excitons (c) “spill over” into neighboring traps they are again localized.

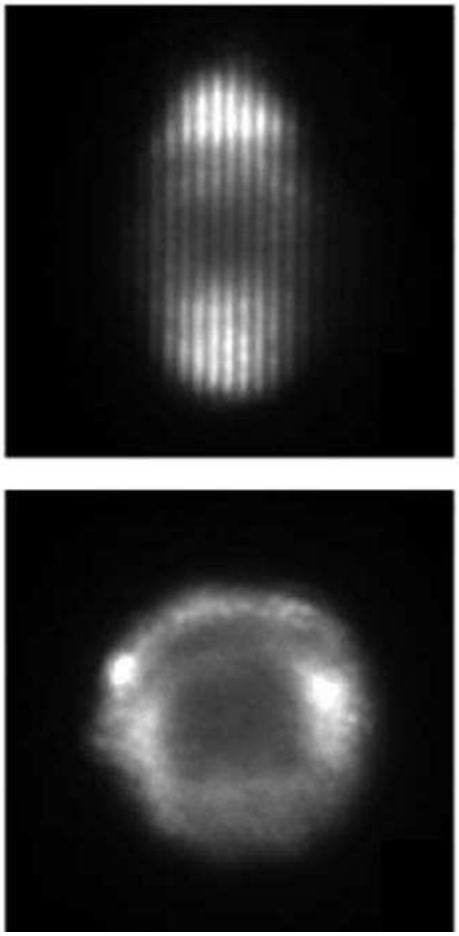

Figure 4.4: Example of two-dimensional photoluminescence pattern from experiment by Butov group. Top: Lattices with $\Delta V = 1.2$ V. Bottom: Lattices with $\Delta V = 0$ V. Temperature is $T = 1.6$ K and excitation power is $P_{ex} = 12\ \mu$W [4].

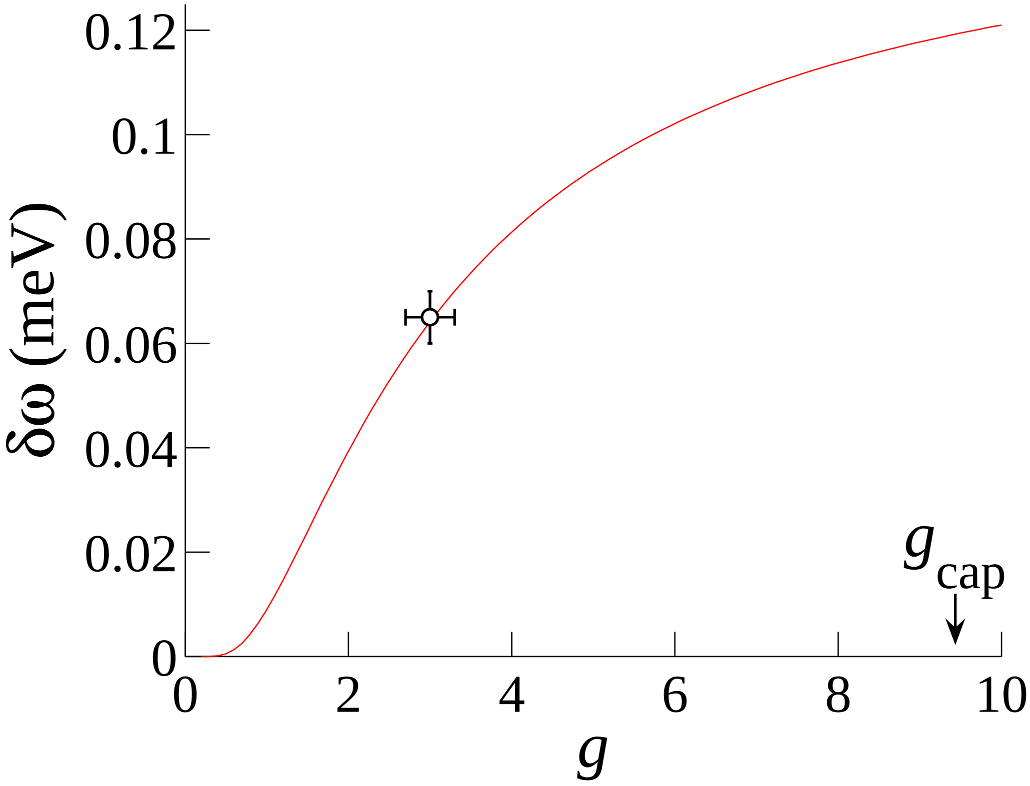

Figure 4.5: The calculated modulation $\delta\omega = \omega_{\mathrm{max}} - \omega_{\mathrm{min}}$ of the photoluminescence frequency as a function of the interaction strength g assuming $k_B T = 0.16$, $U_{\mathrm{lat}} = 3.7$, and $\zeta = 3.7$ (all in meV). The experimental point, shown by the cross, corresponds to $g \approx 3.0$. The value of g predicted by the "capacitor" formula is indicated by the arrow.

where $E_{\mathbf{k}}$ is the single-particle excitation energy in the system, the real part of the pole of the exciton Green's function. Spatially varying $\omega(\mathbf{r})$ is possible only in the normal phase, where

$$E_{\mathbf{k}} = \epsilon_{\mathbf{k}} + \Sigma_{\mathbf{k}} \tag{4.6}$$

remains nonzero (positive). Here $\epsilon_{\mathbf{k}} = \hbar^2 k^2/(2m)$ is the single-particle energy and $\Sigma_{\mathbf{k}}$ is the self-energy. In this case,

$$\omega(x) = \zeta + \Sigma_0 - \mu(x)\,. \tag{4.7}$$

In contrast, in the superfluid phase $E_0 = \mu(x)$ and $\omega(x) = \zeta =$ const, which is apparently not the case experimentally.

Let us find the relation between $\mu(\mathbf{r})$, the local exciton concentration $n(\mathbf{r})$, and Σ_0 in the normal phase. We have:

$$n = \mathcal{G} \int \frac{d^2k}{(2\pi)^2} f(\epsilon_{\mathbf{k}} + \Sigma_{\mathbf{k}} - \mu)\,, \tag{4.8}$$

where $\mathcal{G} = 4$ is the spin degeneracy and $f(\epsilon)$ is the Bose-Einstein distribution function. The interaction has the form

$$\Sigma_{\mathbf{k}} = \int d^2r' V(r - r') n(r')\,,$$

where $V(r - r')$ is the interexcitonic potential and $n(r')$ is the density of excitons. Within the Hartree-Fock approximation,

$$\Sigma_{\mathbf{k}} = V_0 n + \frac{1}{\mathcal{G}} \int \frac{d^2k}{(2\pi)^2} V_{\mathbf{k}-\mathbf{q}} f(E_{\mathbf{q}} - \mu)\,, \tag{4.9}$$

where $V_{\mathbf{k}}$ is the exciton interaction potential. For elementary bosons with short-range interactions, $V_{\mathbf{k}} \simeq V_0$, and therefore

$$\Sigma_{\mathbf{k}} = \left(1 + \frac{1}{\mathcal{G}}\right) V_0 n \equiv \frac{g}{\nu_1} n\,. \tag{4.10}$$

The two terms in parenthesis represent the Hartree and the Fock (exchange) contributions, respectively. Excitons, which are composite bosons, can exchange their constituents, so the Fock term can be somewhat larger.

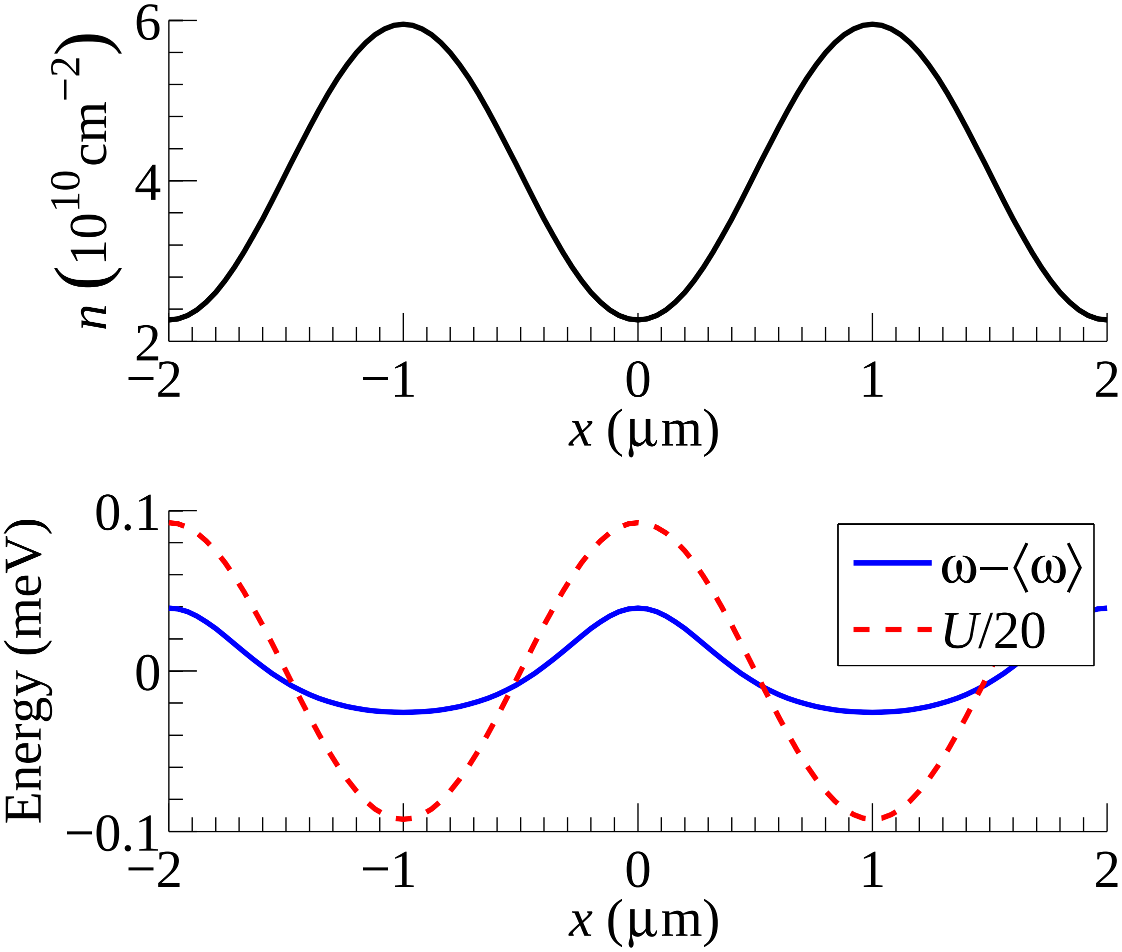

Figure 4.6: Top: Equilibrium density profile in the Hartree-Fock approximation. Bottom: Lattice potential U (divided by 20) and the PL frequency ω (with the average subtracted) *vs.* x.

To characterize the strength of the interaction, we define the dimensionless quantity $g = V_0\nu_1(\mathcal{G}+1)/\mathcal{G}$, where $\nu_1 = m/(2\pi\hbar^2)$ is the density of states per spin species. Note that the "capacitor" formula predicts

$$g_{\text{cap}} = \frac{\mathcal{G}+1}{\mathcal{G}}\frac{2D}{a_e}\left(1+\frac{m_h}{m_e}\right) \approx 9\,, \tag{4.11}$$

see Fig. 4.5.

With the above definition, Eq. (4.10) becomes

$$\Sigma_{\mathbf{k}} = \frac{g}{\nu_1}n\,. \tag{4.12}$$

Substituting this into Eq. (4.8) we have

$$n = \mathcal{G}\int\frac{d^2k}{(2\pi)^2}\frac{1}{\exp[\beta(\epsilon_{\mathbf{k}}+\frac{g}{\nu_1}n-\mu)]-1}.$$

Converting this to an integral over *epsilon* produces

$$n = \mathcal{G}\int_0^\infty d\epsilon\frac{\nu(\epsilon)}{\exp[\beta(\epsilon_{\mathbf{k}}+\frac{g}{\nu_1}n-\mu)]-1}$$

and with a little adjusting,

$$n = \mathcal{G}\nu\int_0^\infty d\epsilon\frac{\exp[-\beta(\epsilon_{\mathbf{k}}+\frac{g}{\nu_1}n-\mu)]}{1-\exp[-\beta(\epsilon_{\mathbf{k}}+\frac{g}{\nu_1}n-\mu)]}\,.$$

Finally we arrive at the transcendental equation for n:

$$n = \frac{\mathcal{G}\nu_1}{\beta}\ln\left[1-\exp\left(\frac{\mu\nu_1-gn}{T\nu_1}\right)\right]\,. \tag{4.13}$$

Given ζ, T, and g, the system of Eqs. (4.4) and (4.13) can be easily solved numerically for each $U(x)$:

$$\exp\left(\frac{\mu\nu_1-gn}{T\nu_1}\right)+\exp\left(-\frac{\beta n}{\mathcal{G}\nu_1}\right) = 1. \tag{4.14}$$

The results for $n(x)$ and $\omega(x)$ are shown in Fig. 4.6. From this calculation we can also determine $\delta\omega \equiv \omega_{\max}-\omega_{\min}$. Treating g as an adjustable parameter, we obtained the dependence $\delta\omega(g)$ plotted in Fig. 4.5. In the experiment $\delta\omega = 0.065\,\text{meV}$ and $\langle\omega\rangle = 3.7\,\text{meV}$, which can be reproduced assuming $\zeta = 3.7\,\text{meV}$ and $g = 3.0$, see Fig. 4.5.

4.2.2 Drift-diffusion model

We start with the two-dimensional quantum diffusion equation

$$\frac{\partial n}{\partial t} + \nabla \cdot \mathbf{J_n} + Rn = G, \tag{4.15}$$

where n is the indirect exciton density, R is the recombination rate of indirect excitons, G is the generation rate of indirect excitons, and $\mathbf{J_n}$ is the indirect exciton particle current

$$\mathbf{J_n} = -D\frac{dn}{d\mu_0}\nabla\left[U + cn + \mu_0(n)\right] , \tag{4.16}$$

where c is a constant representing the exciton-exciton interaction and μ_0 is the "bare" chemical potential (due to kinetic energy only) given by

$$\mu_0(n) = T\ln\left(1 - e^{-n/\mathcal{G}\nu_1 T}\right) = T\ln\left(1 - e^{-T_0/T}\right). \tag{4.17}$$

Here, T_0 is the degeneracy temperature

$$T_0 = \frac{n}{\mathcal{G}\nu_1} , \tag{4.18}$$

where $\mathcal{G}$ is the spin degeneracy and ν_1 is the density of states. Note that c is related to the interaction constant g from Section 4.2.1 by the formula

$$c = \frac{g}{\nu_1}. \tag{4.19}$$

It is illuminating to investigate two limiting cases for Eq. (4.15). First, when the diffusion coefficient D is very large compared to R and G we have

$$\nabla\left[U + cn + \mu_0(n)\right] = 0 \tag{4.20}$$

or

$$U + cn + \mu_0(n) = const\,, \tag{4.21}$$

where this is simply the chemical potential and a restatement of the static case, Eq. (4.4), from Section 4.2.1 where

$$\mu(x) = cn + \mu_0(n)\,. \tag{4.22}$$

In the opposite limit where the diffusion coefficient D is very small compared to R and G, we have

$$Rn = G \tag{4.23}$$

or

$$n = \frac{G}{R} \tag{4.24}$$

in the steady state.

By differentiating Eq. (4.19) we have

$$\frac{dn}{d\mu_0} = \mathcal{G}\nu_1\left(e^{T_0/T} - 1\right). \tag{4.25}$$

If we make the substitutions $\tau = T_0/T$ and $\gamma = \mathcal{G}c\nu_1$, the diffusion equation takes the form

$$\frac{\partial\tau}{\partial t} + \nabla\cdot\mathbf{J}_\tau + R\tau = \frac{G}{\mathcal{G}\nu_1 T}\,, \tag{4.26}$$

with a particle current given by

$$\mathbf{J}_\tau = -D\left(e^\tau - 1\right)\nabla\left[\frac{U}{T} + \gamma\tau + \ln\left(1 - e^{-\tau}\right)\right]. \tag{4.27}$$

This can be rewritten as

$$\mathbf{J}_\tau = -D\left(e^\tau - 1\right)\left(\nabla\frac{U}{T}\right) - D_{eff}\nabla\tau\,, \tag{4.28}$$

with D_{eff} given by

$$D_{eff} = D\left[\gamma(\,e^\tau - 1\,){+}1\right]. \tag{4.29}$$

In the steady state, Eq. (4.26) may be expressed as

$$\nabla\cdot\mathbf{J}_\tau + R\tau = \frac{G}{\mathcal{G}\nu_1 T}\,, \tag{4.30}$$

where $\mathbf{J}_\tau$ is

$$\mathbf{J}_\tau = -D_{eff}\nabla\tau + \mathbf{J_{con}} \tag{4.31}$$

and $\mathbf{J_{con}}$ is

$$\mathbf{J_{con}} = -D\left(e^\tau - 1\right)\left(\nabla\frac{U}{T}\right). \tag{4.32}$$

This set of equations is equivalent to equation 1 from Reference [24]. In the appendix we quickly show this equivalence.

Comparisons of the drift-diffusion model and with experimental results show a qualitative agreement [62]. The experimental results are consistent with an interaction constant of $g = 3$, as in Section 4.2.1. Furthermore, the model leads to a diffusion coefficient on the order of $D \approx 20$ μm [62], which is consistent with previous work [24].

4.3 Appendix

4.3.1 Equivalence of diffusion equation

If we begin with Eq. (4.16) and input our expressions for the chemical potential and for the derivatives of the chemical potential, we have two terms:

$$-D\mathcal{G}\nu_1\left(e^{T_0/T}-1\right)\nabla\left[U+cn\right] \tag{4.33}$$

and

$$-D\mathcal{G}\nu_1\left(e^{T_0/T}-1\right)\nabla\left[T\ln\left(1-e^{-T_0/T}\right)\right]. \tag{4.34}$$

From Ivanov's definition of the mobility,

$$\mu_x = D\left(e^{T_0/T}-1\right)/T_0\,, \tag{4.35}$$

we can rewrite Eq. (4.33) as

$$-\mu_x n\nabla\left[U+cn\right]. \tag{4.36}$$

With the gradient in Eq. (4.34), we can rewrite it as

$$-D\nabla n. \tag{4.37}$$

Finally, Eqs. (4.36) and (4.37) give us

$$-\left(D\nabla n+\mu_x n\nabla\left[U+cn\right]\right)\,, \tag{4.38}$$

which is the indirect exciton particle current term in Reference [24].

4.3.2 Interexcitonic interaction

There is much interest in determining the interaction strength between two indirect excitons. To compute the interaction, we add the interaction of all other indirect excitons:

$$\mathcal{U} = \sum_{j}^{N} V(\mathbf{r} - \mathbf{r}_j). \tag{4.39}$$

Here $V(\mathbf{r} - \mathbf{r}_j)$ is the potential felt between two excitons with a separation of d:

$$V(\mathbf{r} - \mathbf{r}_j) = 2\left(\frac{e^2}{r} - \frac{e^2}{\sqrt{r^2 + d^2}}\right). \tag{4.40}$$

First, one can turn Eq. (4.39) into an integral as such:

$$\mathcal{U} = \sum_{j}^{N} V(\mathbf{r} - \mathbf{r}_j) = \int d^2\mathbf{r}' V(\mathbf{r} - \mathbf{r}') n\left(\mathbf{r}'\right). \tag{4.41}$$

This depends on the density of the excitons. The simplest approximation assumes the density is constant, as in Fig. 4.7. In this case, we have a situation very similar to that of a parallel plate capacitor. One can calculate the energy at the top plate as

$$\psi_{top} = \int d^2 n\mathbf{r}' \left(\frac{e^2}{r} - \frac{e^2}{\sqrt{r^2 + d^2}}\right), \tag{4.42}$$

and the bottom plate as

$$\psi_{bot} = -\int d^2 n\mathbf{r}' \left(\frac{e^2}{r} - \frac{e^2}{\sqrt{r^2 + d^2}}\right). \tag{4.43}$$

Altogether, we have

$$\psi_{top} - \psi_{bot} = \int d^2 n\mathbf{r}' \left(\frac{e^2}{r} - \frac{e^2}{\sqrt{r^2 + d^2}}\right) = \mathcal{U}. \tag{4.44}$$

However, this is also the potential due to a parallel plate capacitor, which we will call U_C. Therefore one can find

$$\mathcal{U} = U_C = \frac{4\pi n e^2 d}{\epsilon}. \tag{4.45}$$

This approximation is referred to as the “capacitor” formula.

4.3.3 Diamond-shaped trap

To analytically model the diamond trap potential, we have

$$w(x) = \begin{cases} L_y(1 - \frac{|x|}{L_x}) & \text{if } |x| < L_x \\ 0 & \text{if otherwise} \end{cases}, \tag{4.46}$$

an arbitrary diamond-shaped pattern in the $x - y$ plane with a length L_x and height L_y. Next, a box shape is created with the function

$$B(x, w, a) = \frac{1}{2}\left[\tanh\left(\frac{x + w}{a}\right) - \tanh\left(\frac{x - w}{a}\right)\right]. \tag{4.47}$$

An example of this box shape is plotted in Fig. 4.9. It has a height of unity, and the sharpness of the box is determined by a. The smaller the value of a the more box-shaped (square) the function will be. The diamond-shaped potential can then be expressed as

$$U(x, y) = -V_{trap}B(y, w(x), a). \tag{4.48}$$

A plot of an example diamond trap potential can be found in Fig. 4.8.

4.3.4 Useful relationships

The center of the diamond-shaped potential is very flat, and one may approximate it as zero ($U = 0$), which leads to Eq. (4.32):

$$\mathbf{J_{con}} = -D\left(e^{\tau} - 1\right)\left(\nabla \frac{U}{T}\right) = 0. \tag{4.49}$$

This leads to

$$\mathbf{J}_{\tau} = -D_{eff}\nabla\tau, \tag{4.50}$$

which makes the diffusion equation

$$-D_{eff}\nabla^2\tau + R\tau = G'. \tag{4.51}$$

Converting τ back to density we have

$$-D_{eff}\nabla^2 n = -G\left(n - \bar{n}\right), \tag{4.52}$$

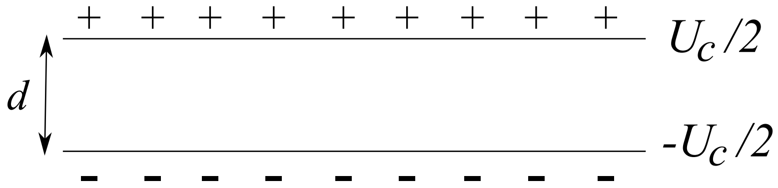

Figure 4.7: Diagram of excitons in “capacitor” formula.

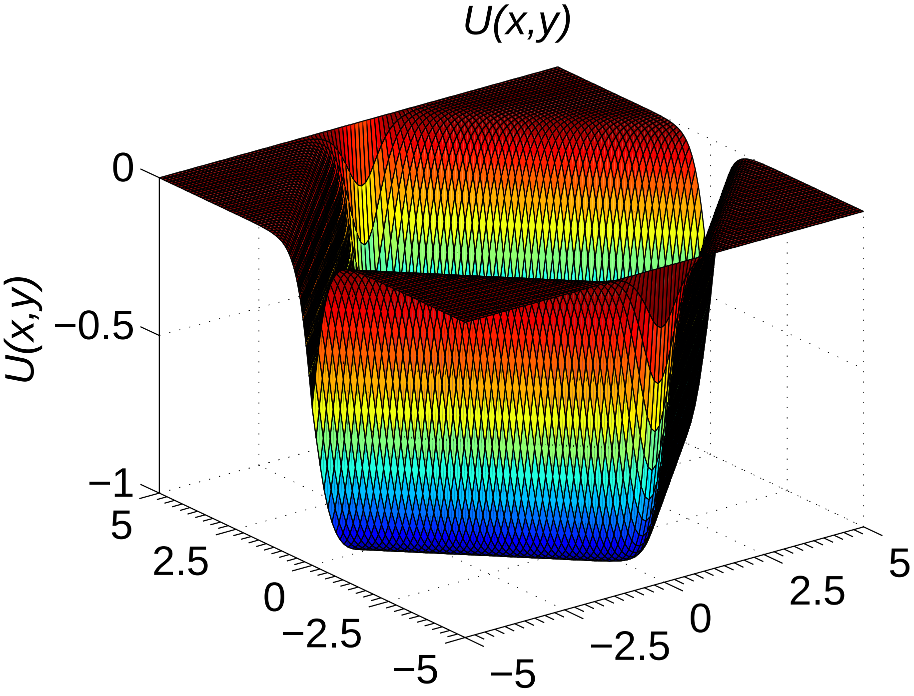

Figure 4.8: Plot of potential $U(x, y)$. Here $V_{trap} = 1$ and $a = 0.5$.

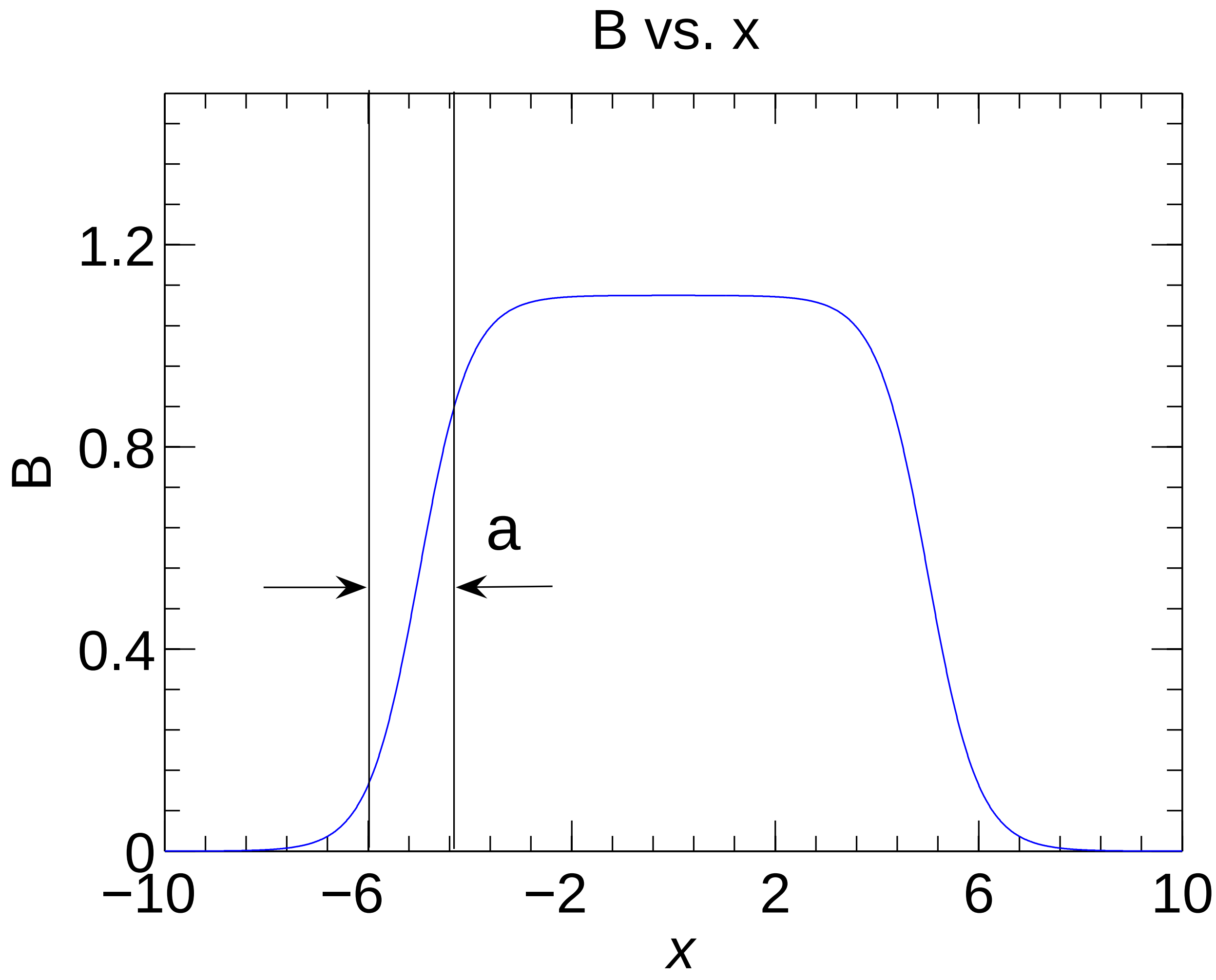

Figure 4.9: Plot of Eq. (4.47). The sharpness of the sides of the box are determined by the constant a. In this figure $a = 1$ and $w = 5$.

remembering that $\bar{n} = G/R$ and

$$D_{eff} = D\left[\Gamma\left(e^{\tau} - 1\right) + 1\right]. \tag{4.53}$$

This is analogous to the Laplace equation, where $n \to \phi$ and

$$\rho \to \frac{1}{4\pi} \frac{R}{D_{eff}} \left(n - \bar{n}\right). \tag{4.54}$$

Chapter 5

Concentration-dependent mobility in organic field-effect transistors

5.1 Introduction

The study of the semiconducting characteristics of organic materials has attracted much research interest. The organic field-effect transistor (FET) is one of the most important applications of organic materials. Studies aim to optimize the performance of organic FETs due to the relative inexpensiveness of these materials. Significant disorder, polaronic, and interaction effects complicate transport mechanisms in organic materials. Therefore, standard model assumptions which are adequate in inorganic devices may be unfeasible. For instance, the canonical model of the FET [64] assumes that the mobility μ is independent of the areal carrier density N in the accumulation layer, while theoretical and experimental studies of organic conductors conclude the opposite [65, 66, 67]. Unfortunately, the nonlinearity of the contact resistance complicates the extraction of mobility from traditional transport measurements. Additional assumptions are usually necessary [68]. Recently, a powerful alternative to transport measurements has appeared: the direct imaging of the charge distribution in the device. Thus, scanning potentiometry studies [69, 70] of an organic FET based on poly-3-hexylthiophene (P3HT) give detailed information about carrier injection and transport, including the interesting regime of current saturation [64] where the charge density in the FET is strongly inhomogeneous. Furthermore, recent experiments show [71] that it is possible to image the accumulation layer of organic FETs using scanning infrared spectroscopy (SIRS). Both methods are able to measure the local carrier density avoiding artifacts due to the contacts, but SIRS also provides the spatially-resolved excitation spectrum.

In this chapter we show that an idealized FET model [64] fails to account for charge density profiles seen in new SIRS data not previously reported. We recount physical arguments that the mobility is density-dependent,

$$\mu = \text{const } \times N^{\beta}, \quad \beta = (E_*/k_B T) - 1 \geq 0, \tag{5.1}$$

and show that this imaging experiment is consistent with this law. Here E_* is the characteristic energy scale of the disorder, which may vary from one device to the next. As a result, the exponent β is not known beforehand and must be determined by its fit to the data. In our case, β ranges between 1 and 4 at $T = 300\,\mathrm{K}$, where all the measurements are taken. This implies $E_* \sim 0.1\,\mathrm{eV}$, which agrees by the order of magnitude with other known experimental measurements of this quantity in P3HT [72]. The power-law behavior (5.1) has also been observed in other organic conductors [65].

5.2 Experiment description

Let us proceed to the description of the SIRS experiment, carried out by the Basov group at UCSD. SIRS was employed to image the injected charges in organic FETs. The structure of the FETs is shown in Fig. 5.1. In these bottom-contacted devices, source and drain Au electrodes were deposited on TiO_2/n-Si substrates followed by the coating of a 4-6 nm thick P3HT film, which served as the electronically active material. The spectroscopic signatures of injected charges in P3HT are the polaron band and the infrared-active vibrational modes, which can be detected by measuring the voltage-induced absorption of the FET [71]. To examine the length scales associated with charge injection, devices were fabricated where source and drain electrodes are tilted with respect to each other. This gives a Λ-shaped pattern [Fig. 5.2] with the separation between electrodes ranging from $10\,\mu$m to 4 mm. By scanning a focused infrared beam 50-100 μm in diameter across the Λ-shaped region and spatially monitoring spectroscopic fingerprints of the injected charges, the charge density profile in the conducting channel of the FET was obtained. In Fig. 5.3, one finds a plot of the deduced change in charge density (compared to ungated FET) as a function of separation x from the source electrode normalized by data at $x = 0$, $N(x)/N(0)$, for three representative devices. The most interesting result of this experiment is that the injected charge density decays with the distance x from the source and drops to zero at $x \sim 800\,\mu$m.

In comparison, the potentiometry experiments of Bürgi et al. [70] used FETs of a similar design, but with a channel of only $\sim 5\,\mu$m wide and a dielectric of only SiO_2. It was found (Fig. 5.4) that the surface potential Φ in the channel can vary in a manner reminiscent of Fig. 5.3. To a good approximation, this potential is linearly related to the local charge density N, and so in both experiments N exhibits a gradual decay of a characteristic concave shape and nearly vanishes at the rightmost point.

However, the reasons for the density inhomogeneity in the two experiments are different. In the larger area FETs it is caused by the current leakage through the dielectric. The charges injected by the source never reach the drain. In Ref. [70], the decay of N is dictated mainly by the large bias voltage (pinch-off effect [64]), and the width of the charge profile is simply the channel width. Nevertheless, we show that both types of experiments can be used to extract the N-dependence of mobility. Here we ignore a possible field-dependence of μ because P3HT is of a rather high mobility, $0.05 < \mu < 0.12$ (in units of $\mathrm{cm}^2/\mathrm{Vs}$) where non-Ohmic effects are not as important as in other, less-conducting organics [66, 67], and also because T was relatively high. (No significant field-dependence was found experimentally at such T [70, 74].)

5.3 Discussion

We start with the analysis of our experiment where a relatively large current leakage j_l through the dielectric [74] was detected. The tunneling resistance per unit area of the dielectric $\rho_l = V/j_l$ was a strong function of V, the voltage difference between the polymer and the gate, at $V < 5\,\mathrm{V}$. At higher V, parameter ρ_l was observed to be approximately constant [74], and we assume this is the case below. In the gradual-channel approximation appropriate for our FETs, the balance of the surface current is

$$\mathbf{j}_s = -\sigma \nabla V \tag{5.2}$$

and leakage current reads

$$\nabla\left(\sigma \nabla V\right) = V/\rho_l. \tag{5.3}$$

For the sheet conductivity σ we adopt the model form $\sigma = \sigma_a + \sigma_r$, where σ_a and σ_r is the sheet conductivities of the accumulation layer and the residual mobile charges, respectively. Initially, let us make the conventional assumptions that (i) $\mu \equiv \sigma_a/eN = \mathrm{const}$, (ii) σ_r is negligible, and (iii) $V = eN/C$, where $C = \mathrm{const}$ is the capacitance per unit area ($C \approx 0.14\,\mu\mathrm{F/cm^2}$ in these FETs). Using Eq. (5.3), we get

$$\nabla\left(N \nabla N\right) = N/(e\mu\rho_l). \tag{5.4}$$

An analogy may be drawn here between Eqs. (5.4) and (4.30). Both equations involve the diffusion of particles, excitons in Chapter 4 and electrons here in Chapter 5. The terms $N/(e\mu\rho_l)$ and Rn are analogous and represent particle loss in the system due to leakage of electrons and recombination of excitons, respectively. Furthermore the interaction terms, the so-called capacitor formulas $V = eN/C$ for electrons and $\Sigma_0 = gn/\nu_1$ [Eq. (4.12)] for excitons, are strikingly similar as well. Note that here g is not too far from the "plate capacitor" estimate, Eqs. (4.11) and (4.45).

Since the characteristic length of charge inhomogeneity is smaller than the lateral extension of the source and drain electrodes in the Λ-shaped region [Fig. 5.2], it is permissible to treat them as infinite metallic half-planes, $x < 0$ and $x > L$, respectively. In this case, all variables depend only on coordinate $x \in (0, L)$.

Suppose first that L is very large (the source and drain are far apart). Then the physically relevant solution of Eq. (5.4) is

$$N(x) = N(0)[1 - (x/x_*)]^2, \quad x < x_* \equiv \sqrt{6\sigma(0)\rho_l}. \tag{5.5}$$

Interestingly, it predicts that there is a well-defined cutoff length x_* for the charge injection. Treating x_* as an adjustable parameter, we plot Eq. (5.5) in Fig. 5.3 (the curves labeled $\beta = 0$). On the other hand, we can estimate x_* from typical values of σ and ρ_l (deduced from the the transport and leakage current measurements [74, 71]), $\sigma \sim 10^{-7}\Omega^{-1}$, and $\rho_l \sim 10^5\,\Omega\,\mathrm{cm}^2$. Equation (5.5) then entails $x_* \sim 2500\,\mu$m. Comparing with Fig. 5.3, we see that the curves do not agree particularly well with this model, neither in their shape nor in the value of x_*. We conclude that a modification of the model is needed.

We reason as follows: At low N, it is natural to assume that the chemical potential ζ presumably resides in the density-of-states tail of disorder-induced traps, but at temperatures of interest such traps are shallow (a few k_BT deep). At temperatures of interest (room temperature and somewhat below), the transport is dominated by activation of carriers to the mobility edge; therefore,

$$\sigma_a \propto \exp(\zeta/k_BT) \tag{5.6}$$

(the mobility edge is taken to be the energy reference point). Because of this exponential relation between the conductivity and ζ, the dependence of ζ on N is amplified in σ_a, producing the sought nonlinear effect.

Next, the chemical potential ζ and the local carrier density N are related by

$$N = \int dEg(E)f(E)\,, \tag{5.7}$$

where $g(E)$ is the density of states and $f(E)$ is the Fermi-Dirac distribution function. Although $g(E)$ is not precisely known, in conducting polymers it is often modeled by Gaussian or exponential forms [66], which are observed experimentally [72]. In either case we obtain

$$N(\zeta) \simeq N_t \exp(\zeta/E_*), \tag{5.8}$$

up to logarithmic factors. Here

$$E_* > k_B T \tag{5.9}$$

is the characteristic energy width of the band tail and N_t is the total number of states per unit area in this tail; hence,

$$\zeta \simeq E_* \ln(N/N_t). \tag{5.10}$$

Substituting this into the formula for σ, we obtain

$$\sigma_a \simeq \sigma_* (N/N_t)^{\beta+1}, \tag{5.11}$$

where

$$\beta + 1 = E_*/k_B T. \tag{5.12}$$

Consequently, the mobility is

$$\mu(N) \equiv \sigma/eN \propto N^{\beta}, \tag{5.13}$$

in agreement with Eq. (5.1). We note that a nearly identical $\mu(N)$ dependence also follows from the hopping transport model [66, 67]. Equation (5.1) was also postulated in Ref. [68]. Substituting $\sigma \propto N^{\beta+1}$ into Eq. (5.4), we obtain

$$N = N(0)\left(1 - \frac{x}{x_*}\right)^{\frac{2}{\beta+1}}, \quad x_* = \frac{\sqrt{2\,(\beta+3)\,\sigma(0)\rho_l}}{\beta+1} \tag{5.14}$$

with Eq. (5.5) being recovered for $\beta = 0$. Three representative curves computed according to Eq. (5.14) are plotted in each panel of Fig. 5.3. We see that for all of the three FETs studied, one can find βs somewhere in the range $1 < \beta < 4$ which give a significantly better fit to experiment than $\beta = 0$, both in the functional form and in the value of x_*. Apparently, Eq. (5.1) is more suitable for modeling the charge injection profile in a “leaky” FET.

For future reference we mention that a refinement of the model including the residual conductivity,

$$\sigma = \sigma_* (N/N_t)^{\beta+1} + \sigma_r\,, \tag{5.15}$$

predicts the injected charge density profile of the form

$$\frac{x}{x_*} = -\sqrt{u+a} + \frac{2\sqrt{a}}{\beta+3}\,\ln\frac{\sqrt{u+a}+\sqrt{a}}{\sqrt{u+a}-\sqrt{a}} + \text{const}, \tag{5.16}$$

$$u \equiv [N(x)/N(0)]^{\beta+1}, \quad a \equiv (\beta+3)\sigma_r/[2\sigma_a(0)]. \tag{5.17}$$

Accordingly,

$$N(x) \propto \exp(-x/\sqrt{\sigma_r \rho_l}) \tag{5.18}$$

at $x > x_*$, i.e., it has exponential decay instead of the abrupt threshold predicted by Eq. (5.14). However, since $\sigma_r/\sigma(0) \sim 10^{-4}$–$10^{-3}$ (the on-off ratio) [74], the pre-exponential factor of this tail is very small, producing apparently no signature in this experiment, see Fig. 5.3.

We move on to the $L < x_*$ case where the charge is injected throughout the channel (as in [70] and in $\mathrm{SiO_2}$ devices studied previously by Li *et al.* [71]). If a finite bias $V_{SD} \equiv V(0) - V(L)$ is applied, Eq. (5.3) still holds but two adjustments are in order. First, the right-hand side of Eq. (5.3) can be set to zero because we can normally neglect the leakage current j_l compared to the source-drain current j_s. Second, when the pinch-off is approached, σ_r may no longer be negligible compared to σ_a, and so a better approximation is [78]

$$\sigma = \sigma_* (N/N_t)^{\beta+1} + \sigma_r. \tag{5.19}$$

The current balance equation (5.3) remains solvable and its integral yields the algebraic equation for $N(x)$:

$$\frac{\sigma_* N_t}{\beta+2}\left(\frac{N}{N_t}\right)^{\beta+2} + \sigma_r N = \frac{C j_s}{e}(x_p - x), \tag{5.20}$$

where x_p is the integration constant. At the pinch-off, $x_p \approx L$. Also, at x not too close to L the first term on the left-hand side dominates, so the charge profile becomes very similar to that of the injection case, Eq. (5.14), except x_* is replaced by L and the power-law exponent $(2/(\beta+2))$ is changed to a smaller number $(1/(\beta+2))$. This explains the visual similarity of the experimental results shown in Figs. 5.3 and 5.4.

Equation (5.20) contains two adjustable parameters. We found that $\sigma_r = 6.2$ and $\beta = 3.0$ give a good fit to the $V_g = -8\,\mathrm{V}$ trace in Fig. 7 of Ref. [70]. Bürgi *et al.* themselves employed another fit, which is equivalent to σ_r and $\beta = 1$ in our notations. They observed, however, that a good fit is achieved only if the data is additionally shifted by $2\,\mathrm{V}$ in order to account for the residual charges. We found this shift *ad hoc*. We think a more reasonable way to model this effect is using parameter σ_r. However, this implies that β has some degree of uncertainty.

5.4 Conclusion

In conclusion, whenever the charge profile in the organic semiconductor is strongly inhomogeneous, as in the charge injection or the pinch-off regimes, the proper modeling should include the density dependence of the carrier mobility. The two experiments discussed are consistent with the power law (5.1), which has a natural physical motivation.

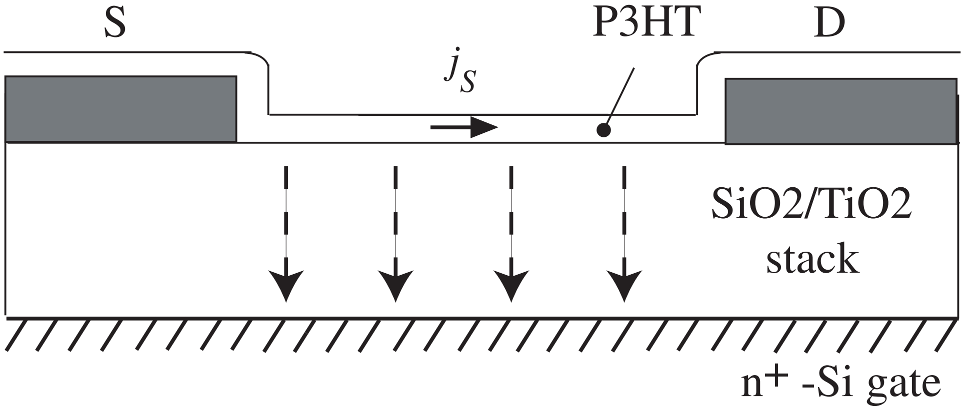

Figure 5.1: FET schematics.

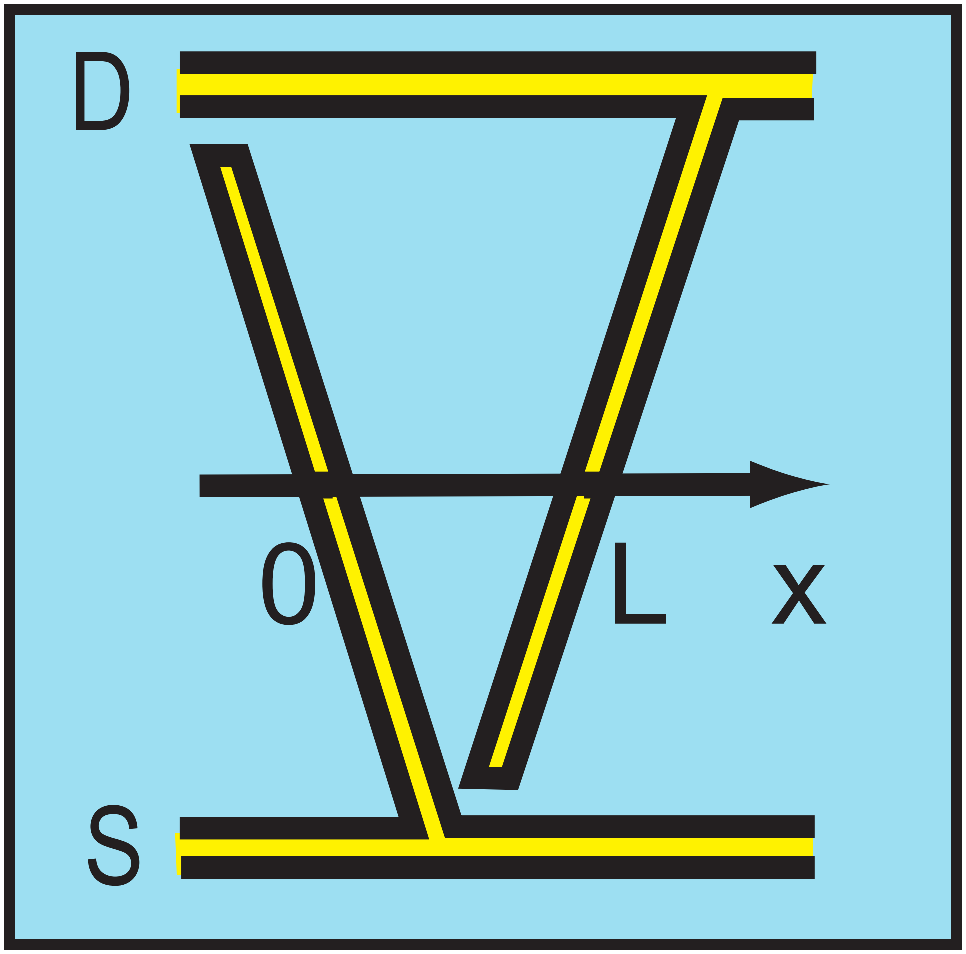

Figure 5.2: A sketch of the V-shaped electrodes between which the IR scans were taken.

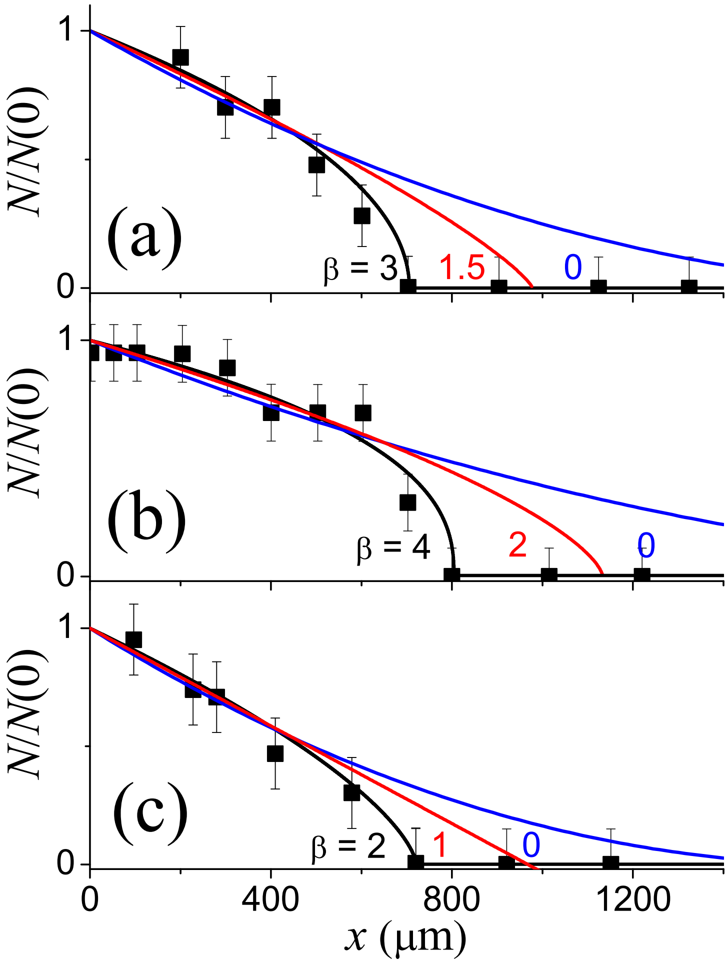

Figure 5.3: Charge density profiles measured by the IR spectromicroscopy in three nominally similar devices. The solid lines are theoretical fits (see text).

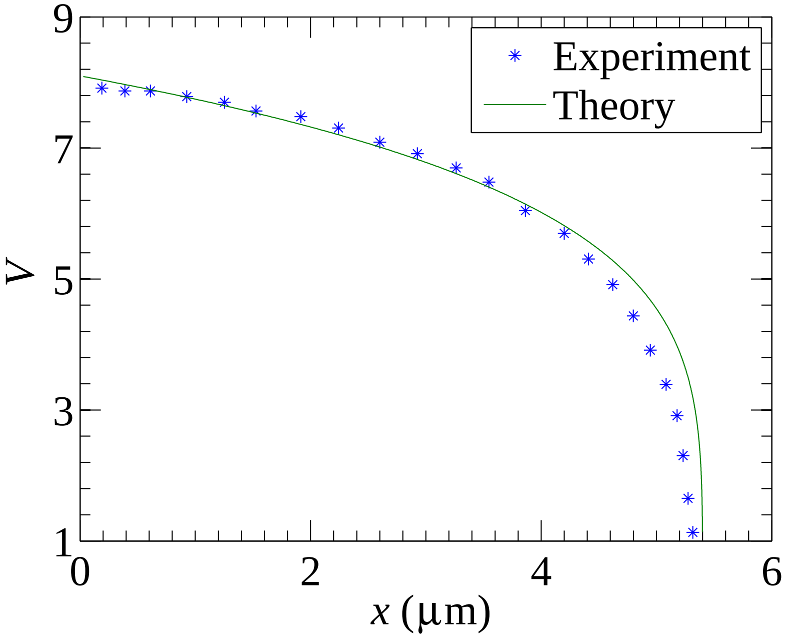

Figure 5.4: Fit of Eq. 5.20 with data from Reference [70].

Appendix A

Rigorous bounds for the biexciton binding energy

A.1 Proof

In this appendix we give a few strict upper bounds on E_B, which enable us to prove the nonexistence of stable biexcitons at sufficiently large d. The basic logic of the proof was outlined in Sec. 3.2A. Here we provide the technical details.

Our starting bound is

$$E_B \leq \max_{R} E_R \,, \tag{A.1}$$

where

$$E_R = \inf \operatorname{spec} H_\infty - \inf \operatorname{spec} H_R \tag{A.2}$$

is the binding energy of the two-electron Hamiltonian $H_R = T_R + U_R$ whose kinetic term is

$$T_R = -(1+\sigma)(\nabla_1^2 + \nabla_2^2) \,, \tag{A.3}$$

and the potential term U_R is given by Eq. (3.15). The Hamiltonian H_R is similar to that of the original problem [Eqs. (3.4)–(3.17)] except the holes are replaced by static charges separated by a given distance R and the electron mass is made equal to the reduced electron-hole mass.

To derive the inequality (A.1) we take advantage of the well-known theorem that the ground-state energy as a concave function in the strength of an arbitrary linear perturbation. (This theorem follows from the variational principle.) For our purposes we choose the perturbation in the form

$$\Delta T_j = \nabla_j^2 - \left(\frac{d}{d\mathbf{R}_j}\right)^2 . \tag{A.4}$$

We add it to the kinetic energy terms with the coefficient $-\sigma \leq \tau \leq 1$, yielding $T_j \to T_j + \tau \Delta T_j$. Hamiltonians H and H_R are obtained by setting $\tau = 0$ and $\tau = -\sigma$, respectively.

The perturbation leaves the reduced electron-hole mass invariant. Therefore, it does not effect the ground-state energy E_X of a single exciton. The energy $E_{\text{XX}}(\tau)$ does vary with τ and the aforementioned concavity property dictates

$$E_{\text{XX}}(\tau) \geq \frac{1-\tau}{1+\sigma} E_{\text{XX}}(-\sigma) + \frac{\tau+\sigma}{1+\sigma} E_{\text{XX}}(1) . \tag{A.5}$$

Since $E_{\text{XX}}(-\sigma) = E_{\text{XX}}(1)$ by electron-hole symmetry, the right-hand side is equal to $E_{\text{XX}}(-\sigma)$ for all τ. Consequently, $\tau = -\sigma$ gives the largest binding energy and we arrive at the inequality (A.1).

If the kinetic energy T_R is discarded, E_R becomes equal to $-V_{\text{cl}}(R, d) < 0$. We want to ascertain that quantum corrections do not change the sign of E_R.

The quantum corrections appear in both E_{X} and E_{XX}. The former are well understood. [38] The internal dynamics of the exciton in the large-d case is analogous to that of a two-dimensional harmonic oscillator with the amplitude of the zero-point motion given by

$$\langle |\mathbf{r}_1 - \mathbf{R}_1|^2 \rangle = l^2 , \quad l = d^{3/4}(1+\sigma)^{1/4} \ll d . \tag{A.6}$$

The corresponding energy correction is

$$E_X + \frac{2}{d} = \frac{2\sqrt{1+\sigma}}{d^{3/2}} - \mathcal{O}\left(\frac{1}{d^2}\right) . \tag{A.7}$$

This result immediately restricts the range of R where the stable biexciton may in principle exist. By positivity of the kinetic energy, $E_R < 2E_X - U_{\text{min}}(R, d)$, where U_{min} is defined in Sec. 3.2A. Therefore, $E_R > 0$ may occur only at R that satisfy

$$V_{\text{cl}}(R) > 2E_X + \frac{4}{d} . \tag{A.8}$$

In view of Eqs. (3.16) and (A.7), R must necessarily be much larger than d.

Choose an arbitrary d_1 such that $d \ll d_1 \ll R$. By definition of $U_{\min}$,

$$U_R \geq U_{\min}(R, d_1) + V_Y(\mathbf{r}_1) + V_Y(\mathbf{r}_2)\,, \tag{A.9}$$

$$V_Y(\mathbf{r}) = \sum_{\mathbf{t}=\pm\mathbf{R}/2} [v(\mathbf{r}-\mathbf{t}, d_1) - v(\mathbf{r}-\mathbf{t}, d)]\,. \tag{A.10}$$

Accordingly, $E_R < 2E_{\mathrm{X}} - U_{\min}(R, d_1) - 2E_Y$, where E_Y is the ground-state energy of a *single* electron subject to the potential $V_Y(\mathbf{r})$ of four out-of-plane charges. This potential has the shape of two symmetric wells separated by the distance R. The amplitude of the zero-point motion in each well is again $l \ll R$. Therefore, the energy shift due to tunneling between the wells is exponentially small. (A rigorous upper bound can be given. [57]) Furthermore, potential V_Y near the bottom of each well coincides with that of a single exciton up to a constant

$$\Delta V_Y = V_Y\left(\frac{\mathbf{R}}{2}\right) - \frac{2}{d} = \frac{2}{d_1} + \frac{d_1^2 - d^2}{R^3}\,. \tag{A.11}$$

Hence, $E_Y = E_{\mathrm{X}} + \Delta V_Y$ and

$$E_R \leq -\frac{2d^2}{R^3} - \left[V_{\mathrm{cl}}(R, d_1) - \frac{2d_1^2}{R^3}\right]\,. \tag{A.12}$$

In these formulas we have dropped subleading terms $o(l^2/d_1^2)$, $o(d_1^4/R^5)$, *etc.* With the same accuracy the bracket in Eq. (A.12) vanishes [cf. Eq. (3.16)], so that we arrive at the result $E_R \simeq -V_{\mathrm{cl}}(R, d)$. This simply means that at large d all quantum corrections to E_R are parametrically smaller than the direct dipolar repulsion of the two excitons. Therefore, $E_R \leq 0$ at all R, so that $E_B \leq 0$, and the proof is complete.

Appendix B

Radial wavefunction for small mass ratios

In this appendix we show how the suitable solution of Eq. (3.35) can be constructed within the quasiclassical approximation. The necessary connection formulas are derived by asymptotic matching with two exact solutions at small and large R.

It is convenient to define the rescaled wavefunction $\psi(R) = \chi(R)\sqrt{R}$. From Eq. (3.35) we find that ψ satisfies the equation

$$\psi'' - \left(\varkappa^2 + \mu V(R) - \frac{1}{4R^2}\right)\psi = 0\,. \tag{B.1}$$

This equation has two linearly independent quasiclassical solutions

$$\psi_\pm(R) = \frac{1}{\sqrt{Q(R)}}\exp\big(\pm[S(R) - S(b)]\big)\,, \tag{B.2}$$

where Q and S are given by

$$Q(R) = \sqrt{\varkappa^2 + \mu V(R)}\,, \quad S(R) = \int\limits_{R_+}^{R} d\rho Q(\rho)\,. \tag{B.3}$$

The subtraction of the R-independent term $S(b)$ in the exponentials amounts to multiplying $\psi_\pm$ by unimportant constants. This is done purely for the sake of convenience. The reason for omitting the $1/4R^2$ term in the formula for Q is more subtle. It is explained in detail in Ref. [58].

In the following we assume that $\varkappa \ll 1/b$, in which case there exists a broad interval $d \ll R \ll b$ where potential $V(R)$ is dominated by the dipolar repulsion (3.1). In this interval, $\mu V(R) \simeq b/4R^3 \gg \varkappa^2$; therefore,

$$\psi_\pm(R) \simeq \left(\frac{4}{b}R^3\right)^{1/4} \exp\left[\pm\left(1-\sqrt{\frac{b}{R}}\right)\right]. \tag{B.4}$$

Using the asymptotic expansion formulas [43] for I_0 and K_0, it is easy to see that the following linear combination

$$\psi(R) \simeq \frac{e}{2\sqrt{\pi}}\psi_-(R) - \frac{2\sqrt{\pi}}{e}c_2\psi_+(R) \tag{B.5}$$

of the quasiclassical wavefunctions (B.4) smoothly matches with the exact solution (3.37) at $d \ll R \ll b$. This is our first connection formula. It is crucial for this derivation because in the intermediate range of distances $b \ll R \ll \varkappa$ the quasiclassical approximation breaks down. (It is invalidated by the sharp decrease of V with R.) In that region $\chi(R) = \psi/\sqrt{R}$ exhibits a slow logarithmic falloff (3.24) instead of the algebraic decay suggested by Eq. (B.4). As explained in Sec. 3.2, the nonanalytical behavior (3.11) of the binding energy is precisely due to this logarithmic falloff.

To finish the calculation we need a second connection formula between χ given by Eq. (B.5) and the same function near the classical turning point R_+. To find it we take advantage of the exact solution for the harmonic oscillator potential (3.38) in terms of the parabolic cylinder function, [43]

$$\psi \propto D_{\varepsilon-1/2}(-\sqrt{2}\,x), \quad x = \frac{R-R_0}{l}. \tag{B.6}$$

Here $R_0 = (R_+ + R_-)/2$ is the point where the potential $V(R)$ has the minimum, $l = (2\,/\,\mu V'')^{1/4}$ is the amplitude of zero-point motion about this minimum, and ε, given by

$$\varepsilon = \frac{1}{2}l^2\left(\mu|V(R_0)| - \varkappa^2\right), \tag{B.7}$$

is the corresponding energy in units of the oscillator frequency $\omega = 2\,/\,\mu l^2$. For the ground state we expect

$$\delta \equiv \varepsilon - \frac{1}{2} \ll 1. \tag{B.8}$$

The negative sign in the argument of $D_{\varepsilon-1/2}$ in Eq. (B.6) is chosen to obtain an exponentially decaying wave at large negative x, i.e., from the left turning point R_- and towards the origin. At large positive x, that is, at $R - R_+ \gg l$, both decaying and growing exponentials are present. At such x the wavefunction can be cast into the quasiclassical form

$$\psi \simeq \sum_{\nu=\pm} \frac{c_\nu}{\sqrt{x}} \exp\left(\nu \int\limits_{\sqrt{2\varepsilon}}^{x} d\xi \sqrt{\xi^2 - 2\varepsilon} \right) , \tag{B.9}$$

which is equivalent to

$$\sqrt{l}\;\psi(R) \simeq c_- e^{-S(b)} \psi_-(R) + c_+ e^{S(b)} \psi_+(R) \, , \tag{B.10}$$

see Eqs. (3.38), (B.2), and (B.6). This is our second connection formula except we still have to specify the preexponential factors c_+ and c_-. In fact, only their ratio is important. With the help of the asymptotical expansion [43] for D_δ, one finds it to be [59]

$$\frac{c_+}{c_-} \simeq -2\sqrt{\pi e}\,\delta \, . \tag{B.11}$$

Comparing Eqs. (B.5) and (B.10), we obtain

$$\delta \simeq -\frac{1}{2\sqrt{\pi e}} \frac{c_+}{c_-} \simeq 2\sqrt{\frac{\pi}{e}}\, c_2 e^{-2S(b)-2} . \tag{B.12}$$

For $\varkappa$ at which the above calculation is valid we have $S(b) \simeq S_0 - 1$, where $S_0 = S(R = \infty, \varkappa = 0)$. Thus, we arrive at

$$\varkappa^2 \simeq \mu |V(R_0)| - \frac{1}{l^2} - 4\sqrt{\frac{\pi}{e}} \frac{c_2}{l^2} e^{-2S_0} \, , \tag{B.13}$$

which leads to Eqs. (3.39)–(3.41) of Sec. 3.2.

Finally, a minor technical comment is in order. Since we have used the quasiclassical approximation, all coefficients in Eq. (B.13) have a relative accuracy $\mathcal{O}\left(e^{-S(b)}\right)$. In particular, we expect that in place of $V(R_0)$ we have a slightly more negative value, so that the ground-state energy E_B never exceeds the oscillator ground-state energy $V(R_0) + 1/(2\mu l^2)$, as required by physical considerations.

Appendix C

Gaussian integrals and the Hamiltonian matrix elements

Since correlated Gaussian functions are the basis functions for the stochastic variational method, the integration of a Gaussian comes up often. What follows is the analytic solution for the matrix elements using these basis states.

Assume the matrix elements are being computed for two basis sets of the form

$$G_n = \exp\left(-\frac{1}{2}\mathbf{x}^\dagger \mathbf{B}_n \mathbf{x}\right). \tag{C.1}$$

Start with the overlap integral

$$\langle G_1|G_2\rangle = \int \mathcal{D}\mathbf{x} \exp\left[-\frac{\mathbf{x}^\dagger \mathbf{B}_+ \mathbf{x}}{2} + \mathbf{b}_+{}^\dagger \mathbf{x}\right] = \left[\frac{(2\pi)^N}{\det(\mathbf{B}_+)}\right]^{D/2} \exp\left[\frac{1}{2}\mathbf{b}_+{}^\dagger \mathbf{B}_+{}^{-1}\mathbf{b}_+\right]. \tag{C.2}$$

Here $\mathbf{B}_+ = \mathbf{B}_1 + \mathbf{B}_2$ and $\mathbf{b}_+ = \mathbf{b}_1 + \mathbf{b}_2$ are the sums of two successive basis coefficients.

Next, one moves to the kinetic energy matrix integral

$$T = \left\langle G_1 \right| - \Lambda \nabla^2 \left| G_2 \right\rangle \,, \tag{C.3}$$

where $\Lambda = \hbar^2/2m$ is the usual kinetic energy coefficient.

This can be rewritten

$$\langle \nabla G_1 | \Lambda | \nabla G_2 \rangle \,, \tag{C.4}$$

which can be expressed as

$$\langle\nabla G_1|\Lambda|\nabla G_2\rangle = \int \mathcal{D}\mathbf{x}(\mathbf{B}_1+\mathbf{b}_1)\Lambda(\mathbf{B}_2+\mathbf{b}_2)\exp[-\frac{\mathbf{x}^\dagger\mathbf{B}_+\mathbf{x}}{2}+\mathbf{b}_+{}^\dagger\mathbf{x}]. \tag{C.5}$$

Realizing that

$$-\frac{\mathbf{x}^\dagger\mathbf{B}_+\mathbf{x}}{2}+\mathbf{b}_+{}^\dagger\mathbf{x} = -\frac{1}{2}\left[\mathbf{x}-\mathbf{B}_+^{-1}\mathbf{b}_+\right]\mathbf{B}_+\left[\mathbf{x}-\mathbf{B}_+^{-1}\mathbf{b}_+\right], \tag{C.6}$$

leads to a change of variables as such

$$\mathbf{y} = (\mathbf{x}-\mathbf{B}_+^{-1}\mathbf{b}_+), \tag{C.7}$$

leaving a final form

$$\int \mathcal{D}\mathbf{x}\left[-\mathbf{B}_1(\mathbf{y}+\mathbf{B}_+^{-1}\mathbf{b}_+)+\mathbf{b}_1\right]^\dagger\Lambda\left[-\mathbf{B}_2(\mathbf{y}+\mathbf{B}_+^{-1}\mathbf{b}_+)+\mathbf{b}_2\right]\exp[-\frac{\mathbf{y}^\dagger\mathbf{B}_+\mathbf{y}}{2}], \tag{C.8}$$

and leaving the terms

$$\begin{aligned}\int \mathcal{D}\mathbf{x}[&\left(-\mathbf{B}_1\mathbf{B}_+^{-1}\mathbf{b}_++\mathbf{b}_1\right)^\dagger\Lambda\left(-\mathbf{B}_2\mathbf{B}_+^{-1}\mathbf{b}_++\mathbf{b}_2\right)+[\mathbf{B}_1\mathbf{y}]^\dagger\Lambda\mathbf{B}_2\mathbf{y}\\ &-[\mathbf{B}_1\mathbf{y}]^\dagger\left(-\mathbf{B}_2\mathbf{B}_+^{-1}\mathbf{b}_++\mathbf{b}_2\right)-\left(-\mathbf{B}_1\mathbf{B}_+^{-1}\mathbf{b}_++\mathbf{b}_1\right)^\dagger\mathbf{B}_2\mathbf{y}]\times\exp[-\frac{\mathbf{y}^\dagger\mathbf{B}_+\mathbf{y}}{2}],\end{aligned} \tag{C.9}$$

with a solution

$$\begin{aligned}\langle G_1|G_2\rangle&\left[\left[-\mathbf{B}_1(\mathbf{B}_+^{-1}\mathbf{b}_+)+\mathbf{b}_1\right]^\dagger\Lambda\left[-\mathbf{B}_2(\mathbf{B}_+^{-1}\mathbf{b}_+)+\mathbf{b}_2\right]\right]\\ &+D\mathrm{Tr}\left[(\mathbf{B}_2+\mathbf{B}_1)^{-1}(\mathbf{B}_1\Lambda\mathbf{B}_2)\right],\end{aligned} \tag{C.10}$$

again where D is the spatial dimension for the system.

Finally, one calculates the potential term. Here to make the integration easier the potential is expressed

$$V(\mathbf{r}_i-\mathbf{r}_j) = \int d\mathbf{r}V(\mathbf{r})\,\delta(\mathbf{r}_i-\mathbf{r}_j-\mathbf{r}). \tag{C.11}$$

Therefore, the potential matrix element will look like

$$\langle G_1|V_{ij}|G_2\rangle = \int d\mathbf{r}V(\mathbf{r})\,\langle G_1|\delta(\mathbf{r}_i-\mathbf{r}_j-\mathbf{r})|G_2\rangle\,. \tag{C.12}$$

One then sets to solve the matrix element $\langle G_1|\delta(\mathbf{r}_i - \mathbf{r}_j - \mathbf{r})|G_2\rangle$, as follows.

Start with

$$\langle G_1|\delta\left(\mathbf{r}_i - \mathbf{r}_j - \mathbf{r}\right)|G_2\rangle = \int \mathcal{D}\mathbf{x}\,\delta(\mathbf{r}_i - \mathbf{r}_j - \mathbf{r})\exp\,[-\frac{\mathbf{x}^\dagger\mathbf{B}_+\mathbf{x}}{2} + \mathbf{b}_+{}^\dagger\mathbf{x}]. \tag{C.13}$$

Using the relationship between spatial and Jacobi coordinates

$$\mathbf{x}_i = \sum_{j=1}^{N}\mathbf{U}_{ij}\mathbf{r}_j\,, \tag{C.14}$$

we have

$$\langle G_1|\delta(\mathbf{r}_i - \mathbf{r}_j - \mathbf{r})|G_2\rangle = \int \mathcal{D}\mathbf{x}\,\delta(\mathbf{r} - \mathbf{C}^\dagger\mathbf{x})\exp\,[-\frac{\mathbf{x}^\dagger\mathbf{B}_+\mathbf{x}}{2} + \mathbf{b}_+{}^\dagger\mathbf{x}]. \tag{C.15}$$

where

$$\mathbf{r}_i - \mathbf{r}_j = \sum_{i=1}^{N-1}\mathbf{C}_{ijk}\mathbf{x}_k\,, \tag{C.16}$$

implying

$$\mathbf{C}_{ijk} = \mathbf{U}_i k^{-1} - \mathbf{U}_j k^{-1}\,, \tag{C.17}$$

The Dirac delta function may be expressed

$$\delta(\mathbf{r} - \mathbf{C}^\dagger\mathbf{x}) = \int \frac{d^2\lambda}{(2\pi)^D}\exp\left[i\lambda(\mathbf{r} - \mathbf{C}^\dagger\mathbf{x})\right]. \tag{C.18}$$

With this Eq. (C.15) becomes

$$\int \frac{d^2\lambda}{(2\pi)^D}\exp\,[i\lambda\mathbf{r}]\int \mathcal{D}\mathbf{x}\exp\,[-\frac{\mathbf{x}^\dagger\mathbf{B}_+\mathbf{x}}{2} + \mathbf{Q}^\dagger\mathbf{x}]\,, \tag{C.19}$$

where $\mathbf{Q} = \mathbf{b}_+ - i\lambda\mathbf{C}$. So now with Eq. (C.2) $\mathcal{D}\mathbf{x}$ can be computed, leading to

$$\int \frac{d^2\lambda}{(2\pi)^D}\exp\,[i\lambda\mathbf{r}]\left[\frac{(2\pi)^N}{\det(\mathbf{B}_+)}\right]^{D/2}\exp\,[\frac{1}{2}\mathbf{Q}^\dagger\mathbf{B}_+{}^{-1}\mathbf{Q}]\,, \tag{C.20}$$

expanding the argument of the exponential

$$\frac{1}{2}\mathbf{Q}^\dagger\mathbf{B}_+{}^{-1}\mathbf{Q} = \frac{1}{2}\mathbf{b}_+^\dagger\mathbf{B}_+^{-1}\mathbf{b}_+ - \frac{\lambda^2}{2}\mathbf{C}^\dagger\mathbf{B}_+^{-1}\mathbf{C} - i\lambda\mathbf{b}_+^\dagger\mathbf{B}_+^{-1}\mathbf{C}. \tag{C.21}$$

We can rewrite our expression as

$$\langle G_1|G_2\rangle\int \frac{d^2\lambda}{(2\pi)^D}\exp\left[-\frac{\lambda^2}{2}\beta + i\lambda\left(\mathbf{r} - \boldsymbol{\gamma}\right)\right], \tag{C.22}$$

where $\beta = \mathbf{C}^{\dagger}\mathbf{B}_{+}^{-1}\mathbf{C}$ and $\boldsymbol{\gamma} = \mathbf{b}_{+}^{\dagger}\mathbf{B}_{+}^{-1}\mathbf{C}$. Again, this leads to a Gaussian integral which gives

$$\langle G_1|\delta\left(\mathbf{r}_i - \mathbf{r}_j - \mathbf{r}\right)|G_2\rangle = \frac{\langle G_1|G_2\rangle}{2\pi\beta}\exp\left[-\frac{(\mathbf{r}-\boldsymbol{\gamma})^2}{2\beta}\right]. \tag{C.23}$$

With Eq. (C.12), we have

$$\langle G_1|V_{ij}|G_2\rangle = \frac{\langle G_1|G_2\rangle}{2\pi\beta}\int d\mathbf{r}V(\mathbf{r})\exp\left[-\frac{(\mathbf{r}-\boldsymbol{\gamma})^2}{2\beta}\right], \tag{C.24}$$

which then depends on the type of potential.

Appendix D

Fermi gas

Section 2.2 references the Fermi gas, the most basic model of charge carriers in a solid. In this model the electrons are considered to be free with no interaction potential, including any interactions from lattice ions or other electrons. To better understand the system dealt with in Chapter 3 and 4, it is useful to work through some of the conclusions from Section 2.2. In this appendix, a brief explanation of the Fermi gas is presented, including a discussion of the density of states, for both a two-dimensional and a three-dimensional system. An excellent account of this topic can be found in the textbook "Solid State Physics" by Ashcroft and Mermin [9].

With no potential energy term V, the Schrodinger equation for these electrons becomes

$$\frac{-\hbar^2}{2m}\nabla^2\Psi(\mathbf{r}) = E\Psi(\mathbf{r}). \tag{D.1}$$

The boundary conditions on the electrons are periodic with the lattice. If the lattice is assumed to be isotropic, Born-von Karmon periodic boundary conditions apply, like so:

$$\Psi(\mathbf{r}+\mathbf{L}) = \Psi(\mathbf{r}), \tag{D.2}$$

where $\mathbf{L}$ is the lattice vector. Therefore the solution to Eq. (D.1) is

$$\Psi(\mathbf{r}) = \frac{1}{\sqrt{V}}\; e^{i\mathbf{k}\cdot\mathbf{r}}, \tag{D.3}$$

where V is the volume L^3, $\mathbf{k}^2 = k_x^2 + k_y^2 + k_z^2$ is the momentum vector for the electrons, and

$$k_x = \frac{2\pi n_x}{L} \quad k_y = \frac{2\pi n_y}{L} \quad k_z = \frac{2\pi n_z}{L}. \tag{D.4}$$

As such, the momentum is quantized and this leads to an infinite number of quantized states with quantum numbers n_x, n_y, and n_z [5]. The energy for one of these electronic states is

$$E = \frac{\hbar^2 \mathbf{k}^2}{2m^2}. \tag{D.5}$$

To determine the macroscopic properties of a system, we must determine how the total number of electrons fill these particular momentum states. As fermions, the electrons fill these levels according to Fermi-Dirac statistics, each state can account for two spins. A good way to visualize this is through a quantity called the density of states. The density of states represents the number of momentum states that exist in a certain energy range. This quantity proves useful in calculating macroscopic characteristics for the solids in question. To do this, we work in the momentum space, or k-space: the space that spans the system's possible momentum [9].

From Eq. (D.4), the volume of one state in k-space can be seen as

$$V_{state} = \frac{2\pi}{L} \times \frac{2\pi}{L} \times \frac{2\pi}{L} = \frac{8\pi^3}{L^3}, \tag{D.6}$$

while the volume of all the filled states in k-space can be thought of as approximately a sphere with radius k_F:

$$V_{total} = \frac{4\pi k_F^3}{3}. \tag{D.7}$$

We call k_F the Fermi momentum. It is defined as the maximum occupied momentum state of a Fermi gas. Dividing these two volumes gives the total number of occupied states:

$$N = \frac{V k_F^3}{3\pi^2}. \tag{D.8}$$

Note that we multiply by two due to the Pauli spin exclusion principle. Now, the definition of the density of states is

$$\mathcal{D}(E) = \frac{dN}{dE}, \tag{D.9}$$

which gives the energy dependence of the number of states. It is then easiest to express N in terms of energy using Eq. (D.5):

$$N = \frac{V}{3\pi^2}\left(\frac{2mE}{\hbar^2}\right)^{3/2}, \tag{D.10}$$

leading to a density of states of

$$\mathcal{D}(E) = \frac{V}{2\pi^2}\left(\frac{2m}{\hbar^2}\right)^{3/2} E^{1/2}, \tag{D.11}$$

which gives the energy dependence of the number of states. It is then easiest to express N in terms of energy using Eq. (D.5):

$$N = \frac{V}{3\pi^2}\left(\frac{2mE}{\hbar^2}\right)^{3/2}, \tag{D.12}$$

leading to a density of states of

$$\mathcal{D}(E) = \frac{V}{2\pi^2}\left(\frac{2m}{\hbar^2}\right)^{3/2} E^{1/2}. \tag{D.13}$$

Our work deals primarily with a two-dimensional excitonic system. We will find the density of states in two dimensions is very different. The density of states is a crucial component in calculating macroscopic physical properties of the system. This leads to very different physics for a two-dimensional versus a three-dimensional system.

Here, the method to find the density of states is similar. In two dimensions, the "volume" of a state in k-space is

$$V_{state} = \left(\frac{2\pi}{L}\right)^2, \tag{D.14}$$

and the "volume" of a filled k-space is

$$V_{total} = \pi k_F^2, \tag{D.15}$$

leading to a total number of occupied states in two dimensions of

$$N = \frac{L^2 k_F^2}{2\pi^2}. \tag{D.16}$$

Again, we multiply by two to account for spin. Converting to a function of energy E, we have

$$N = \frac{L^2 m E}{\pi \hbar^2}, \tag{D.17}$$

leading to a density of states of

$$\mathcal{D}(E) = \frac{L^2 m}{\pi \hbar^2}. \tag{D.18}$$

Appendix E

Heitler-London

The original version of the stochastic variational method uses axially symmetric trial states which unfortunately are not suitable for large σ or loosely bound systems as we have for $d \sim d_c$. The Heitler-London approximation is one simple albeit less precise alternative method which can be used in this case. With the Heitler-London approximation, one works with the solutions to the single exciton Hamiltonian:

$$H_E = -\frac{\hbar^2}{2m_e}\nabla^2 - \frac{\hbar^2}{2m_h}\nabla^2 + \frac{e^2}{\sqrt{(\mathbf{r}_e^2 - \mathbf{r}_h^2) + d^2}} = E. \tag{E.1}$$

The above stochastic variational method was used to find approximate wave functions for the single exciton Hamiltonian which we will call $\Phi(\mathbf{r})$. These wave functions are then used to form the Heitler-London approximate bi-exciton two-body wave function:

$$\Psi(\mathbf{r}_1, \mathbf{r}_2)^{T,S} = C\left[\Phi(\mathbf{r}_1)\Phi(\mathbf{r}_2 - \mathbf{R}) \pm \Phi(\mathbf{r}_1 - \mathbf{R})\Phi(\mathbf{r}_2)\right], \tag{E.2}$$

where R is the separation vector between excitons. $\mathbf{r}_1$ and $\mathbf{r}_2$ are the separation vectors between the first electron and hole and the second electron and hole, respectively. Here the $+$ sign refers to the triplet and the $-$ sign to the singlet, and the normalization constant is

$$C = 2(1 - S^2), \tag{E.3}$$

where S is defined as

$$S = \int d\mathbf{r}\Phi(\mathbf{r})\Phi(\mathbf{r} - R). \tag{E.4}$$

The ground state energy is then found from the expectation value of the energy:

$$E_{GS} = \left\langle \Psi(\mathbf{r}_1, \mathbf{r}_2)^{T,S} | H_{BE} | \Psi(\mathbf{r}_1, \mathbf{r}_2)^{T,S} \right\rangle . \tag{E.5}$$

The ground state energy can then be calculated as a function of R for various values of σ and d.

Bibliography

[1] T. Pradeep, *Nano* (McGraw-Hill Professional, 2008).

[2] L. V. Butov, J. Phys.: Condens. Matter **19**, 295202 (2007).

[3] J. Harrison, *Quantum Wells, Wires and Dots* (Wiley, England, 2005).

[4] M. Remeika, J. C. Graves, A. T. Hammack, A. D. Meyertholen, M. M. Fogler, L. V. Butov, M. Hanson, and A. C. Gossard, Phys. Rev. Lett. **52**, 1885 (2009).

[5] S. Datta, *Electronic Transport in Mesoscopic Systems* (Cambridge University Press, 1995).

[6] S.A. Moskalako and D. W. Snoke, *Bose Einstein Condensation of Excitons and Biexcitons* (Cambridge University Press, 2000).

[7] A. A. High, E. E. Novitskaya, L. V. Butov, M. Hanson, and A. C. Gossard, Science **321**, 229 (2008).

[8] E. Hanamura and H. Haug, Phys. Rep. **33**, 209 (1977).

[9] N. W. Ashcroft and N. D. Mermin, *Solid State Physics* (Brooks Cole, 1976).

[10] V. N. Popov, *Functional Integrals in Quantum Field Theory and Statistical Mechanics* (D. Reidal Publications, 1983).

[11] J. M. Kosterlitz, D. J. Thouless, Phys. C: Solid State Phys. **6**, 1181 (1973).

[12] D. S. Fisher, P. C. Hohenberg, Phys. Rev. B **37**, 4936 (1988).

[13] N. Prokof' ev, O. Ruebenacker, and B. Svistunov, Phys. Rev. Lett. **87**, 270402 (2001).

[14] D. Yoshioka and A. H. MacDonald, J. Phys. Soc. Japan **59**, 4211 (1990).

[15] X. Zhu, P. B. Littlewood, M. Hybertsen, and T. Rice, Phys. Rev. Lett. **74**, 1633 (1995).

[16] L. V. Butov, A. C. Gossard, and D. S. Chemla, Nature (London) **418**, 751 (2002).

[17] L. V. Butov, L. S. Levitov, A. V. Mintsev, B. D. Simons, A. C. Gossard, and D. S. Chemla, Phys. Rev. Lett. **92**, 117404 (2004).

[18] S. Yang, A. T. Hammack, M. M. Fogler, L. V. Butov, and A. C. Gossard, Phys. Rev. Lett. **97**, 187402 (2006); M. M. Fogler, Sen Yang, A. T. Hammack, L. V. Butov, and A. C. Gossard, Phys. Rev. B **78**, 035411 (2008).

[19] K. Varga and Y. Suzuki, Phys. Rev. C **52**, 1885 (1995).

[20] K. Varga and Y. Suzuki, Comp. Phys. Commun. **106**, 157 (1997). The companion computer program is available at the CPC Program Library, online at `http://www.cpc.cs.qub.ac.uk`.

[21] M. Hagn, A. Zrenner, G. Böhm, G. Weimann, Appl. Phys. Lett. **67**, 232 (1995).

[22] A. V. Larionov, V. B. Timofeev, J. Hvam, and K. Soerensen, Zh. Eksp. Teor. Fiz. **117**, 1255 (2000) [JETP **90**, 1093 (2000)].

[23] Z. Vörös, R. Balili, D. W. Snoke, L. Pfeiffer, K. West, Phys. Rev. Lett. **94**, 226401 (2005).

[24] A. L. Ivanov, L. E. Smallwood, A. T. Hammack, Sen Yang, L. V. Butov, and A. C. Gossard, Europhys. Lett. **73**, 920 (2006).

[25] R. C. Miller, D. A. Kleinman, A. C. Gossard, and O. Munteanu, Phys. Rev. B **25**, 6545 (1982).

[26] R. T. Phillips, D. J. Lovering, G. J. Denton, and G. W. Smith, Phys. Rev. B **45**, 4308 (1992).

[27] S. Bar-Ad and I. Bar-Joseph, Phys. Rev. Lett. **68**, 349 (1992).

[28] D. Birkedal, J. Singh, V. G. Lyssenko, J. Erland, and J. M. Hvam, Phys. Rev. Lett. **76**, 672 (1996).

[29] S. Adachi, T. Miyashita, S. Takeyama, Y. Takagi, A. Tackeuchi, and M. Nakayama, Phys. Rev. B **55**, 1654 (1997).

[30] J. C. Kim and J. P. Wolfe, Phys. Rev. B **57**, 9861 (1998).

[31] W. Langbein and J. M. Hvam, Phys. Stat. Sol. A **190**, 167 (2002).

[32] M. Maute, S. Wachter, H. Kalt, K. Ohkawa, and D. Hommel Phys. Rev. B **67**, 165323 (2003).

[33] M. Y. J. Tan, N. D. Drummond, and R. J. Needs, Phys. Rev. B **71**, 033303 (2005).

[34] L. V. Butov and A. I. Filin, Phys. Rev. B **58**, 1980 (1998).

[35] D. Bressanini, M. Mella, and G. Morosi, Phys. Rev. A **57**, 4956 (1998).

[36] J. Usukura, Y. Suzuki and K. Varga, Phys. Rev. B **59**, 5652 (1999).

[37] C. Riva, F. M. Peeters, K. Varga, and V. A. Schweigert, Phys. Stat. Sol. B **234**, 50 (2002) and references therein.

[38] Y. E. Lozovik and O. L. Berman, Zh. Eksp. Teor. Fiz. **111**, 1879 (1997) [Sov. Phys. JETP **84**, 1027 (1997)].

[39] S. Ben-Tabou de-Leon and B. Laikhtman, Europhys. Lett. **59**, 728 (2002).

[40] Ch. Schindler and R. Zimmermann, Phys. Rev. B **78**, 045313 (2008); R. Zimmermann and Ch. Schindler, Solid State Commun. **144**, 395 (2007).

[41] L. D. Landau and E. M. Lifshitz, *Quantum Mechanics: Nonrelativistic Theory* (Pergamon, New York, 1965).

[42] Y. Suzuki and K. Varga, *Stochastic variational approach to quantum-mechanical few-body problems*, Lecture Notes in Physics **M54** (Springer, Berlin, 1998), pp. 1-310.

[43] I. S. Gradshteyn and I. M. Ryzhik *Table of Integrals, Series, and Products*, 6th ed., edited by A. Jeffrey and D. Zwillinger (Academic, San Diego, 2000).

[44] D. Bollé and F. Gesztesy, Phys. Rev. Lett. **52**, 1469 (1984); Phys. Rev. A **30**, 1279 (1984).

[45] M. Born and J. R. Oppenheimer, Ann. Phys. (Leipzig) **84**, 457 (1927).

[46] M. Born, Festschrift Göttinger Akademie der Wissenschaften, I: Math.-Phys. Klasse 1 (1951); M. Born and H. Huang, *Dynamical Theory of Crystal Lattices* (Oxford University Press, New York, 1998).

[47] To this end one can iteratively diagonalize the four-body biexciton Hamiltonian H_{XX} by a sequence of canonical transformations. [60, 61] Equivalently, in the Lagrangian formalism, one would integrate out two out of four fermion degrees of freedom. This generates corrections to the potential and kinetic terms of Eq. (3.35).

[48] J. Adamowski, S. Bednarek, and M. Suffczynski, Solid State Comm. **9**, 2037 (1971).

[49] S. Okumura and T. Ogawa, Phys. Rev. B **65**, 035105 (2001).

[50] R. T. Pack and J. O. Hirschfelder, J. Chem. Phys. **52**, 521 (1970).

[51] M. N. Saha, Proc. Roy. Soc. London, Ser. A **99**, 135 (1921).

[52] L. V. Butov, A. L. Ivanov, A. Imamoglu, P. B. Littlewood, A. A. Shashkin, V. T. Dolgopolov, K. L. Campman, and A. C. Gossard, Phys. Rev. Lett. **86**, 5608 (2001).

[53] L. V. Butov, A. V. Mintsev, Yu. E. Lozovik, K. L. Campman, and A. C. Gossard, Phys. Rev. B **62**, 1548 (2000).

[54] L. Schultheis, K. Köhler, and C. W. Tu, Phys. Rev. B **36**, 6609 (1987).

[55] A. T. Hammack, N. A. Gippius, Sen Yang, G. O. Andreev, L. V. Butov, M. Hanson, and A. C. Gossard, J. Appl. Phys. **99**, 066104 (2006).

[56] A. Filinov, M. Bonitz, P. Ludwig, and Yu. E. Lozovik, Phys. Stat. Sol. (C) **3**, 2457 (2006).

[57] Ph. Briet, J. M. Combes, and P. Duclos, Commun. Math. Phys. **126**, 133 (1989).

[58] M. V. Berry and A. M. Ozorio de Almeida, J. Phys. A **6**, 1451 (1973).

[59] S. C. Miller and R. H. Good, Phys. Rev. **91**, 174 (1953).

[60] P. R. Bunker and R. E. Moss, Mol. Phys. **33**, 417 (1977).

[61] S. Weigert and R. G. Littlejohn, Phys. Rev. A **47**, 3506 (1993).

[62] A. A. High and L. V. Butov, Unpublished (2009).

[63] R. M. Lee, N. D. Drummond, and R. J. Needs, Phys. Rev. B **79**, 152308 (2009).

[64] S. M. Sze, *Physics of Semiconductor Devices* (Wiley, New York, 1981).

[65] A. R. Brown, C. P. Jaret, D. M. de Leeuw, and M. Matters, Synth. Met. **88**, 37 (1997).

[66] M. C. J. M. Vissenberg and M. Matters, Phys. Rev. B **57**, 12964 (1998).

[67] W. F. Pasveer *et al.*, Phys. Rev. Lett. **94**, 206601 (2005).

[68] D. Natali, L. Fumagalli, and M. Sampietro, J. Appl. Phys. **101**, 014501 (2007).

[69] K. Seshadri and C. D. Frisbie, Appl. Phys. Lett. **78**, 993 (2001).

[70] L. Bürgi, H. Sirringhaus, and R. H. Friend, J. Appl. Phys. **80**, 2913 (2002); L. Bürgi *et al.*, Synth. Met. **146**, 297 (2004).

[71] Z. Q. Li, G. M. Wang, N. Sai, D. Moses, M. C. Martin, M. Di Ventra, A. J. Heeger, and D. N. Basov, Nano Lett. **6**, 224 (2006).

[72] O. Tal *et al.*, Phys. Rev. Lett. **95**, 256405 (2005).

[73] B. H. Hamadani and D. Natelson, J. Appl. Phys. **95**, 1227 (2004); **97**, 064508 (2005).

[74] G. Wang *et al.*, J. Appl. Phys. **95**, 316 (2004).

[75] No significant field-dependence of μ was found experimentally at such temperature [70, 74]. The nonlinearity of the contact resistance can still be significant [70]; however, it has no effect on our contactless measurements.

[76] A. S. Dhoot, G. M. Wang, D. Moses, and A. J. Heeger, Phys. Rev. Lett. **96**, 246403 (2006).

[77] By means of repeated capture and release from shallow traps, charge carriers in our experiment travel macroscopic distance (almost a mm) away from injecting electrodes and the decay of $N(x)$ is detected chiefly because we intentionally work with a large-area FET with a non-negligible leakage current.

[78] Deep in the current saturation regime (where $V(0)$ and $V(L)$ are of opposite sign) one cannot treat the problem as one-dimensional, and σ_r becomes position dependent, see, e.g., Ref. [65]. We do not consider this case here.

[79] In order to obtain this fit Bürgi *et al.* had to shift all their data by $2\,\mathrm{V}$, a significant fraction of the total $V_{SD} = 8\,\mathrm{V}$. They argued that such a shift can be viewed as a way to account for residual carriers. We think that a more consistent approach is in terms of a finite σ_r.